Non-linear Dynamo Action and Disc-Halo Interaction in Disc Galaxies

Andrew Smith

Thesis submitted for the degree of
Doctor of Philosophy

School of Mathematics and Statistics
Newcastle University
Newcastle upon Tyne
United Kingdom

September 2011

For those whom I wish could have seen the completion of this thesis.

Acknowledgements

I would like to take this opportunity to thank all those involved in the completion of this thesis. Firstly my supervisors, Dr. Andrew Fletcher, and Prof. Anvar Shukurov, the STFC, and the staff at the Mathematics and Statistics department at Newcastle University, without them none of this would have been possible.

I would also like to thank everyone who has supported me throughout my PhD, from my family, friends and colleagues, and everyone who has offered an ear whenever I've required it in the last 4 years.

Abstract

We have developed a mathematical model which reproduces a broad range of observables in several galaxies, within the same physical framework.

We present an observationally constrained model of mass outflow for galactic discs, derived from star formation rate. This is used to supplement a model of the non-linear, mean-field, $\alpha^2\Omega$ galactic dynamo in the presence of shear. Outflows affect the magnetic pitch angles unexpectedly. This resolves a long standing problem in non-linear dynamo theory, marking a fundamental improvement in the degree of agreement with observations.

The mean-field equations are reduced using a modified version of the no-z approximation, to allow for observed flaring of gaseous galactic discs, leaving us with a flared thin-disc model. We have explored two non-linearities to describe the α-effect. We use recent spatially dependent observations of various galaxy properties to evolve the dynamo equations in time. We present results of the steady state magnetic field for both nonlinearities and demonstrate that observables such as local magnetic field strength and magnetic pitch angle can be closely reproduced, using optimum, physically acceptable values of outflow velocity.

We apply the model to a number of well observed galactic systems with similar kinematic properties and discuss several sensitivities of the model whilst modifying data sets within the ranges of observational uncertainty.

Contents

1 Introduction **2**

1.1 Background . . . 2
1.2 What is a galaxy? . . . 3
1.3 Galactic magnetic fields . . . 5
1.4 What is a dynamo? . . . 7
1.5 The galactic dynamo . . . 8
1.6 The Ω-effect . . . 8
1.7 The α-effect . . . 10
1.8 Magnetic helicity . . . 12
1.9 Organisation of the thesis . . . 13

2 Derivation of the model for a galactic dynamo **15**

2.1 Derivation of the Model Equations . . . 15
2.1.1 Thin disc approximation . . . 15
2.1.2 Non-dimensionalisation . . . 19
2.2 The α-effect . . . 21
2.2.1 α-quenching . . . 21
2.2.2 Dynamical α . . . 22
2.3 Physical models for vertical and radial flows . . . 24
2.3.1 A physical model for U_z . . . 24
2.3.2 Interpretation of the vertical outflow model . . . 27
2.3.3 A physical model for U_r . . . 29

3 Verification and application of the dynamo model **30**

3.1 "Accretion and galactic dynamos": Moss *et al.* (2000) . . . 30
3.1.1 The effect of an inflow . . . 34
3.1.2 Switching on the inflow . . . 36

3.1.3 α-quenching . . . 37
3.1.4 Inflow with α-quenching . . . 37
3.2 "Galactic dynamos supported by magnetic helicity fluxes": Sur *et al.* (2007) 40
3.2.1 Modifications to the no-z approximation for galactic dynamos . . . 43
3.3 The Magnetic field of M31 . . . 45
3.3.1 "The nature of the magnetic belt in M31": Moss *et al.* (1998) . . . 45
3.3.2 New gas density profile . . . 49
3.3.3 New rotation curve . . . 50
3.3.4 The effect of an outflow on the magnetic field . . . 51

4 The Andromeda Galaxy (M31/NGC224) 54
4.1 Introduction . . . 54
4.2 Observational parameters for M31 . . . 58
4.2.1 Gaseous disc scale height . . . 58
4.2.2 Gas densities . . . 59
4.2.3 Rotation curve . . . 61
4.2.4 Star formation rate . . . 64
4.2.5 Outflow model . . . 65
4.3 Results . . . 67
4.3.1 Galactic parameters . . . 67
4.3.2 Comparison with observations . . . 67
4.3.3 Dynamos with α-quenching . . . 67
4.3.4 Dynamos with a dynamical α . . . 68
4.3.5 Time evolution of the magnetic field . . . 71
4.4 Saturation of the dynamo with constant $\alpha_{\rm k}$ . . . 76
4.5 Sensitivity to model inputs . . . 78
4.6 Summary . . . 82

5 The Triangulum Galaxy (M33/NGC598) 83
5.1 Introduction . . . 83
5.2 Observational data . . . 84
5.2.1 Gaseous disc scale height . . . 84
5.2.2 Gas densities . . . 85
5.2.3 Rotation curve . . . 86
5.2.4 Star formation rate . . . 87
5.2.5 Outflow model . . . 88

5.3 Results . . . 89
5.3.1 Galactic parameters . . . 89
5.3.2 Dynamos with α-quenching . . . 89
5.3.3 Dynamos with a dynamical α . . . 90
5.3.4 Pitch angle of the magnetic field . . . 93
5.4 Summary . . . 93

6 The Whirlpool Galaxy (M51a/NGC5194) 95
6.1 Introduction . . . 95
6.2 Galactic observations . . . 96
6.2.1 Gaseous disc scale height . . . 96
6.2.2 Gas densities . . . 97
6.2.3 Rotation curve . . . 98
6.2.4 Star formation rate . . . 99
6.2.5 Outflow and inflow models . . . 100
6.3 Results . . . 100
6.3.1 Galactic parameters . . . 100
6.3.2 Dynamos with α-quenching . . . 102
6.3.3 Dynamos with a dynamical α . . . 102
6.3.4 Pitch angle of the magnetic field . . . 105
6.4 Summary . . . 105

7 The Fireworks Galaxy (NG6946) 107
7.1 Introduction . . . 107
7.2 Galactic observations . . . 108
7.2.1 Gaseous disc scale height . . . 108
7.2.2 Gas densities . . . 109
7.2.3 Rotation curve . . . 110
7.2.4 Star formation rate . . . 111
7.2.5 Outflow model . . . 112
7.3 Results . . . 113
7.3.1 Galactic parameters . . . 113
7.3.2 Dynamos with α-quenching . . . 114
7.3.3 Dynamos with a dynamical α . . . 114
7.3.4 Pitch angle of the magnetic field . . . 117
7.4 Summary . . . 118

8 Conclusions **119**

Bibliography **122**

Chapter 1

Introduction

1.1 Background

Astrophysical dynamo theory is certainly not a new interest amongst both physicists and mathematicians, having been studied since the early part of the 20th century.

In 1919, Sir Joseph Larmor hypothesised that an astrophysical body such as the Sun could possess a self exciting magnetic field, motivated by the realisation that without any sort of regenerative and maintaining mechanism, magnetic fields naturally decay. We wish to apply such thinking to larger astrophysical systems, in particular, spiral galaxies.

Many spiral galaxies have well observed magnetic fields (e.g. Beck *et al.* (1996); Fletcher (2011)) and in recent times, with the advent of more technologically advanced observational instrumentation and data analysis methods, the understanding of the magnetic properties of these massive astrophysical structures has significantly increased. At the same time, new observations have been made that reveal the properties of the interstellar gas in nearby spiral galaxies at a comparable resolution (e.g. Walter *et al.* (2008), a study of H I in nearby galaxies, and Chemin *et al.* (2009), including observations of H I in M31).

This new wealth of observational data is an invaluable asset, and facilitates the opportunity for scientists to start to combat long standing problems, fundamental questions such as how galaxies are created, how long they have existed, and equally deep questions such as how they share dynamics with so many other very similar galaxies, and as this

work will discuss, how are they able to maintain a magnetic field which in theory should have decayed billions of years ago.

1.2 What is a galaxy?

A galaxy is a collection of stars, dark matter and dust, gas, magnetic fields and cosmic rays, where the latter (those from dark matter to cosmic rays) are collectively known as the interstellar medium or ISM. The most common types of galaxy in the universe are elliptical, dwarf and disc galaxies.

Elliptical galaxies have little gas content, and typically do not have active star forming regions. These galaxies have small-scale magnetic fields, but no discernable large-scale magnetic field. Dwarf galaxies are active regions of star formation, which give rise to galactic outflows. They are regularly weakly rotating, or do not rotate at all, however still possess global magnetic fields. Disc galaxies are active, evolving systems, with large volumes of interstellar gas, dust, magnetic fields and star formation. In this thesis we only discuss disc galaxies.

Disc galaxies generally comprise of three parts: a roughly spherical central bulge; a flared disc, which can be of the order of 0.1 to several kpc thick, which is made up of stellar material and gas; and the halo, which consists of stellar material, gas, dust and dark matter. The halo will typically be ellipsoidal in shape and can have a polar diameter in the order $15 - 20\,\mathrm{kpc}$. This surrounding halo of hot gas is supplied by outflows of supernova remnant heated gas from the disc, in a process known as the galactic fountain.

The interstellar gas typically constitutes 10–15% of the mass in a galactic disc (Ferrière, 2001). It consists of a number of relatively distinct phases, outlined in Table 1.1. Chemically, in terms of numbers of particles, about 90% of the gas in the ISM is hydrogen, and a further 9% is helium. About half the mass in the ISM is confined to small dense clouds, accounting for only $1 - 2\%$ of the interstellar volume. These clouds fall into three categories; cold, dense molecular clouds, which can be observed by proxy via the CO emission line, then diffuse, transparent atomic clouds, and clouds which contain a mix of molecular and atomic gases, which can all be observed directly by the H I 21cm line, lying between the two other types of cloud in terms of visibility.

Galaxies are gravitationally bound, dynamically evolving systems. The typical orbital period of the Sun with respect to the galactic centre is 2.5×10^8yr (Bissantz *et al.*, 2003). All galaxies rotate differentially, and this is well known from observations of gas velocity. Contrary to Kepler's laws, which would have the rotation velocity of the disc decrease

Component	Temp. (K)	Density (cm^{-3})
Molecular clouds	$10 - 20$	$10^2 - 10^6$
Cold atomic medium	$50 - 100$	$20 - 50$
Warm atomic medium	$6000 - 10000$	$0.2 - 0.5$
Warm ionised medium	8000	$0.2 - 0.5$
Hot ionised medium	10^6	0.0065

Table 1.1: ISM hydrogen phase descriptions from Ferrière (2001). Density refers to the number of molecules/atoms/ions per unit volume.

inversely in proportion to the square root of galactocentric radius, r, galaxies typically have a flattened rotational velocity profile (from this point we will refer to this as the rotation curve) in the outer regions of the disc. It is thought that this is a result of the dark matter content in galaxies.

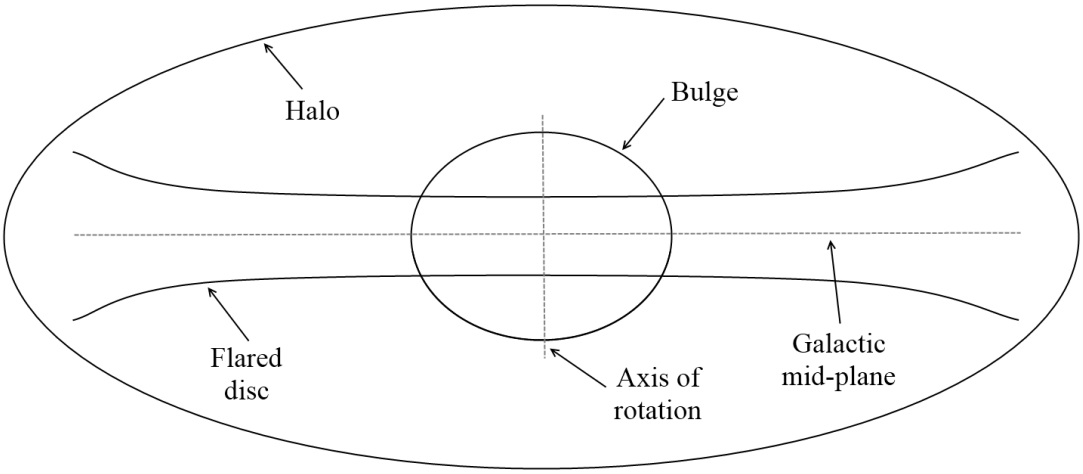

Figure 1.1: Sketch of a typical spiral galaxy and its components.

The large scale magnetic field is concentrated within the flared disc, so we wish to pay this particular attention.

1.3 Galactic magnetic fields

Galactic magnetic fields are well observed and studied (e.g. Beck *et al.* (1996)). They exist on both large ($> 1\,\mathrm{kpc}$) and small scales ($< 100\,\mathrm{pc}$) and are observable indirectly at optical and radio wavelengths, though most information is sourced from radio continuum data (Beck *et al.*, 1996).

Measuring magnetic fields

Certain aspect of magnetic fields in galaxies can be observed using a number of different methods.

Synchrotron Emission

The strengths and directions of the total and regular magnetic fields in galaxies can be ascertained from measurements of total and linearly polarised synchrotron radiation produced by the interaction of cosmic rays with the magnetic fields. The cosmic rays are relativistic electrons, with a particular energy density. It is assumed that there is a relation between this energy density and the energy density of the magnetic field (Beck *et al.*, 1996). The degree of polarisation of the synchrotron emission can be used to give an estimate of the regular magnetic field strength perpendicular to the direction of the emission, i.e. in the plane of the sky.

Faraday Rotation

When a linearly polarised radio wave passes through a plasma with a magnetic field, its plane of polarisation is rotated in proportion to the intensity of the component of the magnetic field parallel to the direction of travel of the wave. This is called Faraday rotation, and gives another method with which to measure the strength of the regular magnetic field. The ratio of rotation angle to the wavelength of the observed radio wave is called the Faraday rotation measure, RM, which is sensitive to the strength and direction of the regular magnetic field. The RM is extremely useful as its sign allows a clear definition of the two directions of the magnetic field to be obtained. This also dictates that the method is sensitive to such phenomena as field reversals (Beck *et al.*, 1996).

Optical polarisation

Light is scattered by dust grains which are aligned by magnetic fields. This light becomes partially polarised perpendicular to the magnetic field (Weilebinski, 1990). One drawback to this method of observing the magnetic field in a galaxy is that it can only provide information on the orientation of the field, not its strength.

Zeeman splitting

The most direct method of measuring magnetic fields is the Zeeman effect (Weilebinski, 1990).

An atom or molecule has a magnetic moment, and the effect arises when this magnetic moment is coupled with an external magnetic field (Heiles *et al.*, 1993). The external magnetic field removes the degeneracy in states with nonzero angular momentum. This splits transitions into a number of components in two categories; circularly polarised components and eliptically polarised components. It is the amplitudes of the circularly polarised components that are used to measure the angle between the magnetic field and the line of sight (Heiles *et al.*, 1993). The information gained from the Zeeman effect allows us to understand the magnetic fields in molecular clouds.

Measuring magnetic field structure

In spiral galaxies, magnetic fields follow spiral patterns, with typical strengths of a few μG, contained both within the spiral arms, and in the inter-arm regions. They have similar energy densities to small scale turbulence, and the gas thermal energy.

We introduce the cylindrical polar coordinate system we shall use throughout this study, where directions are azimuthal, ϕ, radial, r and vertical, z.

An important observable quantity in galactic magnetic field studies is the magnetic pitch angle, p, defined via

$$\tan(p) = \frac{B_r}{B_\phi},$$

a measure of the angle the total magnetic field vector makes with the azimuthal vector. Observed pitch angles are non-zero and the pitch angle is recognised as a very important quantity for the diagnosis of the origin of galactic magnetic fields. The only known mechanism which can produce non-zero radial and azimuthal magnetic field components is the dynamo, via the α and Ω effects discussed later in this chapter.

If there was a magnetic field of μG magnitude present around the time of the formation of the galaxy, and no mechanism to maintain this field, then the decay of the field

would be governed by the nature of the gas in the system. The magnetic diffusion time can be estimated as

$$t_d = \frac{h_0^2}{\eta_t}, \tag{1.1}$$

where h_0 is the typical scale height of the gaseous component of the disc, and $\eta_{\rm t}$ is the turbulent magnetic diffusivity of the gas. Our galactic coordinate system is cylindrical and has vertical, z, azimuthal, ϕ, and radial, r components. For a typical scale height of $h_0 = 500\,{\rm pc}$, and a turbulent magnetic diffusivity coefficient of $\eta_t = 1 \times 10^{26}\,{\rm cm^2\,s^{-1}}$ (Moss *et al.*, 2000; Shukurov *et al.*, 2006), $t_{\rm d} \approx 10^8{\rm yr}$, on the order of 1/100 the age of a typical spiral galaxy. This suggests that the magnetic field should have decayed naturally long ago, and the observed magnetic fields should not exist.

1.4 What is a dynamo?

The premise of a dynamo mechanism is relatively simple (Parker, 1955); a body of electrically conductive fluid in the presence of a magnetic field[1] is considered (in the specific case of a galaxy, this fluid is the interstellar medium.). A flow of material exists, such that the magnetic field is amplified, and this amplification sustains the flow.

In mean-field dynamo theory, we study the large scale part of the magnetic field, under the assumption that we can distinguish between large and small scale components $\boldsymbol{B} = \overline{\boldsymbol{B}} + \boldsymbol{b}$, and the evolution of the field is governed by the mean-field equation for magnetic induction

$$\frac{\partial \overline{\boldsymbol{B}}}{\partial t} = \nabla \times \left(\overline{\boldsymbol{u} \times \boldsymbol{b}}\right) + \nabla \times \left(\overline{\boldsymbol{U}} \times \overline{\boldsymbol{B}}\right) + \eta \nabla^2 \overline{\boldsymbol{B}},$$

with time, t, magnetic diffusivity, η, the velocity vector, $\boldsymbol{U} = \overline{\boldsymbol{U}} + \boldsymbol{u}$, and the magnetic field, $\overline{\boldsymbol{B}}$. The small scale components term will later be interpreted as contributing to the α-effect which will be introduced shortly. An assumption made is that η is constant with respect to position[2].

The dynamo functions by producing azimuthal magnetic fields from radial ones, then

[1] An initial condition imperative to the success of a dynamo is a "seed field" a magnetic field which is then amplified by the dynamo. In this work, we do not discuss the initial creation of these seed fields, but see Widrow (2002) for a detailed description of the various mechanisms by which seed fields can be produced.

[2] This is not necessarily the case, however, in the thin disc approximation we shall be using for this study, where the diffusion is taken at the mid-plane, it can be taken as constant (Moss *et al.*, 1998).

back again, creating a self sustaining magnetic field. The mechanisms for these conversions of the magnetic field components are known as the Ω and α effects.

1.5 The galactic dynamo

The galactic dynamo has been an active area of research for a number of decades (Ruzmaikin *et al.*, 1988; Beck *et al.*, 1996). The idea is to take a thin disc with a very weak seed magnetic field. Taking this approximation allows the dynamo to be considered in a smaller number of dimensions (typically one, occasionally two) and dictates via the weak field that motions in the disc can be considered independent from the magnetic field, known as the kinematic limit (Kulsrud & Zweibel, 2008). The magnetic field is evolved only via the magnetic induction equation, with a set of realistic galactic parameters. Both $\alpha\Omega$ and $\alpha^2\Omega$ dynamos have been considered, primarily in flat geometries.

1.6 The Ω-effect

We begin with a disc, with a net poloidal magnetic field, $\boldsymbol{B}_{\rm p} = (B_r, 0, B_z)$, where subscripts r and z denote the radial and vertical components in cylindrical polar geometry. This magnetic field has a dominant component in the radial direction compared to the vertical direction, which is not the case for a spherical system such as a star, or a planet. So, we consider this field as being radial (Fig. 1.2). We also reserve the subscript ϕ to represent the azimuthal component, $\boldsymbol{B}_{\rm az} = (0, B_\phi, 0)$

The Ω-effect describes how the differential rotation of the disc transforms this radial field into an azimuthal one.

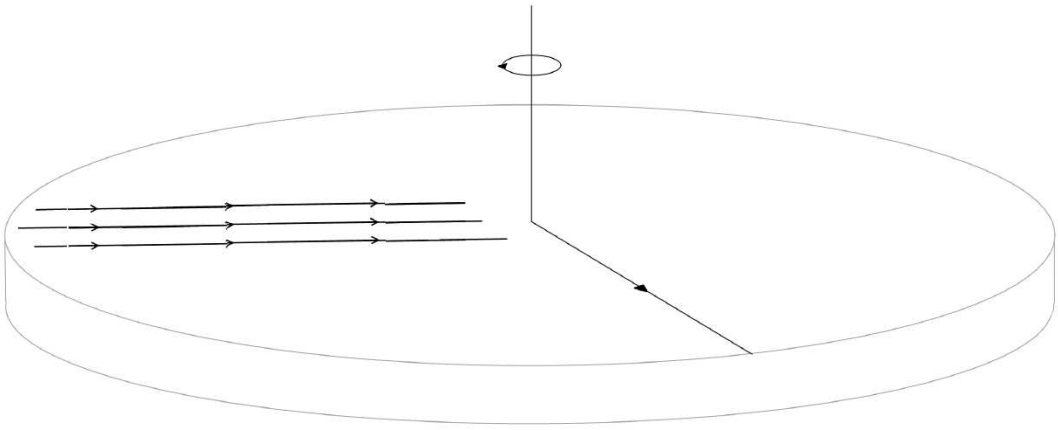

Figure 1.2: Sketch of a galactic disc, with an initial net radial magnetic field, denoted by the parallel lines. The vertical line denotes the axis of rotation.

Upon a differential rotation of the disc, the magnetic field lines begin to "wind up" as in Fig. 1.3.

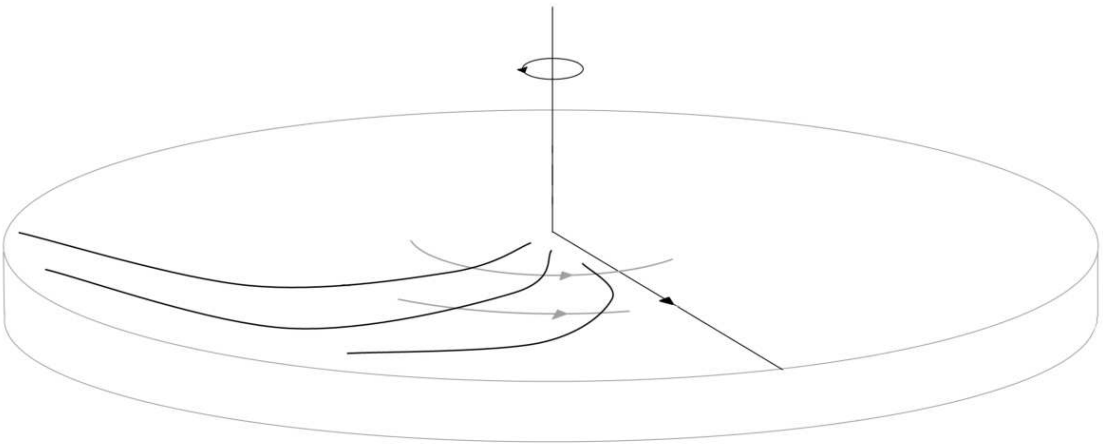

Figure 1.3: Differential rotation of the galactic disc, shown by the azimuthal arrowed lines, winding up the magnetic field lines and stretching them, thus converting B_r into B_ϕ.

After a period of time, this winding up of the field reaches the extreme where the result is an essentially azimuthal magnetic field (Fig. 1.4). For a dynamo to work,

a mechanism is required to convert this azimuthal field back into a radial field. This mechanism is the α-effect.

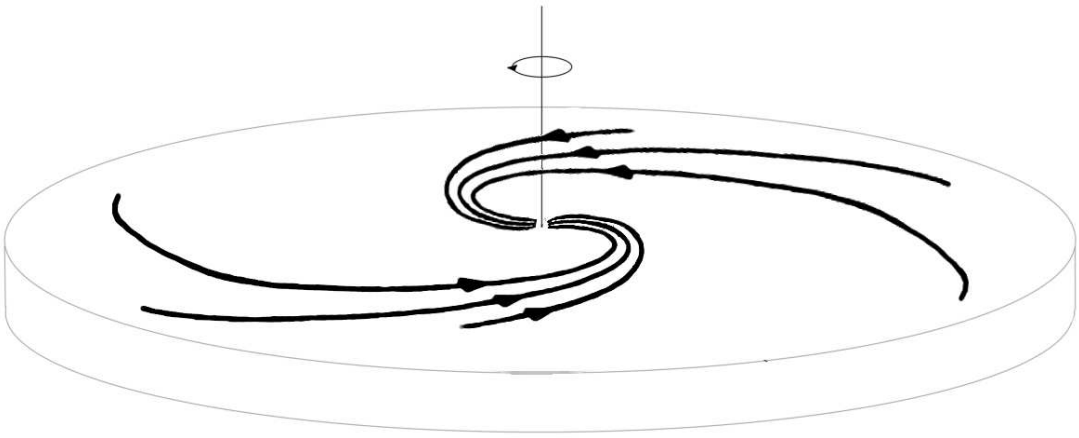

Figure 1.4: Net azimuthal magnetic field resulting from the winding up of the radial magnetic field by the differential rotation of the gaseous disc into a tightly wound spiral.

1.7 The α-effect

The α-effect is one of the most widely debated topics in astrophysical dynamo theory. Such a mechanism for the return of an azimuthal magnetic field to a radial field has not been directly observed within a galactic context, however laboratory dynamos have demonstrated the α-effect (Muller & Stieglitz, 2002). There is no large scale effect such as differential rotation to describe such mechanisms, so we must look to small scale motions to qualitatively discuss what is happening.

We progress from our recently acquired azimuthal field, and make the assumption that buoyant small-scale turbulent motions, or bubbles and superbubbles in the ISM created by supernova remnants (Ferrière, 1993), are sufficient to create loops in the magnetic field lines (Fig. 1.5).

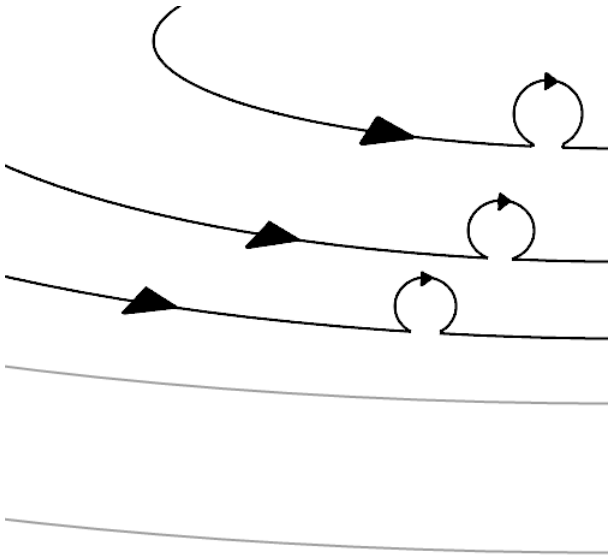

Figure 1.5: Small scale turbulent motions create loops in the magnetic field lines.

The Coriolis force twists these rising loops (Fig. 1.6), producing a radial field component. This radial field is unlike the original state, in that there are parts of the field directed radially inwards, and some directed radially outwards. The radial field of one of the signs is lost to the halo by means of a vertical outflow. The Ω-effect can convert the remaining disc radial field into an azimuthal one, and so a cycle of field amplification is created: a dynamo.

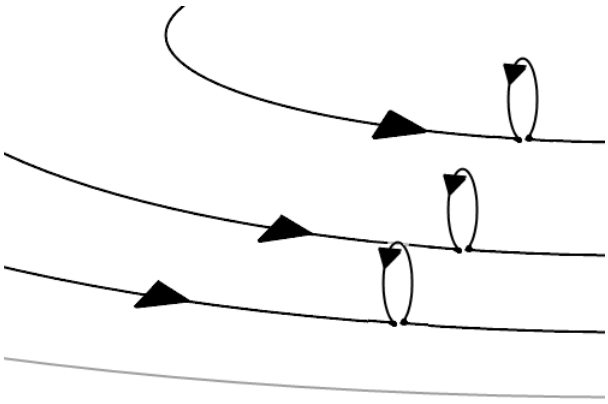

Figure 1.6: As a result of the Coriolis force, the loops are twisted. The summation of the field in these loops results in a multi-directional radial magnetic field. One of the radial components is lost to the halo by means of a galactic outflow.

1.8 Magnetic helicity

Magnetic helicity is a description of how twisted a magnetic field is. If we imagine a simple unaltered loop of magnetic field, we would say it has no helicity, however, if we take that loop and twist it so it would appear as a figure of 8, we would then say that the magnetic field has a certain helicity.

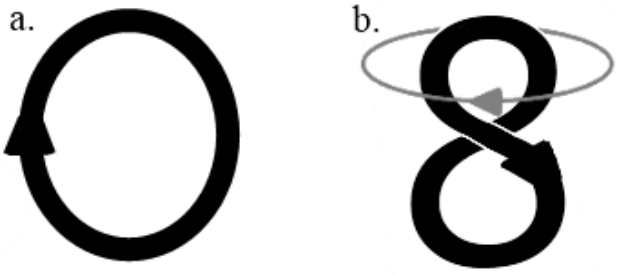

Figure 1.7: (a). Un-altered loop of magnetic field. (b). Same loop of magnetic field, fixed in position at the bottom, and twisted at the top, to create helicity.

Density of magnetic helicity can be described mathematically as $\chi = \boldsymbol{A} \cdot \boldsymbol{B}$ (Subramanian & Brandenburg, 2006), where $\boldsymbol{A}$ is a vector potential of the magnetic field, $\boldsymbol{B} = \nabla \times \boldsymbol{A}$.

The conservation of magnetic helicity in a system with closed boundaries could pose a problem for mean-field theory. The large-scale magnetic field generated by the dynamo has a non-zero net magnetic helicity. This is accompanied by an increase in opposite signed magnetic helicity at smaller scales. This leads to early suppression of the α-effect, and hence switches off the regular magnetic field growth before the equipartition magnetic field strength is reached (Brandenburg & Subramanian, 2005).

Open boundaries could allow for the possible advection of the small- scale magnetic helicity out of the system and so alleviate the problem (Blackman & Field, 2000). This solution is attractive in the case of disc galaxies, where the strongest regular fields are found, and presumably generated, in the disc which is embedded in an extended hot, ionised halo. The origin of the halo gas is the heating of disc gas by supernovae, making it buoyant and so producing a flow across the disc- halo interface. Recent developments in galactic dynamo theory have led to a physically enriched description of the α-effect in galaxies, by allowing for the transport of small-scale magnetic helicity out of the active dynamo layer in the disc into the galactic halo (Shukurov *et al.*, 2006; Sur *et al.*, 2007). This mechanism can alleviate the drastic quenching of the α-effect, and thus the saturation of the large-scale magnetic field strength at levels far below those observed due to the build up of small-scale magnetic helicity.

Shukurov *et al.* (2006) and Sur *et al.* (2007) derived an equation for the evolution of the α-effect that allows for the advection of small-scale magnetic helicity and showed that for plausible parameters describing outflows from the disc, either as a galactic fountain or galactic wind, the coupled non-linear system of equations describing the evolution of the magnetic field $\boldsymbol{B}$ and α can lead to field strengths of about 1/10 of the equipartition value (Sur *et al.* (2007) showed this 1/10 magnitude strength, and later, we demonstrate magnetic field strengths of the order 1/5 equipartition).

We will extend the generic model of Shukurov *et al.* (2006) and Sur *et al.* (2007) by coupling the equation describing the dynamical evolution of the α-effect with a model for galactic outflows driven by supernovae, that depends upon the star-formation rate: an observable quantity. This model will then be applied to specific nearby galaxies.

1.9 Organisation of the thesis

The aim of this thesis is to:

- Develop a new model for galactic dynamos, incorporating an outflow from the disc to the halo, motivated by the advection of small-scale magnetic helicity as a

mechanism to alleviate catastrophic quenching of the dynamo;

- Investigate the effect of the outflow on the observable radial profiles of magnetic field strength and magnetic pitch angle, providing new results so that direct comparisons can be made between the new magnetic field simulations and pitch angle simulations, and the observed values of these quantities already in existence;

- Apply the new dynamo models to several nearby galaxies, using observationally constrained inputs such as rotation curve, gas density profiles and disc scale heights, and compare the outputs to observed parameters of the regular magnetic field in these galaxies.

In Chapter 2, we introduce the governing equations of the mean-field dynamo and outflow models. In Chapter 3, we review some generic dynamo models via the reproduction of previous works but with some additions to explore some of the possibilities in terms of modification of parameters, boundary conditions etc. In Chapter 4, we apply our model, with the inclusion of recent observational data, to the galaxy M31, and explore the effects of the outflow on the magnetic field strength and magnetic pitch angle. In Chapters 5 to 7, we apply the model to the galaxies; M33, M51 and NGC6946, again exploring the effects of galactic outflows on the magnetic field strength and magnetic pitch angle. The main conclusions are summarised in Chapter 8.

Magnetic fields in galaxies have been studied for decades, and still are not thoroughly understood. The exact nature of the magnetic fields we observe remains, even though much advancement has been made in the area, somewhat of a conundrum. The aim of this thesis is to help in the continued advancement in the theory surrounding this topic, to bring our understanding of such fascinating astronomical phenomena slightly closer to completion.

———

Chapter 2

Derivation of the model for a galactic dynamo

2.1 Derivation of the Model Equations

2.1.1 Thin disc approximation

We will model the thin galactic disc using the no-z approximation (Subramanian & Mestel, 1993; Moss, 1995). The thin disc approximation assumes that $\partial/\partial z \gg \partial/\partial r \gg 1/r\,(\partial/\partial\phi)$. This method has been used in models of galactic dynamos in the past (Moss *et al.*, 2000; Phillips, 2001; Sur *et al.*, 2007). We will also consider only axisymmetric galactic discs, i.e. taking $1/r\,(\partial/\partial\phi) = 0$, thus ignoring secondary effects of spiral arms and other intermediate-scale structures. We consider the disc component of a galaxy, and approximate thusly. We assume cylindrical polar geometry of a disc of half-thickness $h_0 = 0.5\,\mathrm{kpc}$, and a radius (dependent on the galaxy) of $R_0 = 20\,\mathrm{kpc}$, resulting in a disc aspect ratio of $\lambda = h_0/R_0 \simeq 1/40$. We ultimately take $B_z = 0$, however only after making use of those derivates of B_z that can be sensibly evaluated. We aim to solve the mean field magnetic induction equation for dynamo action

$$\frac{\partial \overline{\boldsymbol{B}}}{\partial t} = \nabla \times \left(\overline{\boldsymbol{U}} \times \overline{\boldsymbol{B}} + \boldsymbol{\mathcal{E}} - \eta \overline{\boldsymbol{J}}\right), \tag{2.1}$$

where $\overline{\boldsymbol{U}}$, $\overline{\boldsymbol{B}}$ and $\overline{\boldsymbol{J}}$=$\nabla \times \overline{\boldsymbol{B}}$ are the mean velocity field, magnetic field, and current density respectively. Summed with their respective fluctuating quantities, the total of these quantities is $\boldsymbol{B}$=$\overline{\boldsymbol{B}} + \boldsymbol{b}$, etc. $\boldsymbol{\mathcal{E}} = \overline{\boldsymbol{u} \times \boldsymbol{b}}$ is the mean electromotive force arising from small-scale velocity fluctuations, and can be written as (Krause & Rädler, 1980;

Ruzmaikin *et al.*, 1988)

$$\boldsymbol{\mathcal{E}} = \alpha\overline{\boldsymbol{B}} - \eta_t\overline{\boldsymbol{J}},$$

where α represents the α-effect, and η_t is the turbulent magnetic diffusivity. The ohmic magnetic diffusivity, η (an inherent property of the gas in the system), is considerably smaller than η_t, so Eq. (2.1) can be approximated as

$$\frac{\partial\overline{\boldsymbol{B}}}{\partial t} = \nabla\times\left(\overline{\boldsymbol{U}}\times\overline{\boldsymbol{B}} + \alpha\overline{\boldsymbol{B}} - \eta_\mathrm{t}\overline{\boldsymbol{J}}\right). \tag{2.2}$$

The velocity vector can be written in terms of its three components, $\overline{\boldsymbol{U}} = (U_r, U_\phi, U_z)$. From here we only deal with mean quantities and drop the $\overline{\boldsymbol{B}}, \overline{\boldsymbol{U}}$ notation. A valuable expansion is that of the current density

$$\nabla\times(\nabla\times\boldsymbol{B}) = \nabla(\nabla\cdot\boldsymbol{B}) - \nabla^2\boldsymbol{B}.$$

We lose the first term as a consequence Maxwell's equation, $\nabla\cdot\boldsymbol{B} = 0$, i.e. that magnetic field lines are solenoidal. This reduces Eq. (2.2) to

$$\frac{\partial\boldsymbol{B}}{\partial t} = \nabla\times(\boldsymbol{U}\times\boldsymbol{B} + \alpha\boldsymbol{B}) + \eta_\mathrm{t}\nabla^2\boldsymbol{B}, \tag{2.3}$$

Where η_t is assumed to be constant with respect to position, similarly to our assumption of the constant nature of η. We can use the identity

$$\frac{1}{r}\frac{\partial}{\partial r}\left(r\frac{\partial B_i}{\partial r}\right) = \frac{\partial}{\partial r}\left(\frac{1}{r}\frac{\partial}{\partial r}(rB_i)\right) + \frac{B_i}{r^2},$$

where i can be substituted with any of the three components in the cylindrical frame of reference. We expand the Laplacian

$$\nabla^2\boldsymbol{B} = \begin{bmatrix} \frac{\partial}{\partial r}\left(\frac{1}{r}\frac{\partial}{\partial r}(rB_r)\right) + \frac{1}{r^2}\frac{\partial^2 B_r}{\partial\phi^2} + \frac{\partial^2 B_r}{\partial z^2} - \frac{2}{r^2}\frac{\partial B_\phi}{\partial\phi} \\ \frac{\partial}{\partial r}\left(\frac{1}{r}\frac{\partial}{\partial r}(rB_\phi)\right) + \frac{1}{r^2}\frac{\partial^2 B_\phi}{\partial\phi^2} + \frac{\partial^2 B_\phi}{\partial z^2} + \frac{2}{r^2}\frac{\partial B_r}{\partial\phi} \\ \frac{\partial}{\partial r}\left(\frac{1}{r}\frac{\partial}{\partial r}(rB_z)\right) + \frac{1}{r^2}\frac{\partial^2 B_z}{\partial\phi^2} + \frac{\partial^2 B_z}{\partial z^2} + \frac{B_z}{r^2} \end{bmatrix},$$

and from this, we can write Eq. (2.2) in full as

$$\frac{\partial \boldsymbol{B}}{\partial t} = \begin{bmatrix} \frac{1}{r}\frac{\partial}{\partial \phi}\left(U_r B_\phi - U_\phi B_r + \alpha B_z\right) - \frac{\partial}{\partial z}\left(U_z B_r - U_r B_z + \alpha B_\phi\right) \\ \quad +\eta_\mathrm{t}\left[\frac{\partial}{\partial r}\left(\frac{1}{r}\frac{\partial}{\partial r}\left(rB_r\right)\right) + \frac{1}{r^2}\frac{\partial^2 B_r}{\partial \phi^2} + \frac{\partial^2 B_r}{\partial z^2} - \frac{2}{r^2}\frac{\partial B_\phi}{\partial \phi}\right] \\ \\ \frac{\partial}{\partial z}\left(U_\phi B_z - U_z B_\phi + \alpha B_r\right) - \frac{\partial}{\partial r}\left(U_r B_\phi - U_\phi B_r + \alpha B_z\right) \\ \quad +\eta_\mathrm{t}\left[\frac{\partial}{\partial r}\left(\frac{1}{r}\frac{\partial}{\partial r}\left(rB_\phi\right)\right) + \frac{1}{r^2}\frac{\partial^2 B_\phi}{\partial \phi^2} + \frac{\partial^2 B_\phi}{\partial z^2} + \frac{2}{r^2}\frac{\partial B_r}{\partial \phi}\right] \\ \\ \frac{1}{r}\frac{\partial}{\partial r}\left(r\left[U_z B_r - U_r B_z + \alpha B_\phi\right]\right) - \frac{1}{r}\frac{\partial}{\partial \phi}\left(U_\phi B_z - U_z B_\phi + \alpha B_r\right) \\ \quad +\eta_\mathrm{t}\left[\frac{\partial}{\partial r}\left(\frac{1}{r}\frac{\partial}{\partial r}\left(rB_z\right)\right) + \frac{1}{r^2}\frac{\partial^2 B_z}{\partial \phi^2} + \frac{\partial^2 B_z}{\partial z^2} + \frac{B_z}{r^2}\right] \end{bmatrix}.$$

We ignore the vertical magnetic field component as $B_z \ll B_r, B_\phi$, however retain terms including B_z in the radial and azimuthal magnetic field component equations, in accordance with the previously mentioned derivates of B_z which may not be of negligible magnitude. We are left with the radial and azimuthal components of the mean-field equation

$$\begin{aligned} \frac{\partial B_r}{\partial t} = \quad & \frac{1}{r}\frac{\partial}{\partial \phi}\left(U_r B_\phi - U_\phi B_r + \alpha B_z\right) - \frac{\partial}{\partial z}\left(U_z B_r - U_r B_z + \alpha B_\phi\right) \\ & +\eta_t\left[\frac{\partial}{\partial r}\left(\frac{1}{r}\frac{\partial}{\partial r}\left(rB_r\right)\right) + \frac{1}{r^2}\frac{\partial^2 B_r}{\partial \phi^2} + \frac{\partial^2 B_r}{\partial z^2} - \frac{2}{r^2}\frac{\partial B_\phi}{\partial \phi}\right], \end{aligned} \tag{2.4}$$

$$\begin{aligned} \frac{\partial B_\phi}{\partial t} = \quad & \frac{\partial}{\partial z}\left(U_\phi B_z - U_z B_\phi + \alpha B_r\right) - \frac{\partial}{\partial r}\left(U_r B_\phi - U_\phi B_r + \alpha B_z\right) \\ & +\eta_t\left[\frac{\partial}{\partial r}\left(\frac{1}{r}\frac{\partial}{\partial r}\left(rB_\phi\right)\right) + \frac{1}{r^2}\frac{\partial^2 B_\phi}{\partial \phi^2} + \frac{\partial^2 B_\phi}{\partial z^2} + \frac{2}{r^2}\frac{\partial B_r}{\partial \phi}\right]. \end{aligned} \tag{2.5}$$

In a reduction to the no-z, axisymmetric set of equations, we need to proceed carefully. Firstly, we look at the expression which describes the solenoidal condition for magnetic field lines, $\nabla \cdot \boldsymbol{B} = 0$, which has to be maintained,

$$\nabla \cdot \boldsymbol{B} = \frac{1}{r}\frac{\partial}{\partial r}\left(rB_r\right) + \frac{1}{r}\frac{\partial B_\phi}{\partial \phi} + \frac{\partial B_z}{\partial z} = 0. \tag{2.6}$$

Taking only the axisymmetric solutions, i.e. $\partial/\partial\phi = 0$, we deduce that

$$\frac{\partial B_z}{\partial z} = -\frac{1}{r}\frac{\partial}{\partial r}\left(rB_r\right).$$

This affects the radial component of Eq. (2.4), where, without careful attention, we would have disregarded the term involving $\partial B_z/\partial z$ as being of negligible magnitude when removing the vertical field component. With this taken into consideration, and upon removal of the non- axisymmetric components, Eqs. (2.4) and (2.5) become

$$\begin{aligned}\frac{\partial B_r}{\partial t} = \quad & -\frac{U_r}{r}\frac{\partial}{\partial r}\left(rB_r\right) - \frac{\partial}{\partial z}\left(U_z B_r + \alpha B_\phi\right) \\ & +\eta_t\left(\frac{\partial}{\partial r}\left[\frac{1}{r}\frac{\partial}{\partial r}\left(rB_r\right)\right] + \frac{\partial^2 B_r}{\partial z^2}\right),\end{aligned} \tag{2.7}$$

$$\begin{aligned}\frac{\partial B_\phi}{\partial t} = \quad & -\frac{\partial}{\partial r}\left(U_r B_\phi - U_\phi B_r\right) - \frac{\partial}{\partial z}\left(U_z B_\phi - U_\phi B_z - \alpha B_r\right) \\ & +\eta_t\left(\frac{\partial}{\partial r}\left[\frac{1}{r}\frac{\partial}{\partial r}\left(rB_\phi\right)\right] + \frac{\partial^2 B_\phi}{\partial z^2}\right).\end{aligned} \tag{2.8}$$

In our models we consider the azimuthal velocity due to differential rotation only, so $U_\phi = r\Omega\left(r\right)$, with $\Omega\left(r\right)$, the rotation rate measured in $\mathrm{km\,s^{-1}\ kpc^{-1}}$. This modification leads to a change in the expression for the azimuthal field component, as a result of Eq. (2.6)

$$\frac{\partial}{\partial z}\left(U_\phi B_z\right) = -\Omega\frac{\partial}{\partial r}\left(rB_r\right) = -\Omega B_r - r\Omega\frac{\partial B_r}{\partial r}, \tag{2.9}$$

$$-\frac{\partial}{\partial r}\left(-U_\phi B_r\right) = \frac{\partial}{\partial r}\left(r\Omega B_r\right) = \Omega B_r + rB_r\frac{\partial\Omega}{\partial r} + r\Omega\frac{\partial B_r}{\partial r}, \tag{2.10}$$

$$\begin{aligned}\frac{\partial}{\partial z}\left(U_\phi B_z\right) + \frac{\partial}{\partial r}\left(U_\phi B_r\right) &= -\Omega B_r - r\Omega\frac{\partial B_r}{\partial r} + \Omega B_r \\ &\quad + rB_r\frac{\partial\Omega}{\partial r} + r\Omega\frac{\partial B_r}{\partial r} \\ &= rB_r\frac{\partial\Omega}{\partial r},\end{aligned} \tag{2.11}$$

Now the full, dimensional, equations describing the evolution of B_r and B_ϕ are

$$\begin{aligned}\frac{\partial B_r}{\partial t} = \quad & -\frac{U_r}{r}\frac{\partial}{\partial r}\left(rB_r\right) - \frac{\partial}{\partial z}\left(U_z B_r + \alpha B_\phi\right) \\ & +\eta_t\left(\frac{\partial}{\partial r}\left[\frac{1}{r}\frac{\partial}{\partial r}\left(rB_r\right)\right] + \frac{\partial^2 B_r}{\partial z^2}\right),\end{aligned} \tag{2.12}$$

$$\frac{\partial B_\phi}{\partial t} = -\frac{\partial}{\partial r}\left(U_r B_\phi\right) - \frac{\partial}{\partial z}\left(U_z B_\phi - \alpha B_r\right) + r B_r \frac{\partial \Omega}{\partial r} + \eta_t \left(\frac{\partial}{\partial r}\left[\frac{1}{r}\frac{\partial}{\partial r}\left(r B_\phi\right)\right] + \frac{\partial^2 B_\phi}{\partial z^2}\right). \tag{2.13}$$

Now we write the equations in the no-z approximation. The use of a vertical wavenumber, $k \approx 1/h$ and considering solutions of the form e^{ikz} leads us to replace our first and second vertical derivatives with $1/h\left(r\right)$ and $-1/h^2\left(r\right)$ respectively. We can rewrite Eqs. (2.12) and (2.13) leaving us with the dimensional form of the mean-field dynamo equation in the axisymmetric, no-z approximation

$$\frac{\partial B_r}{\partial t} = -\frac{U_r}{r}\frac{\partial}{\partial r}\left(r B_r\right) - \frac{1}{h} U_z B_r - \frac{1}{h}\alpha B_\phi + \eta_t \left(\frac{\partial}{\partial r}\left[\frac{1}{r}\frac{\partial}{\partial r}\left(r B_r\right)\right] - \frac{1}{h^2} B_r\right), \tag{2.14}$$

$$\frac{\partial B_\phi}{\partial t} = -\frac{\partial}{\partial r}\left(U_r B_\phi\right) - \frac{1}{h} U_z B_\phi + \frac{1}{h}\alpha B_r + r B_r \frac{\partial \Omega}{\partial r} + \eta_t \left(\frac{\partial}{\partial r}\left[\frac{1}{r}\frac{\partial}{\partial r}\left(r B_\phi\right)\right] - \frac{1}{h^2} B_\phi\right). \tag{2.15}$$

These two expressions form the basis of this work. Note that we have retained the terms involving the radial velocity component. We have done this so that we can investigate the sensitivity of the model to radial flows later on.

2.1.2 Non-dimensionalisation

It is now convenient, for computational and interpretational reasons, to write the equations in dimensionless form. This means writing the various quantities in the expressions in terms of a dimensional component (taken as a constant, here denoted with the subscript "$_0$") and a dimensionless function of radius, of the order 1. In this particular case where we are considering a 1-dimensional system, this dimensionless component is a locally varying array, for example, with a flared disc of scale height $h\left(r\right)$, typically with a value of $h_0 = 500\,\mathrm{pc}$, we can redefine $h\left(r\right) = h_0 h^*\left(r\right)$, which leaves us with a dimensionless array, $h^*\left(r\right)$ of the order unity. Our other scalings include $\alpha\left(r\right) = \alpha_0 \alpha^*\left(r\right)$, $\Omega\left(r\right) = \Omega_0 \Omega^*\left(r\right)$, $U_i\left(r\right) = U_{i0} U_i^*\left(r\right)$ and $B\left(r\right) = B_0 B^*\left(r\right)$. From this point onwards however, we shall drop the '*' notation for dimensionless quantities, and shall leave them as, for example $h\left(r\right)$.

When applied with the time scaling $t_0 = h_0^2/\eta_\mathrm{t}$ to all the quantities in Eqs. (2.14)

and (2.15), we obtain

$$\frac{\partial B_r}{\partial t} = -\frac{U_{r0}h_0}{\eta_t}\frac{h_0}{R_0}\frac{U_r}{r}\frac{\partial}{\partial r}(rB_r) - \frac{U_{z0}h_0}{\eta_t}\frac{U_z}{h}B_r - \frac{\alpha_0 h_0}{\eta_t}\frac{\alpha}{h}B_\phi + \frac{h_0^2}{R_0^2}\frac{\partial}{\partial r}\left(\frac{1}{r}\frac{\partial}{\partial r}(rB_r)\right) - \frac{B_r}{h^2}, \tag{2.16}$$

$$\frac{\partial B_\phi}{\partial t} = -\frac{U_{r0}h_0}{\eta_t}\frac{h_0}{R_0}\frac{\partial}{\partial r}(U_r B_\phi) - \frac{U_{z0}h_0}{\eta_t}\frac{U_z}{h}B_\phi + \frac{\alpha_0 h_0}{\eta_t}\frac{\alpha}{h}B_r + \frac{\Omega_0 h_0^2}{\eta_t}rB_r\frac{\partial\Omega}{\partial r} + \frac{h_0^2}{R_0^2}\frac{\partial}{\partial r}\left(\frac{1}{r}\frac{\partial}{\partial r}(rB_\phi)\right) - \frac{B_\phi}{h^2}. \tag{2.17}$$

Note we have removed B_0 from these expressions as it cancels from each term. This separation into dimensional and dimensionless variables introduces a number of dimensionless combinations of parameters

$$R_{U_r} = \frac{U_{r0}h_0}{\eta_t}, \qquad R_{U_z} = \frac{U_{z0}h_0}{\eta_t}, \qquad R_\alpha = \frac{\alpha_0 h_0}{\eta_t}, \qquad R_\omega = \frac{\Omega_0 h_0^2}{\eta_t}, \qquad \lambda = \frac{h_0}{R_0}, \tag{2.18}$$

which govern the flow velocity[1], the α- effect, and the Ω-effect respectively. We also define the disc aspect ratio, λ. We analogously define local, radially varying dimensionless numbers,

$$\mathcal{R}_{U_i}(r) = R_{U_i}U_i(r)h(r), \quad \mathcal{R}_\alpha(r) = R_\alpha\alpha(r)h(r), \quad \mathcal{R}_\omega(r) = R_\omega\Omega(r)h^2(r),$$

with the exception that the disc aspect ratio, like the time scaling, is a constant value, and not spatially dependent[2]. The local dynamo number, $D(r)$, is given by

$$D(r) = \mathcal{R}_\alpha\mathcal{R}_\omega = R_\alpha R_\omega\alpha(r)G(r)h^3(r), \tag{2.19}$$

where $G(r) = rd\Omega/dr$ is the local shear. We are left with the non-dimensional versions

[1] From this point onwards, we shall use two separate versions of this constant, R_{U_r} and R_{U_z} which will be used in the terms involving radial and vertical flows respectively. We do this to allow us to separately investigate effects of the individual velocities.

[2] The constant nature of the disc aspect ratio is required for the derivation of the equations, and the time scaling we have used. As a result there is no inclusion of any disc flaring in the disc aspect ratio.

of our basic equations,

$$\frac{\partial B_r}{\partial t} = -R_{U_r}\lambda\frac{U_r}{r}\frac{\partial}{\partial r}(rB_r) - R_{U_z}\frac{U_z}{h}B_r - R_\alpha\frac{\alpha}{h}B_\phi + \lambda^2\frac{\partial}{\partial r}\left(\frac{1}{r}\frac{\partial}{\partial r}(rB_r)\right) - \frac{B_r}{h^2}, \tag{2.20}$$

$$\frac{\partial B_\phi}{\partial t} = -R_{U_r}\lambda\frac{\partial}{\partial r}(U_rB_\phi) - R_{U_r}\frac{U_z}{h}B_\phi + R_\alpha\frac{\alpha}{h}B_r + R_\omega GB_r + \lambda^2\frac{\partial}{\partial r}\left(\frac{1}{r}\frac{\partial}{\partial r}(rB_\phi)\right) - \frac{B_\phi}{h^2}, \tag{2.21}$$

where $G = r\partial\Omega/\partial r$ is the shear rate.

2.2 The α-effect

We now introduce the two versions of the non-linear α-effect which we will be using.

2.2.1 α-quenching

The numerical quenching model is a long established method for preventing permanent exponential growth of magnetic fields in mean- field dynamos (Moss *et al.*, 1998; Panesar & Nelson, 1992). It has a simple expression

$$\alpha = \frac{\alpha_0}{1 + B^2/B_{\rm eq}^2}, \tag{2.22}$$

where α_0 is a typical velocity of the order 1 km s^{-1}, B is the magnetic field strength, and $B_{\rm eq} = \sqrt{4\pi\rho u^2}$ is the equipartition magnetic field strength, a function of the density, ρ, and turbulent velocity, u, of gas in the disc, defined via the magnetic energy density $B^2/8\pi = (\rho u^2)/2$.

This quantity becomes important when $B^2/B_{\rm eq}^2 \approx {\rm O}\,(1)$, i.e. when the field becomes strong. When B grows to a sufficient magnitude, the value of α is quenched, and the growth of the field diminishes to zero. This is called the saturated state, and shall be referred to for both the numerically quenched, and dynamically quenched models of the alpha effect.

In a modification to the above model, we follow the approach taken by Moss *et al.* (1998), where the rotation of the disc and flaring are incorporated into the model to

make it physically more realistic (but still highly simplified)

$$\alpha\left(r\right)=\frac{l^{2}\Omega\left(r\right)}{h\left(r\right)}\frac{1}{1+B^{2}/B_{\mathrm{eq}}^{2}}, \tag{2.23}$$

where l is a typical length scale. This approach is used purely as a numerical form of quenching, and apart from the addition of the rotation and flaring, has little physical background.

2.2.2 Dynamical α

The second model we evaluate describes the dynamical evolution of α, which has its origins in a model developed by Brandenburg & Subramanian (2005) for the evolution of magnetic helicity, and more recently modified by Sur *et al.* (2007) to allow for a vertical advection of magnetic helicity across the disc-halo boundary.

The model involves recognising α as the sum of kinetic and magnetic components, i.e., α=α_{k}+α_{m}, where the subscripts k and m represent the kinetic and magnetic quantities respectively and

$$\alpha_{\mathrm{k}}=-\frac{1}{3}\overline{\tau\boldsymbol{u}\cdot\nabla\times\boldsymbol{u}},\quad\alpha_{\mathrm{m}}=\frac{1}{3}\rho^{-1}\overline{\tau\boldsymbol{j}\cdot\boldsymbol{b}}, \tag{2.24}$$

with τ, the correlation time of the small scale velocity field $\boldsymbol{u}$, and ρ, the local gas volume density.

As in the quenching model, the α-effect is affected by the growth of the magnetic field. $\alpha_{\mathrm{k}}\propto l^{2}\Omega/h$ (Krause & Rädler, 1980), and is constant with respect to time in our model, so α_{m} must be constrained to be affected by the magnetic field similarly. Catastrophic quenching, as described in Sur *et al.* (2007), which hinders the evolution of the dynamo, can be avoided if the flux of magnetic helicity is non-zero. We introduce a transport equation for the helicity density (Subramanian & Brandenburg, 2006)

$$\frac{\partial\chi}{\partial t}+\nabla\cdot\boldsymbol{F}=-2\boldsymbol{\mathcal{E}}\cdot\boldsymbol{B}-2\eta\overline{\boldsymbol{j}\cdot\boldsymbol{b}}, \tag{2.25}$$

with χ, the helicity density of the small scale magnetic field, $\boldsymbol{b}$, and $\boldsymbol{F}$, the helicity flux density. The left hand side of the expression concerns the evolution with time and the removal of helicity from the disc, whereas the right hand side involves the generation of helicity.

We shall use a simple version of flux

$$\boldsymbol{F}=\chi\overline{\boldsymbol{U}},$$

which can be physically described by saying we have a helicity density, and are using a flow $\overline{\boldsymbol{U}}$ of some sort to move it. $\alpha_{\rm m}$ can be related to χ via

$$\alpha_{\rm m} \simeq \frac{1}{3}\tau\frac{1}{l_0^2}\frac{\chi}{\rho}. \tag{2.26}$$

With the identity $\eta_{\rm t} = 1/3\overline{\tau \boldsymbol{u}^2}$, we can rewrite the helicity density as

$$\chi = \rho\overline{\boldsymbol{u}^2}\alpha_{\rm m}\frac{l_0^2}{\eta_{\rm t}}. \tag{2.27}$$

With all but $\alpha_{\rm m}$ being constant with respect to time in this model, we can substitute this into Eq. (2.25)

$$\frac{\partial \alpha_{\rm m}}{\partial t} = -\frac{2\eta_{\rm t}}{l_0^2}\left(\frac{\boldsymbol{\mathcal{E}}\cdot\boldsymbol{B}}{\rho\overline{\boldsymbol{u}^2}} + \frac{\eta\overline{\boldsymbol{j}\cdot\boldsymbol{b}}}{\rho\overline{\boldsymbol{u}^2}}\right) - \nabla\cdot\left(\alpha_{\rm m}\overline{\boldsymbol{U}}\right). \tag{2.28}$$

It can be shown with the combination of Eqs. (2.26) and (2.27), and with the introduction of a reference magnetic field $B_{\rm eq}^2 = \rho\overline{\boldsymbol{u}^2}$, that the evolution of $\alpha_{\rm m}$ can be written (Sur *et al.*, 2007)

$$\frac{\partial \alpha_{\rm m}}{\partial t} = -\frac{2\eta_{\rm t}}{l_0^2}\left(\frac{\boldsymbol{\mathcal{E}}\cdot\boldsymbol{B}}{B_{\rm eq}^2} + \frac{\alpha_{\rm m}}{R_{\rm m}}\right) - \nabla\cdot\left(\alpha_{\rm m}\boldsymbol{U}\right), \tag{2.29}$$

where l_0 describes a typical length scale for the turbulence, here $l_0 = 0.1\,\mathrm{kpc}$. The choice of using $B_{\rm eq}$ as our reference magnetic field strength is an important one. It gives us a somewhat simple yet still illustrative impression of what we expect the magnetic field should look like in a gaseuos disc. It should be expected to be a measure of the upper limit of the magnitude of the magnetic field, demonstrating how any simulations should behave. $R_{\rm m} = \eta_{\rm t}/\eta \simeq 1\times10^5$ is the magnetic Reynolds number. The first term in Eq. (2.29) describes the amount of small-scale helicity created by the mean field dynamo. If nothing is done with this term, α is rapidly quenched. The second term, $\alpha_{\rm m}/R_{\rm m}$ is negligible as a result of the magnitude of $R_{\rm m}$. The final term is the advection term, which is used to remove the helicity created in the first term, and hence preventing catastrophic quenching.

Upon expansion of Eq. (2.29), and again taking the axisymmetric, no-z approximation, with a negligible magnetic field component in the z direction, and using the velocity profile, $\boldsymbol{U} = (0, r\Omega, U_z)$, we are left with

$$\frac{\partial \alpha_{\rm m}}{\partial t} = -\frac{2\eta_{\rm t}}{l_0^2}\left(\frac{\alpha\boldsymbol{B}^2}{B_{\rm eq}^2} - \eta_{\rm t}\frac{\boldsymbol{J}\cdot\boldsymbol{B}}{B_{\rm eq}^2} + \frac{\alpha_{\rm m}}{R_{\rm m}}\right) - \frac{\partial}{\partial z}\left(\alpha_{\rm m}U_z\right). \tag{2.30}$$

We have taken $U_r(r) = 0$ here, however we will use radial inflows later, and this will result in another term in Eq. (2.30). It was noted in Sur *et al.* (2007) that the term $\boldsymbol{J}\cdot\boldsymbol{B}$ vanishes under the no-z approximation. Under the axisymmetric no-z approximation, this term reduces to

$$-B_r\frac{B_\phi}{h}+B_\phi\frac{B_r}{h}-B_\phi\frac{\partial B_z}{\partial r}+\frac{B_z}{r}\frac{\partial(rB_\phi)}{\partial r},$$

which vanishes when it is assumed that B_z is negligible in relation to the other two components of magnetic field strength. In reality, this would not be the case, and the other terms would also not vanish, as the vertical derivatives would be different for each of the terms, so a move away from the no-z approximation is necessary.

It was shown in Appendix A of the same paper that a suitable approximation to the term to retain realism takes the form

$$\boldsymbol{J}\cdot\boldsymbol{B}\simeq-\frac{3}{8}\left(|\pi D|\right)^{1/2}B_rB_\phi, \tag{2.31}$$

where we make the modification whereby we use radially dependent quantities rather than mean values for the magnetic field components. We non-dimensionalise Eqs. (2.30) and (2.31), and rewrite them using the no-z approximation and take $B_0 = B_{\rm eq}$

$$\begin{aligned}\frac{\partial\alpha_{\rm m}}{\partial t} &= -\frac{2R_{U_z}U_z\alpha_{\rm m}}{h}-2\left(\frac{h_0}{l_0}\right)^2\Big[\left(\alpha_{\rm k}+\alpha_{\rm m}\right)\left(B_r^2+B_\phi^2\right)\\ &\quad+\left(\alpha_{\rm k}+\alpha_{\rm m}\right)^{1/2}\frac{3\left(|\pi D|\right)^{1/2}}{8R_\alpha}B_rB_\phi+\frac{\alpha_{\rm m}}{R_m}\Big].\end{aligned} \tag{2.32}$$

We have used generic cases for much of our initial work, particularly in the case of flows. Here we present some physical flow models for the enrichment of our model. We discuss both vertical outflows and radial inflows.

2.3 Physical models for vertical and radial flows

2.3.1 A physical model for U_z

We consider the assumption made in Sur *et al.* (2007) that material can be advected vertically from the galactic disc, and we adopt the mechanism of supernova explosions to facilitate this. We also consider a model of fountain flow of Shukurov *et al.* (2006) to describe the return of some of the magnetic material to the disc; and the effects of this on the dynamo.

We employ a model for vertical outflow developed by Shu *et al.* (2005), based on models of the ISM and supernovae evolution (McKee & Ostriker, 1977; Efstathiou, 2000) in which such advection is analytically postulated in terms of a wind. The model describes how such phenomena are related to observables such as gas density, star formation rate and structure within the galactic disc.

We do not follow from the beginning the model of Shu *et al.* (2005), as it has been shown that in some spiral galaxies (including our main study target, M31), the connection between the gas density in the disc and the star formation rate can be non-trivial and inconsistent (Kennicutt, 1989; Tabatabaei & Berkhuijsen, 2010). We hence begin from the star formation rate, which is an observable quantity.

We make the assumption that the star forming gas in the galaxy exists in the form of cold gas clouds surrounded by a warm ISM (McKee & Ostriker, 1977). The cold gas populates a certain fraction of the disc, given as a ratio of the cold gas density to the mean gas density, the cold gas volume filling factor, $f_{\rm c}$.

The star formation rate volume density is

$$\dot{\rho}_* = \dot{\mu}_*/2h_{\rm CO}, \tag{2.33}$$

with $h_{\rm CO}$, the scale height of the molecular hydrogen gas, where star formation takes place, and $\dot{\mu}_*$ the star formation rate surface density. From this we can infer a supernova explosion rate (Efstathiou, 2000)

$$S_{-13} = 10^{13}\frac{\dot{\rho}_*}{M_{\rm ps}}\,{\rm yr}^{-1}{\rm pc}^{-3}, \tag{2.34}$$

where $M_{\rm ps}$ is the mass of star formation required for one supernova explosion, taken to be $125{\rm M}_\odot$ (Shu *et al.*, 2005).

An expanding supernova explosion evaporates the surrounding ISM, and moves the local warm gas in the system. We adopt the evaporation parameter (a measure of the efficiency of a potential supernova explosion to evaporate the surrounding ISM) normalised to the value close to the solar neighbourhood (Efstathiou, 2000; Shu *et al.*, 2005),

$$f_\Sigma = 21.5\left(\frac{f_{\rm c}}{e^{-1}}\right)^{-1}\left(\frac{\gamma}{2.5}\right)\left(\frac{\phi_{\rm k}}{0.01}\right)^{-1}\left(\frac{a_{\rm l}}{\rm pc}\right)^2,$$

which incorporates the filling factor of the cold gas, f_c (we assume to be constant (McKee & Ostriker, 1977)), and the ratio of the supernova explosion wave velocity to the isothermal sound speed of the hot gas, γ, as used in Shu *et al.* (2005), ϕ_k is the efficiency

of conduction, of the order 0.1, and a_l is the lower limit of cloud radius. The hot cavities which result from the expansion of the supernovae remnants closely resemble bubbles. Should the kinetic energy in these bubbles be great enough, they can push through the ISM in bulk, and the sum of these events can be classified as an outflow, wind or fountain.

The hot phase temperature of the supernova explosion can be written as

$$T = 6.6 \times 10^5 \mathrm{K} \left(S_{-13} E_{51} \frac{f_\Sigma}{\gamma} \right)^{0.29}, \tag{2.35}$$

with E_{51}, the energy released by a supernova explosion. The isothermal sound speed of the moving gas can be calculated using $U_\mathrm{i} = 37 T_5^{1/2}\,\mathrm{km\,s^{-1}}$ (Efstathiou, 2000), where T_5 is the hot phase temperature measured in units of 10^5K, which, when considering conservation of specific enthalpy, gives a terminal wind speed $U_\mathrm{wind} = \sqrt{2.5} U_\mathrm{i}$ (Shu *et al.*, 2005), which can be rewritten using Eq. (2.35)

$$U_\mathrm{wind} = 5.18 \times 10^3 \left(\frac{\dot{\mu}_*}{h_\mathrm{CO}} \right)^{0.15} \left(\frac{f_\Sigma}{\gamma} \right)^{0.15} \mathrm{km\,s^{-1}}. \tag{2.36}$$

This wind model accounts for large scale vertical motions within the disc, being of the order of several hundred $\mathrm{km\,s^{-1}}$. On its own this model would quickly remove magnetic material from the disc, on timescales considerably smaller than the age of the galaxy. A modification to the mechanism is required to explain what happens next.

We adopt a model suggested in Section 2 of Shukurov *et al.* (2006), whereby the hot expanding gas from the supernova is travelling at these high velocities. The rising gas crosses the disc-halo boundary, and cools. Once it has lost enough heat it contracts and loses the kinetic energy which drove it upwards. It falls back to the disc in the form of the small clouds we had at the beginning of the model. This mechanism is labelled fountain flow. The return of some of the magnetic material to the disc prevents the dynamo from being subcritical in its evolution, and allows the magnetic field to grow.

This mass weighted velocity is defined via

$$U_z = f_\mathrm{h} U_\mathrm{wind} \frac{\rho_\mathrm{h}}{\rho}, \tag{2.37}$$

with f_h, the volume filling factor of the hot gas, typically of the order 0.2 at the galactic midplane (Korpi *et al.*, 1999), $\rho_\mathrm{h} \simeq 1.7 \times 10^{-27}\mathrm{g\ cm^{-3}}$ and $\rho \simeq 1.7 \times 10^{-25}\mathrm{g\ cm^{-3}}$, the mean hot and interstellar gas densities respectively. With this taken into account, we

can define our outflow velocity

$$U_z = 10\,\mathrm{km\,s^{-1}} \left(\frac{\dot{\mu}_*}{h_{\mathrm{CO}}}\right)^{0.15} \left(\frac{f_\Sigma}{\gamma}\right)^{0.15}. \tag{2.38}$$

We require a mass weighting because not all of the magnetic material is removed from the disc; most is considerably more dense. Our outflow model removes the hot ionised component, which is carried by the blast of the supernova. The ratio of the densities defines how much of the field is connected to the hot gas.

With f_Σ/γ being made up of a number of generalised constants (McKee & Ostriker, 1977; Shu *et al.*, 2005), we are left with a rather elegant expression for the outflow velocity in terms of only the star formation rate density and the molecular hydrogen scale height. It is surprising yet encouraging that we can end up with such a simple seeming solution following a considerable amount of working with a number of astrophysical quantities.

2.3.2 Interpretation of the vertical outflow model

One of the interesting and important outcomes from the testing of the model was the variation in pitch angle with the alteration of R_{U_z}. As shown in Fig. 4.11 (panel c), as the value of R_{U_z} is increased, the magnitude of the magnetic pitch angle also increases, in what would appear by eye to be a relatively linear fashion.

This can be explained by analysing the dynamo equations in the steady state. We reduce the mean field dynamo equations (Eqs. 2.20 and 2.21) by removing the radial derivative terms, setting $U_z(r) = 1$, $h(r) = 1$, $G = 1$ and by neglecting radial diffusion in the steady state

$$0 = -R_\alpha \alpha B_\phi - B_\mathrm{r} - R_{U_z} B_\mathrm{r}, \tag{2.39}$$

$$0 = R_\alpha \alpha B_\mathrm{r} - B_\phi - R_{U_z} B_\phi + R_\omega B_\mathrm{r}. \tag{2.40}$$

It is clear that the terms involving the outflow are of the same form in each equation, so we can take our analysis further to investigate

$$\frac{B_\mathrm{r}}{B_\phi} = -\frac{R_\alpha \alpha}{1 + R_{U_z}} \equiv -\frac{1 + R_{U_z}}{R_\alpha + R_\omega}, \tag{2.41}$$

where the middle term is the result for Eq. 2.39, and the right hand side is the result for Eq. 2.40. It is worth noting that it does not matter whether we assume α-quenching or a dynamical α, the outcome is the same.

If R_{U_z} is increased, the outflow removes more of the magnetic material from the disc, and hence a greater source of B_r is required. More of the azimuthal component, B_ϕ is

therefore comverted to radial magnetic field, and as a result, B_r/B_ϕ increases.

If we now take α to be constant in the steady state, we can rearrange Eq. 2.41 to solve for R_α, and find a quadratic relation

$$R_\alpha^2 + R_\omega R_\alpha - (1 + R_{U_z})^2 = 0, \tag{2.42}$$

which has the solutions

$$R_\alpha = -\frac{1}{2}R_\omega \pm \frac{1}{2}\sqrt{R_\omega^2 + 4\,(1 + R_{U_z})^2}. \tag{2.43}$$

Then, upon substituting this back into Eq. (2.41), we obtain the relation

$$\frac{B_\mathrm{r}}{B_\phi} = -\frac{R_\omega + \sqrt{R_\omega^2 + 4\,(1 + R_{U_z})^2}}{2\,(1 + R_{U_z})}, \tag{2.44}$$

leading to what we observe in Fig. 2.1. We have taken the positive square root in Eq. (2.43) as the negative solution gives physically unrealistic values significantly deviated from the model outputs.

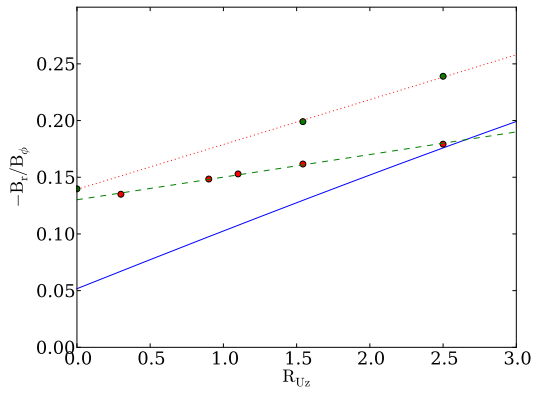

Figure 2.1: An analytical representation of the ratio between radial and azimuthal magnetic field components with varying R_{U_z}, given by Eq 2.44 (solid line). Green circles show the results for the α-quenching model and red circles show the results for the dynamical α model.

The ratio of magnetic field components is affected less by an increase in the magnitude of the outflow when using the dynamical α model.

2.3.3 A physical model for U_r

We have developed a model for vertical outflows in Chapter 2, and it is also possible to ascertain such a physically derived model for radial inflows.

The model takes its basis from the gas density in the disc, and the star formation rate. We make the assumption that in regions of high star formation, local gas will be used for star forming. Outside these regions, where star formation is low, gas will flow inwards towards the centre of the disc to feed the regions of star formation rate. It could be pictured that this is the case in the M31 galaxy, where a region of high gas density and star formation at $r \simeq 10\,\mathrm{kpc}$ from the galactic centre exists. Outside this region, star formation and gas density are both relatively small; analogous with theories of galaxy and star formation from clouds of gas, it could be assumed that at an earlier time, the gas in M31 was much more evenly distributed throughout the disc. Not dissimilar from theories of density fluctuations in the cosmic microwave background being connected with galaxy formation, density fluctuations could have led to the ring of high density in M31, and the surrounding regions of gas would have fed the higher density region. This defines how we are looking at the inflow here, we are assuming surrounding gaseous regions are feeding regions of star formation.

We begin with the continuity equation

$$\frac{\partial \rho_\mathrm{g}}{\partial t} + \nabla \cdot \left(\rho_\mathrm{g} \overline{\boldsymbol{U}}\right) = -\dot{\rho}_*, \tag{2.45}$$

where ρ_g is the volume gas density and $\dot{\rho}_*$ is the volume star formation rate density. We make the assumption that mass is conserved, so $\partial \rho_\mathrm{g}/\partial t = 0$. Eq. 2.45 can thus be rewritten

$$\frac{1}{r}\frac{\partial}{\partial r}\left(r \rho_\mathrm{g} U_r\right) = -\dot{\rho}_*, \tag{2.46}$$

when we make the assumption that we are only solving for U_r, and in our axisymmetric thin disc approximation, the other two terms vanish. Solving for U_r, we obtain

$$U_r = \frac{1}{r\rho_\mathrm{g}} \int_0^r -r' \dot{\rho}_* \left(r'\right) dr'. \tag{2.47}$$

———

Chapter 3

Verification and application of the dynamo model

Before we begin discussing the galaxies we wish to study, we briefly look at a number of generic and simple observationally constrained models which have been previously studied. This is useful for two reasons: in order to verify the code we shall use later, and in order to develop some understanding of how different components of the flow affect the dynamo generated magnetic field. We begin with a paper by Moss *et al.* (2000), looking at the role of radial velocities. We then consider the role of outflows from the disc, that were included in the generic galaxy model of Sur *et al.* (2007), and finally a dynamo model for the Andromeda galaxy M31 developed by Moss *et al.* (1998).

The code

Throughout these studies, we will be using our own code to solve the equations. We run a relatively simple third order Runge-Kutta time stepping loop to advance the model in time, and use second order forward finite difference methods to resolve derivatives in spatial dimensions. The code is written in Python. This method has proven very useful for using a lot of observational data easily, and collating a lot of results from single run simulations.

3.1 "Accretion and galactic dynamos": Moss *et al.* (2000)

In this study the evolution of a simple $\alpha\Omega$ dynamo was tested, with and without α-quenching, for a range of radial flows. The aim was to explore whether radial flows would suppress or enhance mean-field dynamo action in thin discs, following a suggestion in

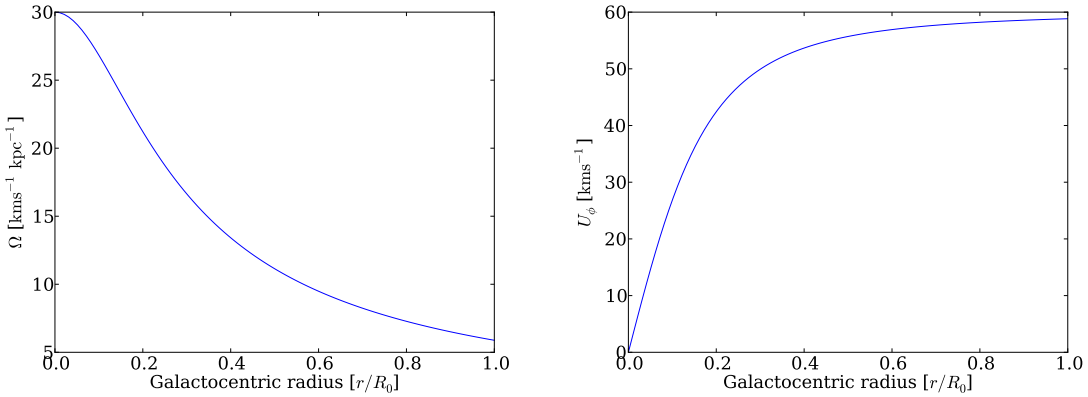

Figure 3.1: *Left panel*: Angular velocity calculated using the Brandt law, Eq. (3.3), with $\Omega_0 = 30\,\mathrm{km\,s^{-1}kpc^{-1}}$, and $r_\omega = 0.2R_0$. *Right panel*: Rotation curve for the Brandt rotation law calculated via $U_\phi = r\Omega(r)$.

Chiba & Lesch (1994), that an inflow would enhance the mean magnetic field of a barred galaxy. The paper by Moss *et al.* (2000), as we shall see, dispels such a hypothesis, by showing that the magnetic field would be suppressed with the inclusion of inflows.

The dimensionless equations solved were a version of our Eqs. (2.20) and (2.21)

$$\frac{\partial B_r}{\partial t} = -\lambda R_{U_r}\frac{U_r}{r}\frac{\partial}{\partial r}(rB_r) - R_\alpha \alpha B_\phi - B_r + \lambda^2\frac{\partial}{\partial r}\left[\frac{1}{r}\frac{\partial}{\partial r}(rB_r)\right], \tag{3.1}$$

$$\frac{\partial B_\phi}{\partial t} = -\lambda R_{U_r}\frac{\partial}{\partial r}(U_r B_\phi) + R_\omega r B_r\frac{\partial \Omega}{\partial r} - B_\phi + \lambda^2\frac{\partial}{\partial r}\left[\frac{1}{r}\frac{\partial}{\partial r}(rB_\phi)\right], \tag{3.2}$$

with the exception that in this model, there is no flaring of the disc, i.e. $h(r) = h_0$. This model differs considerably from the generalised dynamo system introduced in the previous chapter. Along with the flattening of the gaseuos disc, we consider a system without vertical outflows, and we consider α to be constant with respect to radius. We also consider the $\alpha\Omega$ dynamo whereby the term involving α in the expression for the azimuthal magnetic field component is removed (the dynamo model in Chapter 2 was the $\alpha^2\Omega$ dynamo).

Moss *et al.* (2000) used the dimensional Brandt rotation law

$$\Omega(r) = \frac{\Omega_0}{\left[1 + (r/r_\omega)^2\right]^{1/2}}, \tag{3.3}$$

which is a commonly used generic description for the rotation of galactic discs. It

describes the angular velocity of the disc, $\Omega(r)$, allowing for the flattening of the rotation curve, U_ϕ, in the outer regions of the disc, where r_ω determines the radius at which U_ϕ flattens (Fig. 3.1).

Using the values of Moss *et al.* (2000) of $h = 500\,\mathrm{pc}$, $R_0 = 10\,\mathrm{kpc}$, $\Omega_0 = 30\,\mathrm{km\,s^{-1}kpc^{-1}}$, $\alpha_0 = 0.65\,\mathrm{km\,s^{-1}}$ and $\eta_\mathrm{t} = 1.0 \times 10^{26}\mathrm{cm^2 s^{-1}}$, we obtain an associated diffusive timescale of $t_0 = 7.5 \times 10^8$ yr, and dimensionless values of $\lambda = 0.05$, $R_\alpha = 1.0$, and $R_\omega = 10.0$, which can be considered typical values for galactic discs.

The linear growth rate of the magnetic field is given by

$$\Gamma = \frac{\mathrm{d}\ln|\boldsymbol{B}|}{\mathrm{d}t},$$

where $|\boldsymbol{B}| = \sqrt{B_r^2 + B_\phi^2}$ and B_r and B_ϕ are averages over all radii. The growth rate describes how the magnetic field evolves over time.

The boundary conditions adopted by Moss *et al.* (2000) at the inner boundary are $B_r = B_\phi = 0$ when the inner boundary is at $r_{min} = 0$ (we shall call this type a 'zero' boundary condition), and $\partial B_r/\partial r = \partial B_\phi/\partial r = 0$ (we shall call this type a 'flat' boundary condition), when $r_{min} \neq 0$. We apply flat boundary conditions throughout at the outer radius. Here, in addition to reproducing the results of Moss *et al.* (2000), we shall investigate the effect that changing the inner boundary condition can have on the results.

Fig. 3.2 shows the results of this first test. We observe magnetic field growth at the expected growth rate of 0.8 (Moss *et al.*, 2000), for both sets of boundary conditions, with the run using flat boundary conditions taking slightly longer to reach that rate. We also notice very similar magnetic pitch angles, p, with the exception of a slight opening of the angle in the inner regions of the disc for the flat boundary conditions, where the field profiles differ, depending on the type of boundary condition.

The locality of the field growth is of interest as it is related to the local dynamo number, which is not constant. We calculate the local dynamo number for this model

$$D(r) = R_\alpha R_\omega r \frac{\partial\Omega}{\partial r}, \tag{3.4}$$

and see in Fig. 3.3, that the magnitude of the dynamo number is largest around $r/R_0 = 0.3$. This can be explained by the high value of $\partial\Omega/\partial r$ at this radius, as is apparent in Fig. 3.1.

So, we have successfully reproduced the expected growth rate of 0.8 in order to validate our code, and got a small insight into some other aspects of the dynamo model, namely, how the inner boundary condition can alter the magnetic pitch angle and the

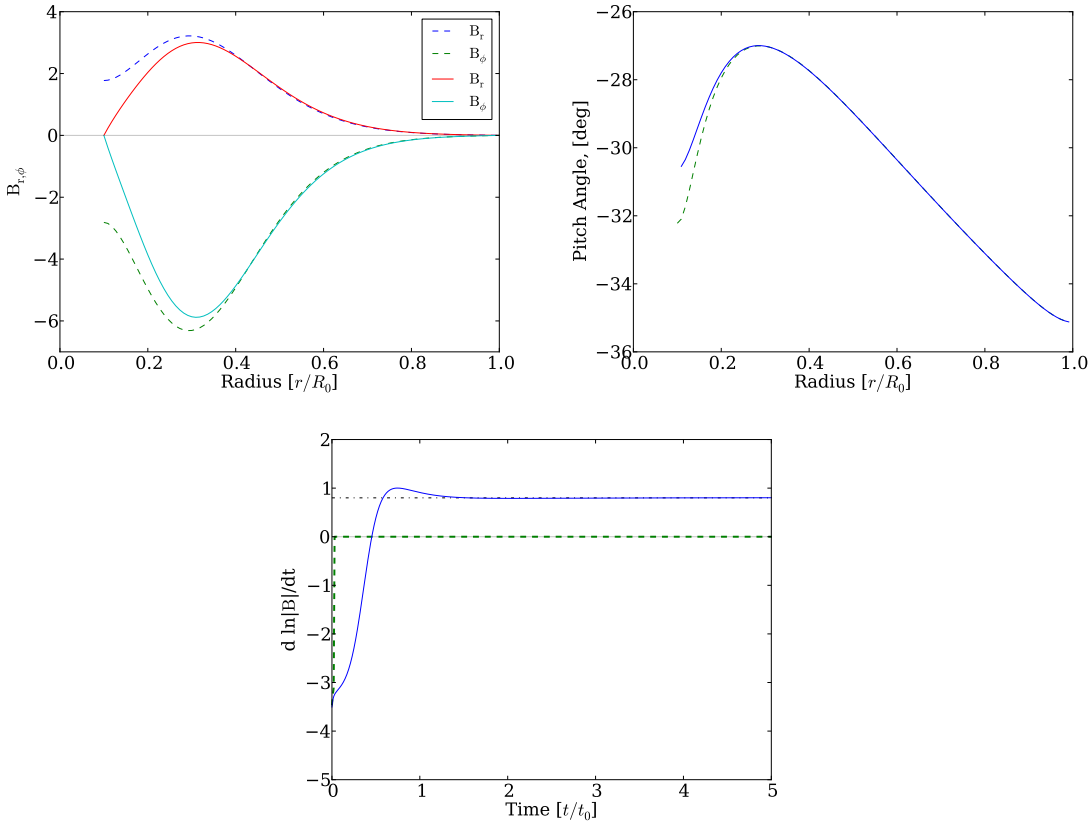

Figure 3.2: *Upper left panel*: Radial and azimuthal magnetic field components, with no inflow, i.e. $R_{U_r} = 0$. *Upper right panel*: The pitch angle of the magnetic field, with $R_{U_r} = 0$. *Lower panel*: Growth rate of the magnetic field with $R_{U_r} = 0$. The dash-dot line represents the $\Gamma = 0.8$ growth rate found by Moss *et al.* (2000), using zero boundary conditions. In all panels, zero (solid lines) and flat (dashed lines) boundary conditions are used. Time is measured in units of $h_0^2/\eta_t = 7.5 \times 10^8$ yr.

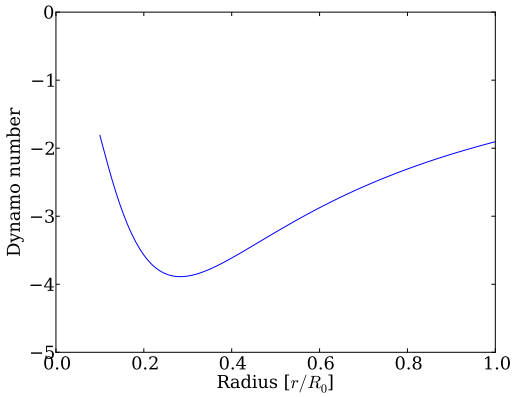

Figure 3.3: Local dynamo number, calculated using Eq. (3.4). Note its negative magnitude as a result of the gradient of $\Omega(r)$ always being negative.

growth rate. We also see that the field growth can be strongly localised due to variations in the local dynamo number, even for this idealised (smooth) galaxy model.

3.1.1 The effect of an inflow

The next step we take in advancing the model is to include a small radial inflow, superimposed on the stronger galactic rotation.

We introduce the radial velocity component

$$U_r = -\frac{0.05}{r}\exp\left(\frac{r}{r_e}\right), \tag{3.5}$$

where r_e is a term of order unity used to enhance or suppress the exponential.

Here, we take slightly more realistic values for the parameters, and choose $R_\alpha = 1.0$, $R_\omega = 20.0$ and $\lambda = 1/30$, which are closer to parameters for a galaxy such as the Andromeda Nebula[1].

Firstly, we set $R_{U_r} = 0$, and show the results in Fig. 3.4.

The magnetic field profile in this case, in contrast to Fig. 3.2, is more strongly concentrated around $r/R_0 = 0.3$, and the magnitude of the azimuthal magnetic field is larger in proportion to the radial component than it was in the setup of Fig. 3.2. This affects the pitch angle, reducing its magnitude by about 7°.

[1] Note that there is a small error in Moss *et al.* (2000), where $r_e = 1/3$ is specified but $r_e = 3$ is used, and tabulated results refer to $R_\omega = 10$, whereas the text to $R_\omega = 20$

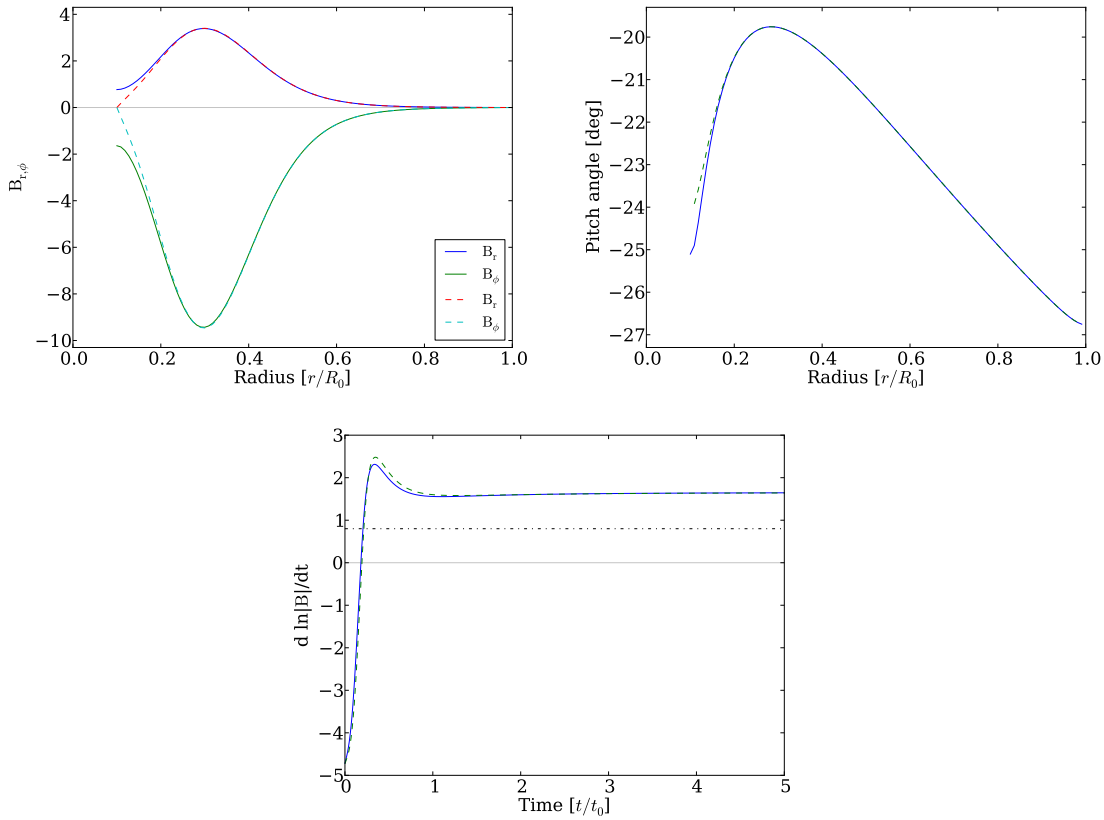

Figure 3.4: *Upper left panel*: Radial and azimuthal magnetic field components, with $R_\omega = 20$ and $R_{U_r} = 0$. *Upper right panel*: The pitch angle of the magnetic field, with $R_\omega = 20$ and $R_{U_r} = 0$. *Lower panel*: Growth rate of the magnetic field, with R_ω and $R_{U_r} = 0$. The dash-dot line represents the original $\Gamma = 0.8$ growth rate quoted in Moss *et al.* (2000). In all panels flat boundary conditions are shown as solid lines and zero boundaries using dashed lines.

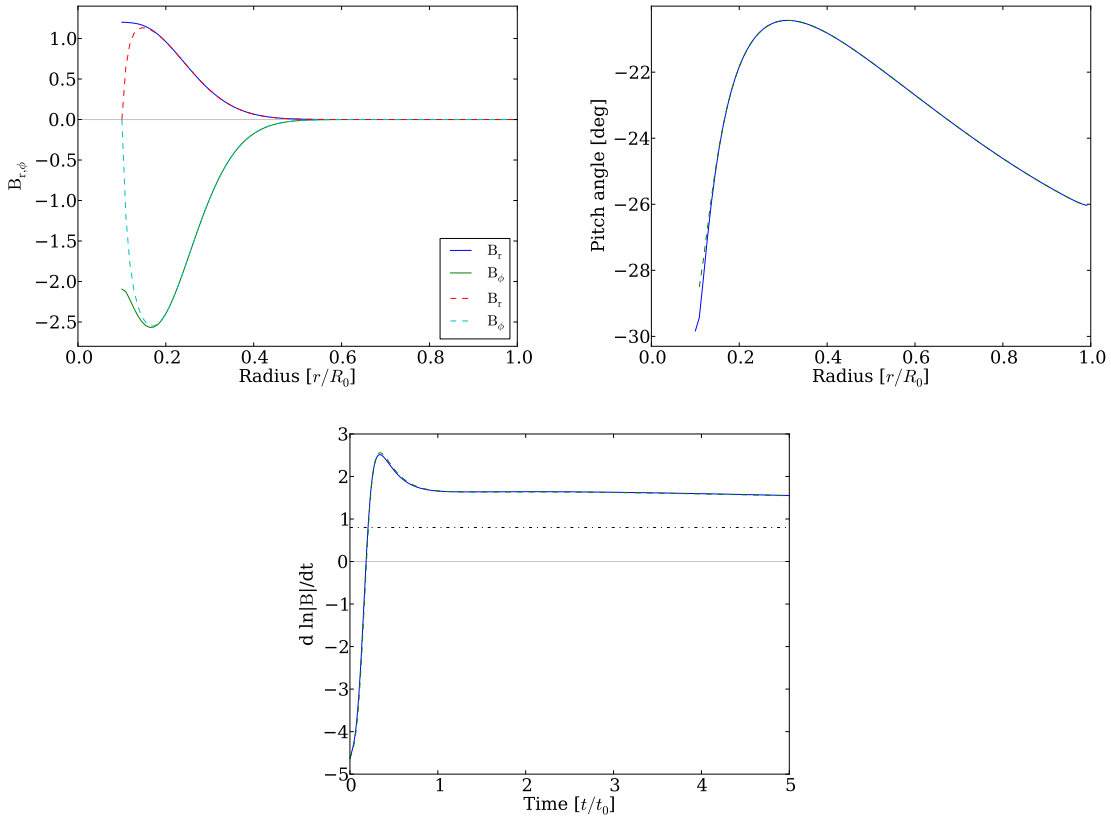

Figure 3.5: *Upper left panel*: Radial and azimuthal magnetic field components, with $R_\omega = 20$ and $R_{U_r} = 4$. *Upper right panel*: The pitch angle of the magnetic field, with $R_\omega = 20$ and $R_{U_r} = 4$. *Lower panel*: Growth rate of the magnetic field, with R_ω and $R_{U_r} = 4$. The dash-dot line represents the original $\Gamma = 0.8$ growth rate quoted in Moss *et al.* (2000). In all panels flat boundary conditions are shown as solid lines and zero boundaries using dashed lines.

We obtain a growth rate of $\Gamma = 1.61$, just over twice that of the first run. We can attribute this to the doubling of R_ω, and the reduction of λ which reduces the effect of the diffusive term in the equations, further enhancing the ability of the magnetic field to grow.

3.1.2 Switching on the inflow

Now we switch on the inflow. We use the same parameters as we did in Section 3.1.1, and set $R_{U_r} = 4$. The results are shown in Fig. 3.5.

The magnetic field is now confined to a smaller region towards the centre of the disc, and is of considerably smaller magnitude. Physically, including the inflow has moved the

magnetic material inwards towards the centre of the disc. These results match those of Moss *et al.* (2000). Note we are not reproducing the growth rates from Table 1. of Moss *et al.* (2000), which used a separate set of values of R_U. We also notice a small increase in the pitch angle as a result of switching on the inflow.

3.1.3 α-quenching

We now introduce α-quenching to the model to investigate the effects on the evolution of the dynamo.

We include a model of numerical α-quenching similar to models we have already discussed

$$\alpha \propto \frac{1}{1 + \boldsymbol{B}^2},$$

and also reset $R_{U_r} = 0$. Otherwise, the parameters chosen are the same as in Section 3.1.2. The results are shown in Fig. 3.6.

We obtain very different results with α quenching, in each of the magnetic field strength, magnetic pitch angle and the growth rate. It can be seen that the magnetic field is now more evenly distributed throughout the disc.

We also observe a large decrease in the magnetic pitch angle throughout the entire disc, since the azimuthal field grows at a quicker rate than the radial component. As the field grows, the term involving R_α in the equation for the radial field decreases in magnitude, leading to a slower growth rate of B_r, and hence smaller pitch angles.

The growth rate undergoes the largest change in this regime. In the previous examples with the constant α, we observed permanent growth, however, here it is not the case. As we can see from the lower panel of Fig. 3.6, after a period of growth as in the other model, the growth rate decreases to zero and never recovers. This is exactly as we expect the non-linearity of the α- quenching to evolve. The magnetic field grows, quenching α, until a steady state is reached, where both $\boldsymbol{B}$ and α have saturated, and no more growth occurs.

3.1.4 Inflow with α-quenching

Finally, we switch on the inflow with $R_{U_r} = 4$, the value we used in Section 3.1.2. The results shown in Fig. 3.7 are the same as those shown in Moss *et al.* (2000).

Again, as in Section 3.1.2, we observe a concentration of the magnetic field towards the inner regions of the disc in the presence of an inflow. We also see the decrease in the magnitude of the magnetic field components.

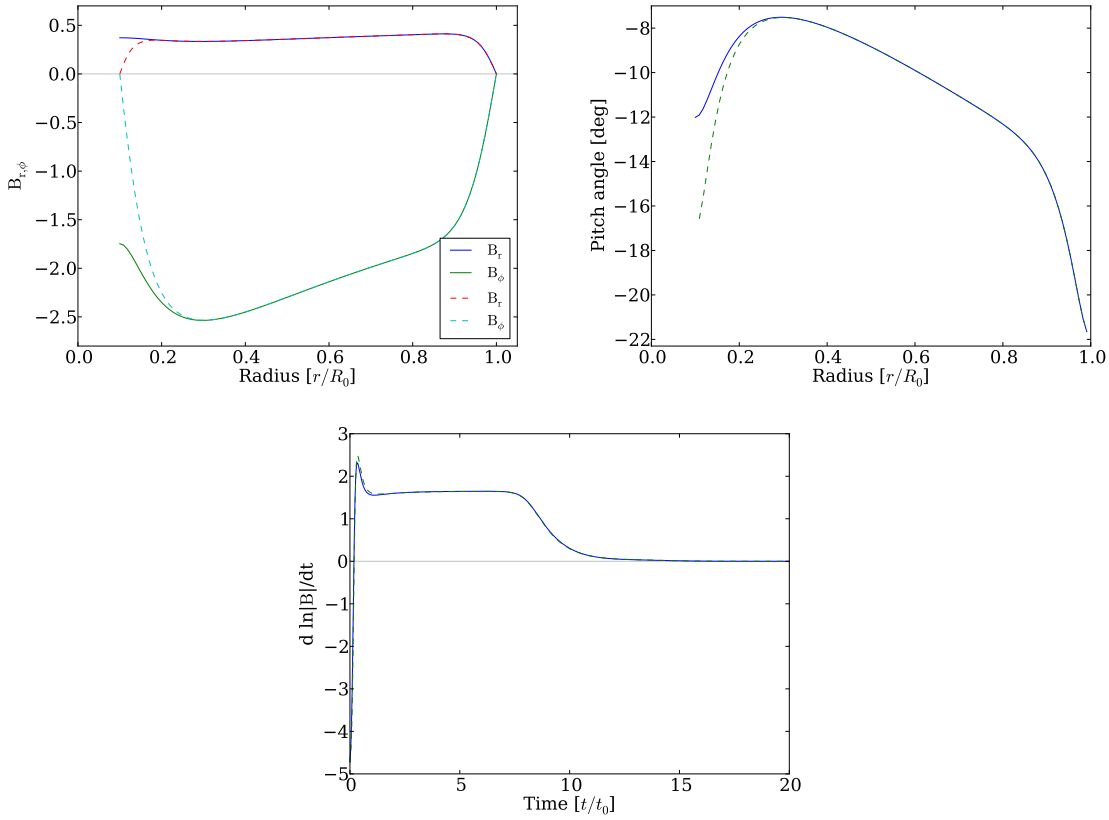

Figure 3.6: *Upper left panel*: Radial and azimuthal magnetic field components, with $R_{U_r} = 0$ and α-quenching. *Upper right panel*: The pitch angle of the magnetic field, with $R_{U_r} = 0$ and α-quenching. *Lower panel*: Growth rate of the magnetic field, with $R_{U_r} = 0$ and α- quenching. In all panels flat boundary conditions are shown as solid lines and zero boundaries using dashed lines.

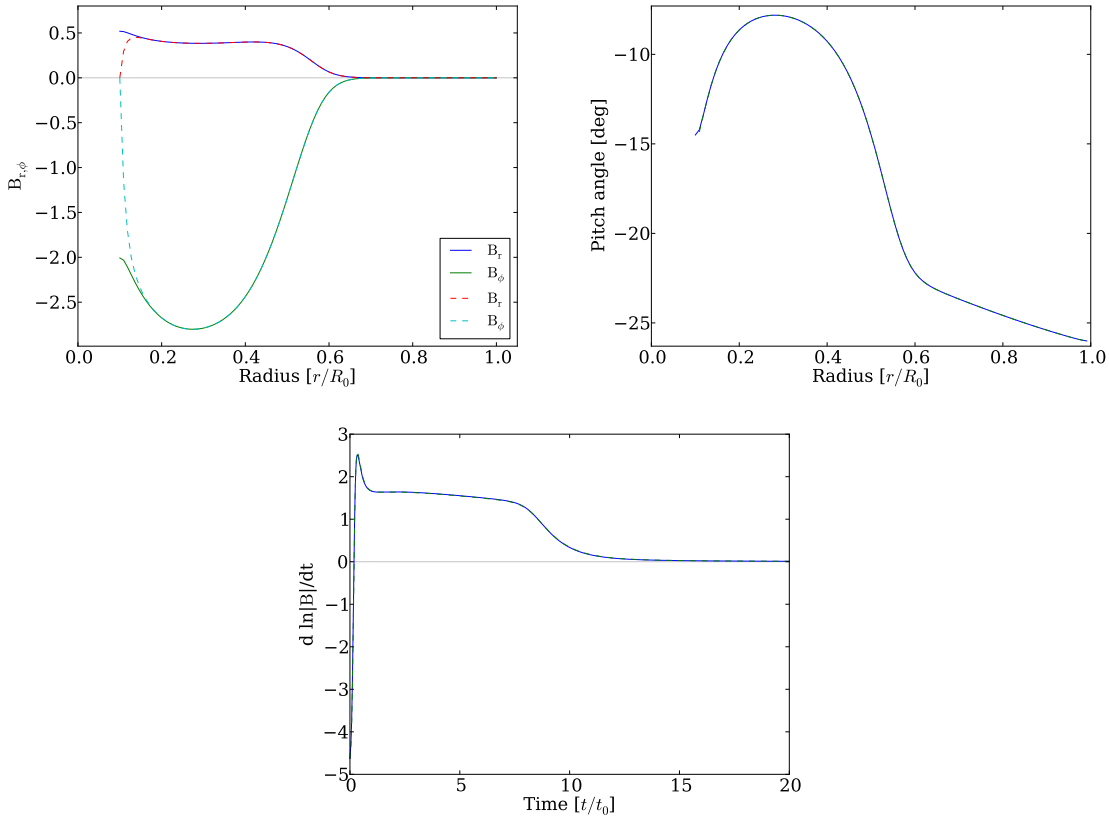

Figure 3.7: *Left panel*: Radial and azimuthal magnetic field components, with $R_{U_r} = 4$ and α-quenching. *Right panel*: The pitch angle of the magnetic field, with $R_{U_r} = 4$ and α-quenching. *Lower panel*: Growth rate of the magnetic field, with $R_{U_r} = 4$ and α- quenching. In all panels flat boundary conditions are shown as solid lines and zero boundaries using dashed lines.

The magnetic pitch angle has a very different profile in this example. Outside the inner region, the magnetic field does not grow, and hence the α-effect cannot be quenched, and as a result, the pitch angle takes similar values to that of the earlier example where there was no α-quenching and no inflow.

We have now completed our reproduction of this work, and have gained a good insight into how the model works mathematically. We have verified our code, and shown it to work for a generic model with a number of parameter changes and modifications. We have seen that boundary conditions have some effect on the growth rate of the magnetic field, and the pitch angle, although this is strongly localised to the boundary regions and does not propagate through the rest of the disc. We have also shown that non-azimuthal flows affect the magnetic pitch angle, an interesting result which will become more important shortly.

3.2 "Galactic dynamos supported by magnetic helicity fluxes": Sur *et al.* (2007)

Now we follow the work of Sur *et al.* (2007), where magnetic helicity advection was used to model the evolution of the α-effect. Again, we shall reproduce their main results, in order to validate our code, but we will also critically discuss some of the results in order to gain useful insight for the interpretation of our own model in Chapters 4 to 7.

In contrast to the last section, where we considered a radial inflow, here the model concerns vertical advection out of the galactic disc. This model is again treated rather differently to the previous two models. We do not vary quantities with radius here, choosing to only focus on the generalised evolution of the terms. We take the kinetic component of the α-effect, $\alpha_{\rm k}$ to be constant and equal to 1, and evolve the magnetic component, $\alpha_{\rm m}$ in time. As we are not varying quantities with radius, disc flaring is not considered, and here we are only considering vertical flows, not radial ones.

We assume a constant vertical velocity, U_z profile which does not vary with radius. With this taken into account we can rewrite Eqs. (2.20), (2.21) and (2.32) for the mean-field dynamo and magnetic component of the α-effect

$$\frac{\partial \overline{B}_r}{\partial t} = -\frac{2}{\pi} R_\alpha \left(1 + \alpha_{\rm m}\right) \overline{B}_\phi - \left(R_{U_z} + \frac{\pi^2}{4}\right) \overline{B}_r, \tag{3.6}$$

$$\frac{\partial \overline{B}_\phi}{\partial t} = R_\omega \overline{B}_r - \left(R_{U_z} + \frac{\pi^2}{4}\right) \overline{B}_\phi, \tag{3.7}$$

$$\frac{\partial \alpha_{\rm m}}{\partial t} = -R_{U_z}\alpha_{\rm m} - C\left[(1+\alpha_{\rm m})\left(\overline{B}_{\rm r}^2 + \overline{B}_{\phi}^2\right) + (1+\alpha_{\rm m})^{1/2}\,\frac{3\,(-\pi D)^{1/2}}{8R_\alpha}\overline{B}_{\rm r}\overline{B}_{\phi} + \frac{\alpha_{\rm m}}{R_{\rm m}}\right], \tag{3.8}$$

where $C = 2\,(h_0/l_0)^2$, and the terms involving R_{U_z} in this case are those which include the vertical component of velocity, U_z, instead of those which included the radial component in the previous section.

Another modification to this model regards the replacement of z- derivatives with ratios to derive the no-z equations. In Eqs. (3.6)-(3.8), instead of replacing the second vertical derivatives with $-1/h^2$, we use $-\pi^2/4h^2$, and replace α with $(2/\pi)\,\alpha$. This was done following work done by Phillips (2001), in which it was shown that these coefficients enhanced the accuracy of no-z dynamo models, bringing results closer to asymptotic results for equivalent models. We shall discuss this result further in Section 3.2.1.

The initial conditions are

$$\overline{B}_{\rm r} = 0, \quad \overline{B}_{\phi} = 10^{-3}, \quad \alpha_{\rm m} = -10^{-3}.$$

The dynamo number, $D = R_\alpha R_\omega$ is constant in this model, and the critical dynamo number, $D_{\rm cr}$ is

$$D_{\rm cr} = -\frac{\pi}{2}\left(R_{U_z} + \frac{\pi^2}{4}\right)^2, \tag{3.9}$$

obtained from Eqs. (3.6) and (3.7) in their steady states, with $\alpha_{\rm m} = 0$. For $R_{U_z} = 0$, the critical dynamo number is $D = -9.6$. The parameter values are $R_\alpha = 1$, $R_{\rm m} = 10^5$, $R_\omega = -15$, and $C = 50$, as used by Sur *et al.* (2007). The value of R_ω is negative in this model because the shear was taken to be of order unity as radial derivatives were not considered.

Figure 3.8 demonstrates perfect agreement with Sur *et al.* (2007), and allows us to gain more insight into what happens in the model. As discussed before, we see that for either zero or very low values of R_{U_z}, the magnetic field grows linearly, until $\alpha_{\rm m}$ becomes of significant magnitude. Then, as a result of the small vertical velocities not being able to remove enough small scale magnetic helicity from the disc, $-\alpha_{\rm m}$ increases in magnitude until the dynamo is subcritical, and the magnetic field decays to a minimum value, several orders of magnitude less than we might expect from observations. As $\alpha = \alpha_{\rm k} + \alpha_{\rm m} = 1 + \alpha_{\rm m}$ here, if $|-\alpha_{\rm m}|$ grows too large, then α decreases below a critical value, $\alpha_{\rm crit}$, whereby below this value, the dynamo number is subcritical.

It is only when R_{U_z} is increased, that we begin to see enough magnetic helicity being

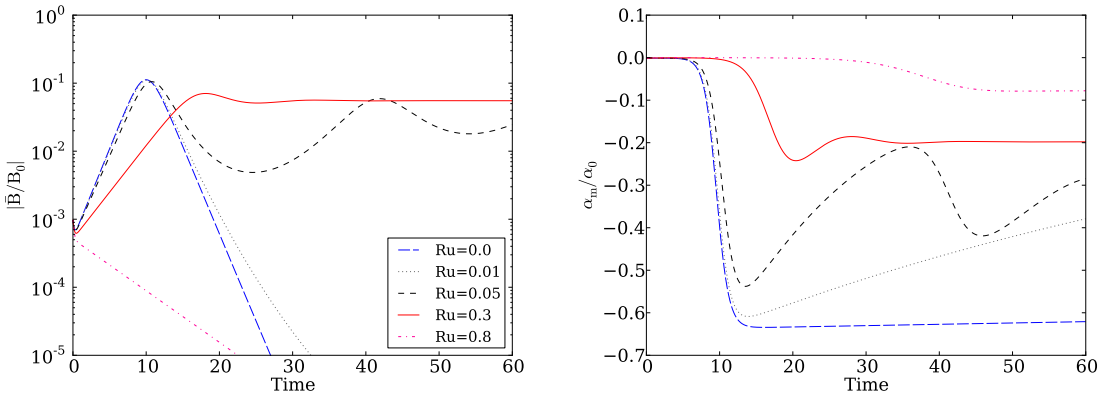

Figure 3.8: *Left panel*: A reproduction of Fig. 2 from Sur *et al.* (2007), using identical values of R_{U_z}, with $B_0 = 5\mu$G *Right Panel*: Evolution of the magnetic component of the α-effect as a function of time, for the same model, for the same values of R_{U_z} in the left panel, with $\alpha_0 = 1\,\mathrm{km\,s^{-1}}$. Time is measured in diffusion times, $t_\mathrm{d} \simeq 10^7$yr.

removed from the disc to allow the magnetic field to saturate at higher levels, and we find an optimum value of $R_{U_z} = 0.3$, as in Sur *et al.* (2007). Above this value, the magnetic field is removed more rapidly, and the field saturates at a lower magnitude. As we increase R_{U_z} further, in this case only as high as 0.8, we see that even the linear growth phase of the field is prohibited, and it simply decays.

An important result is the level of saturation of the magnetic field. Fig 3.8 shows the magnetic field saturating at roughly 1/10 of the equipartition field strength, rather than at the equipartition level as observations of some galaxies suggest. This was a result noted in Sur *et al.* (2007), and earlier obtained in Shukurov *et al.* (2006). In Sur *et al.* (2007), it was noted that another flux of magnetic helicity, the Vishniac-Cho flux (Vishniac & Cho, 2001) was expected to be present alongside the advective flux, and this would lead to higher saturation levels, of the order B_eq. We do not include the Vishniac-Cho flux in our model, so in future sections involving the dynamical α, we will expect to see saturation of the magnetic field at levels much lower than equipartition. The possibility of including the Vishniac-Cho flux would be a good next step in the investigation of these models; however due to its increased level of complexity we do not include it in the remainder of this study. In the cases where we find much lower than equipartition saturation, we will normalise our results appropriately in order to compare with observations. This low level of saturation could also have its roots in terms such as the approximation for $\boldsymbol{J} \cdot \boldsymbol{B}$, where coefficients of magnitude 2 may be missing. These factors of two arise when considering how the problem is tackled. Various groups use

R_ω	λ	r_ω	Γ $(1/h^2)$	Γ $(\pi^2/4h^2)$
5	0.025	0.2	0.32	-1.14
5	0.05	0.2	0.26	-1.214
10	0.05	0.2	0.81	-0.663
10	0.01	0.2	0.93	-0.536
10	0.10	0.2	0.63	-0.838
10	0.05	0.1	0.64	-0.830
10	0.05	0.4	0.88	-0.587
25	0.05	0.2	1.91	0.441

Table 3.1: Reproduction of the growth rates of Phillips (2001), for the linear evolution of the mean field equations, in their original form (column 4), and with the replacement of the second derivatives in z with $\pi^2/4h^2$ (column 5). The dimensional time scaling used in the evolutionof the model was $t_0 = h_0^2/\eta_t$.

slightly different methods for judging the α-effect, and from this there are a number of different outcomes, and factors of 2 between groups occasionally surface.

3.2.1 Modifications to the no-z approximation for galactic dynamos

We mentioned in the previous section a set of coefficients introduced by Phillips (2001) in order to increase the accuracy of no-z dynamo models. In this section we discuss this further by again, using a version of Eqns. (2.20) and (2.21) with a couple of simplifications.

Again, we solve the simple no-z mean field equations with $R_{U_{r,z}} = 0$ and $h(r) = 1$

$$\frac{\partial B_r}{\partial t} = -R_\alpha \alpha B_\phi - B_r + \lambda^2 \left(\frac{\partial}{\partial r} \left[\frac{1}{r} \frac{\partial}{\partial r} (r B_r) \right] \right), \tag{3.10}$$

$$\frac{\partial B_\phi}{\partial t} = R_\omega r B_r \frac{\partial \Omega}{\partial r} - B_\phi + \lambda^2 \left(\frac{\partial}{\partial r} \left[\frac{1}{r} \frac{\partial}{\partial r} (r B_\phi) \right] \right), \tag{3.11}$$

using the Brandt rotation curve defined by Eq. (3.3).

We firstly set $R_\alpha = 1$, and vary R_ω and λ, using constant α (no numerical quenching), for the no-z model without and with the coefficient of $\pi^2/4$ preceding the second z-derivatives, and show the linear growth rates in columns 4 and 5 of Table 3.1. We find a perfect agreement with the results in Phillips (2001).

However, a notable difference between the two models not previously discussed is the ability of the dynamo to operate. We see in the model without the $\pi^2/4$ coefficients, that for a large range of parameter choices, the magnetic field grows, whereas in the model

R_α	$\alpha\omega$	$\alpha\omega$ $(\pi^2/4)$	$\alpha^2\omega$	$\alpha^2\omega$ $(\pi^2/4)$
0.00	o	o	o	o
0.25	+	o	+	o
0.50	+	o	+	o
0.75	+	o	+	o
1.00	+	o	+	o
1.25	+	o	+	+
1.50	+	+	+	+
1.75	+	+	+	+
2.00	+	+	+	+
2.25	+	+	+	+
2.50	+	+	+	+
2.75	+	+	+	+
3.00	+	+	+	+

Table 3.2: Demonstration of the values of R_α required for the onset of dynamo action. A "o" represents decaying solutions, and a "+" denotes solutions where either the solutions grow continuously or remain positive or zero. The columns headed with $\pi^2/4$ show the results when this coefficient is used to replace $\partial^2/\partial z^2$

with the coefficient, only high values of R_ω permit the growth rate to remain above zero.

To put this into context, we now consider the galaxy M31. Based on observed quantities, suitable parameters for this model would be $R_\omega \simeq 19$ and $\lambda \simeq 0.02$ (refer to Chapter 4 for further discussion on these parameters). We also use the observed M31 rotation curve Chemin *et al.* (2009), and use standard α-quenching. We use $R_\alpha \simeq 0.7$, corresponding to a value of $\alpha_0 = 0.5\,\mathrm{km\,s^{-1}}$.

For the $\alpha\Omega$ dynamo as modelled above, and without the $\pi^2/4$ coefficient suggested, we obtain a linear growth rate of 1.32. However, with the coefficient included, we obtain a growth rate of -0.139, suggesting that the dynamo model would fail for the M31 galaxy.

Before we disregard the coefficients based on a single run, we must conduct further investigations to assess the issue. In order to address this point, we perform a set of runs for both the $\alpha\Omega$, and $\alpha^2\Omega$ models. Having done a number of runs with varying R_ω and λ, we now fix these to the values we have introduced for the M31 galaxy. Now, the parameter we vary will be R_α, in order to see when the onset of dynamo action occurs. We show the results of this test in Table. 3.2, and Fig. 3.9.

These results give a much greater insight into the working of both models. We see that both $\alpha\Omega$ and $\alpha^2\Omega$ dynamos have very similar thresholds of R_α for the onset of dynamo action. Our problem arises when we include the $\pi^2/4$ coefficient in the equations. For both models, it increases the threshold to $R_\alpha = 1.25$ and $R_\alpha = 1.0$ for the $\alpha\Omega$ and

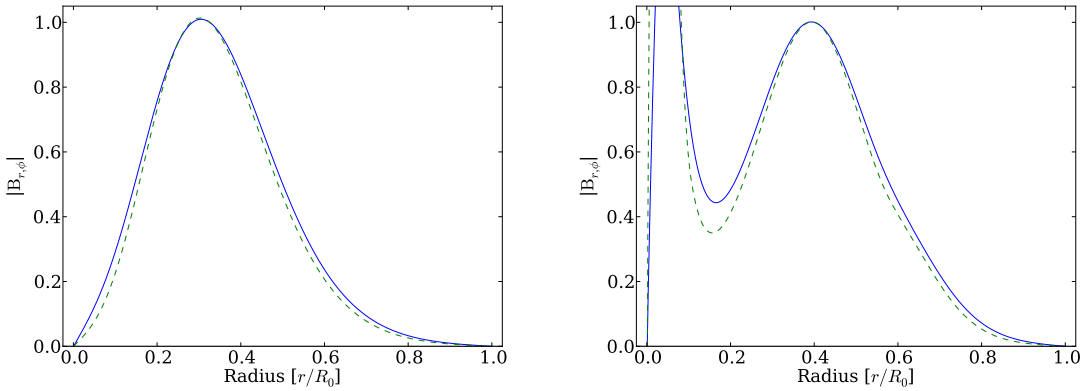

Figure 3.9: *Left panel*: Normalised radial and azimuthal magnetic field components (solid and dashed lines respectively), for the model using the Brandt rotation curve, and $R_\alpha = 1.0$. *Right panel*: Normalised radial and azimuthal magnetic field components (solid and dashed lines respectively), for the model using the M31 rotation curve, and $R_\alpha = 0.5$.

$\alpha^2\Omega$ models respectively. These values correspond to values of $\alpha_0 \geq 0.81\,\mathrm{km\,s^{-1}}$ and $\alpha_0 \geq 0.65\,\mathrm{km\,s^{-1}}$ respectively. This is restrictive in that for the model we will study when dealing with real galaxies, we shall be using a value of $\alpha_0 = 0.5\,\mathrm{km\,s^{-1}}$, below the threshold we observe here.

For this reason, we choose not to include the modified coefficients from this point onwards. This gives us more flexibility in choosing what we already understand to be a loosely defined quantity.

We must also note that there is a small typing error in the paper by Phillips (2001). In the final set of updated dynamo equations (not numbered), the $\pi^2/4$ coefficients are placed wrongly on the terms involving λ, instead of those which involved the second derivatives in z.

3.3 The Magnetic field of M31

3.3.1 "The nature of the magnetic belt in M31": Moss *et al.* (1998)

Finally in this chapter we look at a dynamo model for the galaxy M31 by Moss *et al.* (1998). This work focussed on the reproduction of the observed concentration of regular magnetic field in a ring at a radius of 10 kpc (Pooley, 1969; Berkhuijsen, 1977; Berkhuijsen *et al.*, 1983; Beck, 1982; Beck & Graeve, 1982; Beck *et al.*, 1980, 1989, 1996, 1998), using the observed rotation curve and disc scale height of Braun (1991), and the H I and CO gas density observations from Cram *et al.* (1980) and Dame *et al.* (1993) respectively, all

shown in Fig. 3.10.

Moss *et al.* (1998) did not use the no-z model for a thin disc dynamo, but used a 2-dimensional model involving z as well as r. We wish to see if our no-z model can reproduce the main features of their M31 model, and then to examine how the derived magnetic field changes as a result of new observational data on the rotation curve and gas density distribution of M31.

Firstly, we note the differences to the models discussed previously. Now we use a flared disc

$$\frac{h\left(r\right)}{1\,\mathrm{kpc}}=\begin{cases}0.2\left(1+r/16\,\mathrm{kpc}\right) & \text{for } r\leq 16\,\mathrm{kpc},\\ 0.4+0.016\left(r/\,\mathrm{kpc}-16\right) & \text{for } r>16\,\mathrm{kpc},\end{cases} \tag{3.12}$$

which was derived by Moss *et al.* (1998) from observations of the H I disc of M31 (Braun, 1991). This model is not that of an exponential disc, but rather two linear fits to the observational data. There are two fits because outside 16 kpc the disc appears, from the limited number of data points available, to increase in scale height more rapidly than within this radius. The disc aspect ratio for M31 is $\lambda\simeq 0.02$ at $R=25\,\mathrm{kpc}$, and $\lambda=0.03$ at $R=10\,\mathrm{kpc}$, so the degree of flaring is small.

This model uses numerical α-quenching, and α is derived from the rotation of the disc and the turbulent length scale

$$\alpha=\frac{l^2\Omega}{h}\frac{1}{1+\boldsymbol{B}^2/B_{\mathrm{eq}}^2}, \tag{3.13}$$

with the reference equipartition field strength

$$B_{\mathrm{eq}}=\left(4\pi\rho v^2\right)^{1/2}. \tag{3.14}$$

The local dynamo number can now be calculated

$$D\left(r\right)=R_\alpha R_\omega r\frac{\partial\Omega}{\partial r}\Omega\left(r\right)h^3\left(r\right), \tag{3.15}$$

including the disc flaring $h\left(r\right)$. In dimensionless form, and now that $\partial\Omega/\partial r$ is not constant, there is a much stronger shear within the inner regions of the disc, where the angular velocity gradient is large. Taking $h_0=0.5\,\mathrm{kpc}$, the dimensionless profile for the scale height lies within the range $0.4\leq h\left(r\right)\leq 1.1$, resulting in $0.064\leq h^3\left(r\right)\leq 1.33$, and so reducing the magnitude of the local dynamo number significantly within the inner regions, as in Table 3.3. This means that the dynamo is not dominated by the shear

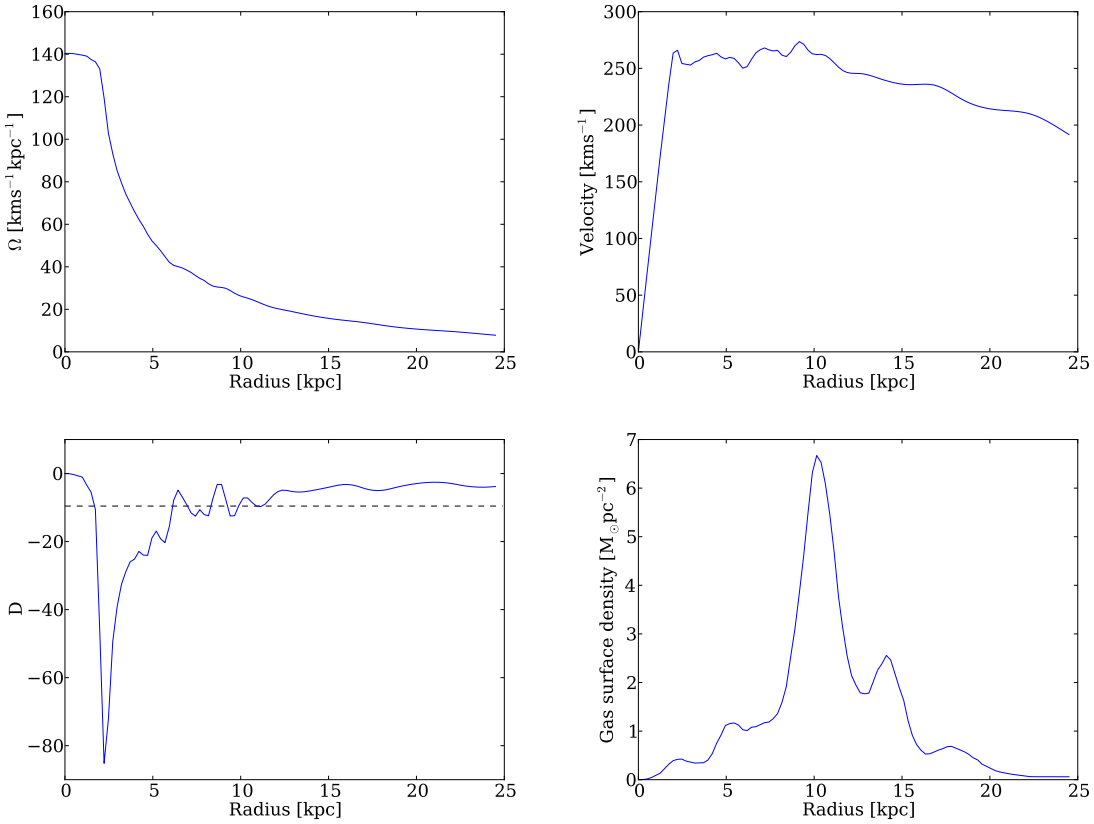

Figure 3.10: *Upper left panel*: Angular velocity as a function of radius, taken from Fig. 2 in Moss *et al.* (1998), a fit to the observations of Braun (1991). *Upper right panel*: Azimuthal velocity as a function of radius, derived from the angular velocity, using $U_\phi = r\Omega\,(\mathrm{r})$. *Lower left panel*: Local dynamo number, as calculated from Eq. (3.15), corresponding with the solid curve in Fig. 2 of Moss *et al.* (1998). *Lower right panel*: Gas surface density as a function of radius, converted from Fig. 1 of Moss *et al.* (1998), who derived the profile from the H I density observations of Cram *et al.* (1980), the CO density observations of Dame *et al.* (1993), and the H I scale height observations of Braun (1991).

Radius [kpc]	$D(r)$
3	-39
10	-7
18	-5

Table 3.3: Values of the local dynamo number calculated from Eq. (3.15).

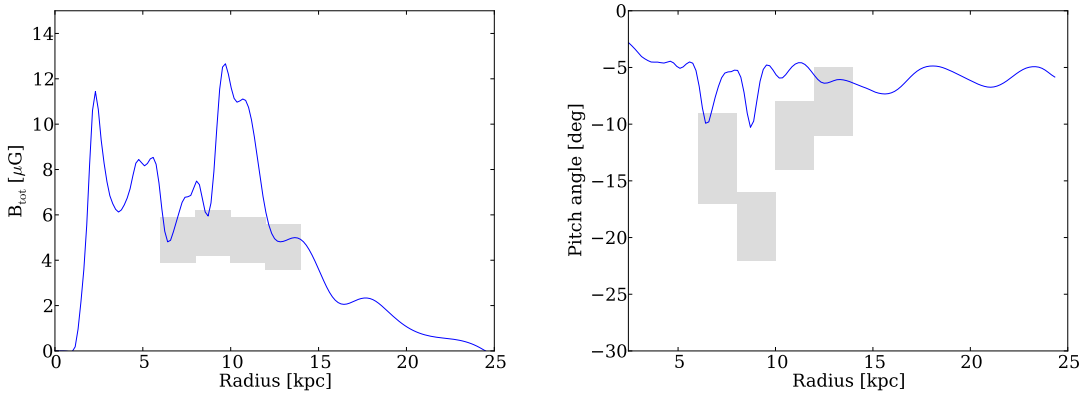

Figure 3.11: *Left panel*: Total steady state magnetic field strength obtained from the model of Moss *et al.* (1998) for M31 with no vertical outflow. *Right panel*: Local pitch angle calculated from the same model. Grey boxes denote observations from Fletcher *et al.* (2004).

within the inner few kpc.

The initial conditions used in the original work included magnetic field reversals in the disc. Here, we retain the initial conditions we used in Section 3.2, and note that this change in seed field does not have an effect on the radial profiles of field strength and pitch angle that we shall discuss. We use zero conditions at the inner boundary, i.e. $B_r(r=0) = B_\phi(r=0) = 0$.

Fig. 3.11 shows the results of this model for M31, using $R_\alpha = 0.771$ and $R_\omega = 19.284$ (which correspond to values of $\alpha_0 = 0.5\,\mathrm{km\,s^{-1}}$, $\Omega_0 = 25\,\mathrm{km\,s^{-1}\,kpc^{-1}}$ and $\eta_\mathrm{t} = 1.0 \times 10^{26}\mathrm{cm^2 s^{-1}}$ respectively). In contrast to the generic models from Sections 3.1 and 3.2, we now obtain a much more featured magnetic field profile, with magnitudes in the order of the observational data. As found by Moss *et al.* (1998), there is a peak in the magnetic field strength in the range $8 \leq r \leq 12\,\mathrm{kpc}$, which is observed in the disc of M31, which corresponds with the ring of high gas density in M31. The grey boxes in Fig. 3.11 show observations of the regular magnetic field and pitch angle with corresponding uncertainties from Fletcher *et al.* (2004). The boxes show a much less prominent peak in the magnetic field strength, so it is possible that there is some missing element of the

model.

This point becomes clearer when examining the magnetic pitch angles shown in Fig. 3.11 (right panel). The pitch angles are in very good agreement with the 2D model of Moss *et al.* (1998), demonstrating the ability of the no-z approximation to accurately model a thin disc. However, the model pitch angles are generally $5 - 10^{\circ}$ smaller than observed.

3.3.2 New gas density profile

Since 1998, new observations of the gas density profile of M31 have been made. It is important to see if any differences in the profiles change the results of this model.

We include the H I surface density profile from Chemin *et al.* (2009), and combine with the CO profile taken from Nieten *et al.* (2006). To combine the profiles, we convert the CO emission intensity profile from Fig 9. of Nieten *et al.* (2006), using $X_{\rm CO} = 1.9 \times 10^{20}$ mol cm^{-2} $\left(\text{K km s}^{-1}\right)^{-1}$, which can be written as $\Sigma_{\rm CO} = 3.04 I_{\rm CO}\, \text{M}_{\odot}\text{pc}^{-2} \left(\text{K km s}^{-1}\right)^{-1}$, converting the CO surface density into an atomic hydrogen density equivalent, so we can combine with the H I data. There are differences to the total gas surface density present in the data Moss *et al.* (1998) used (Fig. 3.10, lower right panel). The peak in the region $8 \leq r \leq 12\,\text{kpc}$ is wider in the observations of Chemin *et al.* (2009), and the maximum is closer to $r \simeq 12\,\text{kpc}$ than the $r \simeq 10\,\text{kpc}$ peak present in the previous observations. It is also a higher peak, about $3\text{M}_{\odot}\text{pc}^{-2}$ greater than the previous data. There is also more gas in the region $0 \leq r \leq 7\,\text{kpc}$ in the new observations.

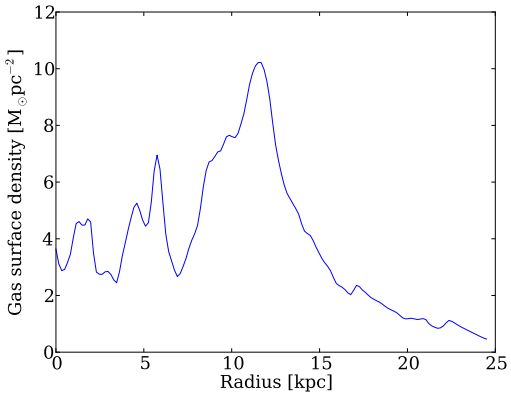

Figure 3.12: Un- smoothed gas surface density, a combination of CO and H I, taken from Nieten *et al.* (2006) and Chemin *et al.* (2009) respectively.

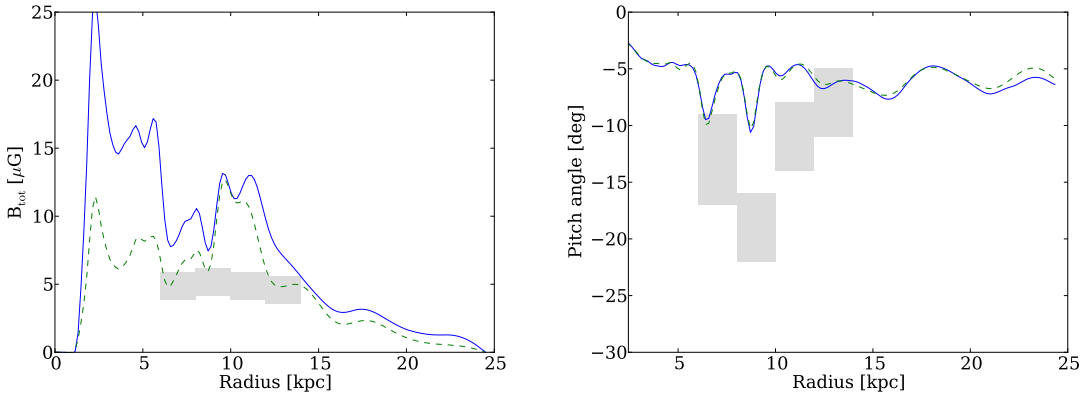

Figure 3.13: *Left panel*: Local magnetic field strength as calculated using the new combined density profile of H I of Chemin *et al.* (2009) and CO of Nieten *et al.* (2006) from Fig. 3.12. *Right panel*: Local pitch angle calculated from the model with the new density profile. Dashed lines denote the results using the gas density profile of Moss *et al.* (1998). Grey boxes denote observations with corresponding uncertainties from Fletcher *et al.* (2004).

We can deduce what effect this new profile will have on the dynamo. The density enters the model as part of the equipartition field strength, $B_{\rm eq}$, which in turn is part of the α- quenching nonlinearity. With a higher equipartition strength, we would expect to see the magnetic field reach higher values before it saturates, and as we now have a considerably higher density in the inner regions of the disc, we would expect that there will be significant magnetic field in this area.

Fig. 3.13 shows what is expected, with larger magnetic field strengths in the inner regions of the disc, a large contrast to the results in Fig. 3.11 (left panel). The pitch angle is not affected by the change of density profile.

3.3.3 New rotation curve

We use the recent rotation curve of Chemin *et al.* (2009) to gauge the sensitivity of the model to changes in $U_\phi\,(r)$. There are small differences in the local dynamo number to the curve using the original rotation curve in Fig. 3.14. We use a smoothed version of the rotation curve given in Chemin *et al.* (2009), and will be discussed in Chapter 4. This smoothed curve gives a much less featured local dynamo number, and a wider peak in the inner regions of the disc. More of the local dynamo number is smaller in magnitude than the estimated critical dynamo number of $D_{\rm cr} = -9.6$ of the model of Sur *et al.* (2007); however without the derivative coefficients used in that paper, the critical dynamo number would be $D_{\rm cr} = -1$, allowing the magnetic field to grow mostly

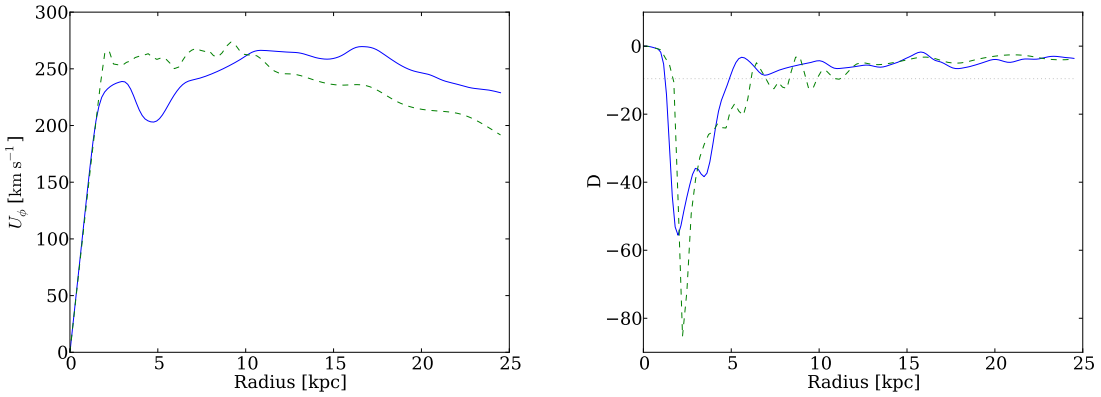

Figure 3.14: *Left panel*: Rotation curve from Chemin *et al.* (2009) (solid line). The dashed line shows the data from Braun (1991), which featured in the model in Section 3.3.1. *Right panel*: Local dynamo number, as calculated from equation (3.15). The dashed line shows the local dynamo number featured in Section 3.3.1.

throughout the disc.

With this taken into account, we might expect weaker magnetic field growth in the outer regions of the disc, and a slightly wider area of strong growth in the inner regions. The results are shown in Fig. 3.15.

The magnetic field strength is now stronger in the inner and outer regions of the disc. The peak previously observed in the magnetic field profile at $r = 10\,\mathrm{kpc}$ is now slightly broader, yet with the observations giving very little evidence for a peak in the magnetic field strength, this new result, even with a magnitude of roughly twice that of the observations, is a positive step forward. There is significant change in the shape of the pitch angle profile using the new rotation curve. There are now two distinctive troughs at $r = 6\,\mathrm{kpc}$ and $r = 16\,\mathrm{kpc}$.

3.3.4 The effect of an outflow on the magnetic field

First we improve the model of Moss *et al.* (1998) discussed in Section 3.3.1. In Section 3.1, we showed that non-circular flows can alter the pitch angle. Let us show how vertical outflows can change the pitch angles obtained for M31. We introduce an outflow which is constant with position and dimensionlessly equal to 1. This simple outflow will later be developed into a physically consistent model. We begin by applying this simple outflow to the α-quenching model of Section 3.3.1. We use $R_\alpha = 0.7714$ and $R_\omega = 19.284$, and now vary R_{U_z}, and show the results in Fig 3.16.

The effect of the outflow on the magnitude of the magnetic field is immediately appar-

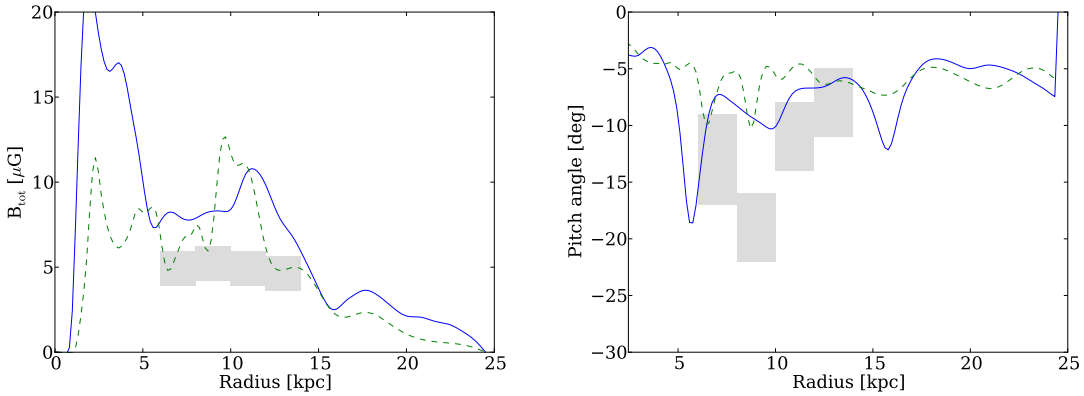

Figure 3.15: *Left panel*: Local magnetic field strength as calculated using the new rotation curve of Chemin *et al.* (2009). *Right panel*: Local pitch angle calculated using the new rotation curve. Dashed lines denote the results using the rotation curve of Braun (1991). Grey boxes denote observations with corresponding uncertainties from Fletcher *et al.* (2004).

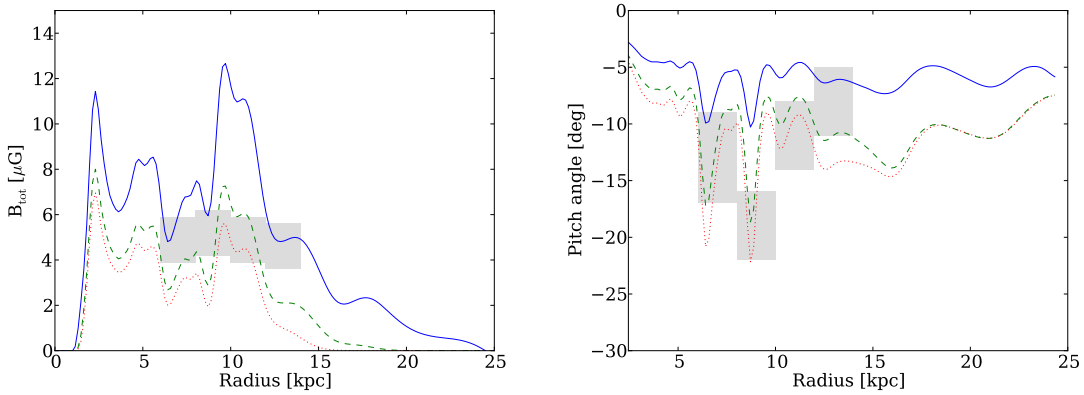

Figure 3.16: *Left panel*: Local total magnetic field strength as calculated using the α- quenching model of Moss *et al.* (1998). Values of R_{U_z} are 0.0, 1.0 and 1.5 (solid, dashed and dotted respectively). *Right panel*: Local pitch angle calculated from the model. Values of R_{U_z} are 0.0, 1.0 and 1.5 (solid, dashed and dotted respectively). Grey boxes denote observations (with error estimates) from Fletcher *et al.* (2004).

ent and significant. For $R_{U_z} = 0$ the original result of Fig. 3.11 is reproduced, and when the magnitude of the outflow is increased, the magnitude of the steady state magnetic field is decreased. As this is a constant outflow throughout the disc, the magnetic field is reduced by the same factor in all regions of the disc. We would expect this not to be the case should the outflow vary with position, with lower local values of outflow leading to lower reductions in the steady state field. We also would expect higher values of R_{U_z} to lead to the magnetic field decaying quicker than being amplified, therefore $\boldsymbol{B} \rightarrow 0$ (Shukurov *et al.*, 2006; Sur *et al.*, 2007).

Perhaps surprisingly, the pitch angle is also altered by the inclusion of the outflow. $R_{U_z} = 1.0$ increases the pitch angle by a factor of nearly 2; large enough to bring the model results into much better agreement with the observations. This is an important result.

The nature of the magnetic belt in M31: Summary

In this section we have demonstrated the ability of the no-z model to reproduce the results of the 2D model of Moss *et al.* (2000) with high accuracy, and demonstrated the sensitivity of the model to the introduction of different sets of observational data. Changes in the rotation curve can change the magnetic field profile and the magnetic pitch angle.

Changing the gas density affects the structure and magnitude of the magnetic field and has little or no effect on the pitch angle. Alterations in the rotation velocity lead to both changes in the magnetic field and the pitch angle.

Updating the density and rotation curves to more recent profiles does not significantly improve the comparison with the observed magnetic field, in particular the pitch angles. This would suggest that there is something missing from the model.

In Chapter 4 we will investigate the effects of outflows on the model, to attempt to improve the comparison with observational data.

———

Chapter 4

The Andromeda Galaxy

M31

NGC224

Image credit: NASA/JPL-Caltech/UCLA

4.1 Introduction

The Andromeda nebula (M31, NGC224) is the nearest spiral galaxy to the Milky Way galaxy. It lies at a distance of $780 \pm 40\,\mathrm{kpc}$ (Stanek & Garnavich, 1998), and is inclined at an angle of $74° \pm 1°$ (Chemin *et al.*, 2009) (where 0° would be face on). Even though its large inclination presents observers with some difficulty, its proximity means that it is one of the most observed and studied galaxies. The abundance of observational

information allows for detailed testing of models such as the one we have developed in Chapter 2. We use a physically motivated description of the α-effect, with magnetic helicity conservation in the disc alleviated by a galactic outflow. We will compare this with a standard α-quenching model. This is the most physically rich galactic dynamo model for a specific galaxy developed to date.

M31 is very well suited for our purposes since all of the important input parameters for our model, including their variation with galactic radius, are known from observations: the rotation curve (Sofue *et al.*, 1999; Chemin *et al.*, 2009), gas density (Nieten *et al.*, 2006; Chemin *et al.*, 2009) and scale height (Braun, 1991), and star formation rate (Tabatabaei & Berkhuijsen, 2010). In addition the magnetic field of M31 has been studied extensively using radio polarization observations since these became possible over 30 years ago. The properties of the regular magnetic field of M31 are better known than those of any other spiral galaxy as a result of a comprehensive series of radio observing programmes and careful modelling of the full set of radio data.

Early maps of the total radio emission from M31 such as the λ11cm survey of Berkhuijsen & Wielebinski (1974), which trace the combined distribution of cosmic ray electrons and total magnetic field, discovered that the emission is concentrated in a bright ring centered at a radius of $r \simeq 10$kpc that is several kpc wide. Subsequent radio polarization observations (Beck *et al.*, 1978; Beck, 1982; Beck *et al.*, 1989), among the earliest resolved polarization studies of nearby spiral galaxies, showed that this ring hosts a strong regular field (with the regular and random field components of equal strength in the ring) that is basically axisymmetric and predominantly azimuthal i.e. that it has a small pitch angle which does not vary much with azimuth. These basic properties of the regular field were confirmed by Faraday rotation measurements (Berkhuijsen *et al.*, 2003). Fletcher *et al.* (2004) fitted a parameterized model of regular field to all of the available polarization maps, simultaneously taking into account depolarization, which returned the field strength and pitch angle as a function of radius and azimuth. Their results showed that the regular field can be described by a single axisymmetric azimuthal mode (i.e. $m = 0$ in azimuth) in the radial range $8 - 14$kpc, and a predominantly axisymmetric mode, perturbed by a weaker doubly periodic (i.e. $m = 2$) mode, between 6 and 8kpc. The regular field strength only mildly peaks at $r = 10$kpc and the magnitude of the pitch angles tend to decrease with increasing radius.

This very simple regular magnetic field structure is an ideal test for our new dynamo model as its rotational symmetry means that we need only to retain r and t as our independent variables. Of course in order to study more detailed properties of the magnetic field of M31 ϕ and z dependence will need to be restored. Thus our model

will be strongly constrained by observable inputs and will generate output parameters, the magnetic pitch angle and strength profiles, that can be compared directly to the observationally determined magnetic field.

Earlier attempts to construct dynamo models for specific galaxies, including M31, tended to use only the rotation curve as a unique characteristic of the galaxy (Ruzmaikin *et al.*, 1985; Baryshnikova *et al.*, 1987; Krasheninnikova *et al.*, 1989). In the case of M31 this led to the prediction that its regular magnetic field would be concentrated in a ring at a radius of $r \simeq 10$kpc (Ruzmaikin & Shukurov, 1981); this prediction was then confirmed by observations (Beck, 1982) and is an early illustration of both the success of the mean field galactic dynamo theory and the utility of M31 as an object with which to compare theory to observation! Although these models could reproduce some of the observed magnetic features, they all tended to struggle to reproduce the observed magnetic pitch angles, which have long been recognized to be a very sensitive diagnostic of the regular field (Ruzmaikin *et al.*, 1988). The model of Moss *et al.* (1998) for M31, discussed in the previous Chapter, used the observed rotation curve, gas density and scale height (taking into account the flared gaseous disc), but while the concentration of magnetic field in a ring centered at 10 kpc radius was reproduced, the magnitude of the pitch angles of the field were everywhere much smaller than observed: in other words the modelled field was much more azimuthal than the observed field. In this Chapter we show that adding an observationally constrained outflow alleviates this problem in M31, producing a very close correspondence between the modelled and observed pitch angles.

Application of the outflow with recent observations

In Sections 3.3.2 and 3.3.3, we introduced new observations to see how these would affect the results obtained by Moss *et al.* (1998). We first show the results of the calculations using the combined gas density profile of Chemin *et al.* (2009) and Nieten *et al.* (2006) in the model of Section 3.3.1, with our constant outflow, and show the results in Fig. 4.2, where, for the first time in this study we have taken the total magnetic field obtained from the simulation and split it into its radial and azimuthal components, giving a direct view of how the magnetic field is structured in terms of the coordinate system.

Again, with $R_{U_z} = 0$, the original results from Fig. 3.13 are obtained, and the application of the constant outflow has a significant effect on the magnitude of the magnetic field strength, and the magnitude of the magnetic pitch angle. Setting $R_{U_z} = 1.0$ reduces the magnitude of the steady state azimuthal magnetic field profile again by a factor of nearly 2, enough to give a good agreement with the observational values. This increase in

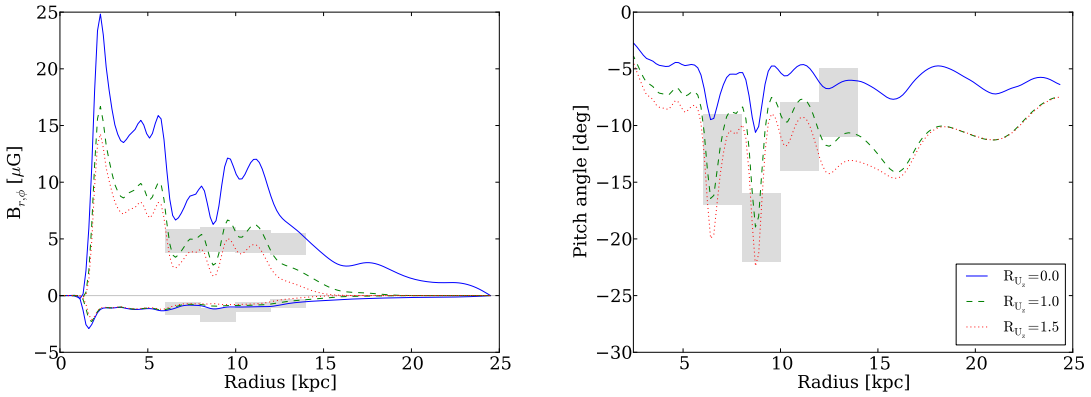

Figure 4.2: *Left panel*: Strength of the local magnetic field components (positive lines are azimuthal, negative lines are radial) as calculated using the α-quenching model of Moss *et al.* (1998), with the combined gas density profile of Chemin *et al.* (2009) and Nieten *et al.* (2006) (see Fig. 3.12). Values of R_{U_z} are 0.0, 1.0 and 1.5 (solid, dashed and dotted respectively). *Right panel*: Local pitch angle calculated from the components in the left panel. Values of R_{U_z} are 0.0, 1.0 and 1.5 (solid, dashed and dotted respectively). Grey boxes denote observations from Fletcher *et al.* (2004).

R_{U_z} approximately halves the strength of the azimuthal magnetic field, whereas there is a considerably smaller reduction in the magnitude of the radial magnetic field. This has a profound effect on the pitch angle, which becomes less azimuthal, and has a magnitude closer to the observational data for $R_{U_z} = 1.0$, as compared to the zero outflow case, $R_{U_z} = 0$. The dip in the observed pitch angle data at $8 \leq r \leq 10\,\mathrm{kpc}$ is now approximately reproduced and the results in the surrounding regions are broadly comparable to those in Fig 4.2.

Next, we apply the same outflow using the new rotation curve of Chemin *et al.* (2009) introduced in Section 3.3.3, whilst keeping the gas density profile the same. The results are shown in Fig. 4.3.

There are some instantly noticeable differences in the fit to the observational data with increased R_{U_z}, than with the old rotation curve in Fig. 4.2. The curve contains fewer features, and does not vary as heavily as previously. For $R_U = 1.0$, the magnitude of the total magnetic field is slightly closer than that with the old rotation curve of Braun (1991) (see Fig. 3.10). The magnetic pitch angle is also closely reproduced, with the dip in the $8 \leq r \leq 10\,\mathrm{kpc}$ region being retained whilst having a good fit in the other regions of the disc; however again the curve is less featured. Results with fewer features may or may not be a good thing; it is possible that in applying the smoothings we have to the observational data that some results may be overlooked.

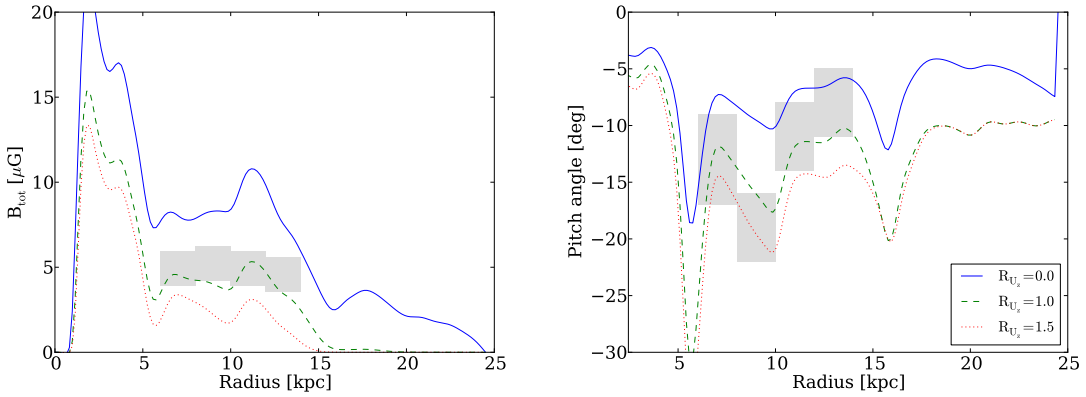

Figure 4.3: *Left panel*: Local total magnetic field strength as calculated using the α-quenching model of Moss *et al.* (1998), with the recent H I rotation curve of Chemin *et al.* (2009) (see Fig. 3.14). Values of $R_{\rm Uz}$ are 0.0, 1.0 and 1.5 (solid, dashed and dotted respectively). *Right panel*: Local pitch angle calculated from the left panel. Values of $R_{\rm Uz}$ are 0.0, 1.0 and 1.5 (solid, dashed and dotted respectively). Grey boxes denote observations (with error estimates) from Fletcher *et al.* (2004).

In summary, a non-zero vertical outflow helps to bring the results of the no-z dynamo model for M31 into closer agreement with the observed radial profile of the regular magnetic field strength and pitch angle.

Now that the broad effects of vertical outflows on the magnetic field derived for M31 has been tested, and it has been discovered that an outflow can improve the match between modelled and observed pitch angles, we will include our physical model for a galactic outflow developed in Section 2.3.1, along with the most up to date observational data we have, in order to develop a new dynamo model for M31.

4.2 Observational parameters for M31

4.2.1 Gaseous disc scale height

We adopt the H I disc scale height profile used by Moss *et al.* (1998), which they derived from the H I observations of Braun (1991), and is shown in Fig. 4.4.

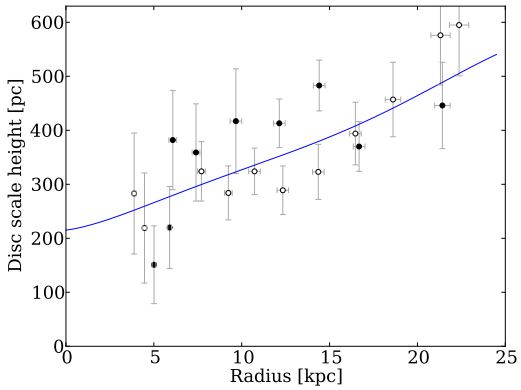

Figure 4.4: H I disc scale height of M31 (solid line), derived from a smoothing of the model given by Eq. (3.12). The points represent observations from Braun (1991) of the northern and southern spiral arms (open and filled circles respectively).

A slight change in gradient at $r = 16\,\mathrm{kpc}$ represents an increase in the flaring of the gaseous disk in the outer regions. For our model we have taken a cubic spline interpolation of Eq. (3.12), and smoothed it to give the H I gas scale height. This gives the closest smooth fit to the model. We also require a CO scale height, which is approximated from the H I scale height via $h_{\mathrm{CO}} \approx 0.5 h_{\mathrm{HI}}$, a rough estimate based on observed values for the Milky Way (Ferrière, 2001).

4.2.2 Gas densities

To derive the total gas density we use the combination of the CO gas surface density, converted via Σ_{CO}=3.04$I_{\mathrm{CO}}\mathrm{M}_{\odot}\ \mathrm{pc}^{-2}\left(\mathrm{K\ km\,s^{-1}}\right)^{-1}$, where I_{CO} is the intensity of CO emission measured in K $\mathrm{km\,s^{-1}}$, from Nieten *et al.* (2006), and recent observations by Chemin *et al.* (2009) of the H I surface density, Σ_{HI}, which we introduced in Section 3.3.1. We perform a similar smoothing to the one used for the disc scale height. This combination gives the gas surface density shown in Fig. 4.5. We obtained the stellar surface density, Σ_* (dashed line in Fig. 4.5) from a chemical evolution model based on gas density given in Marcon-Uchida *et al.* (2010).

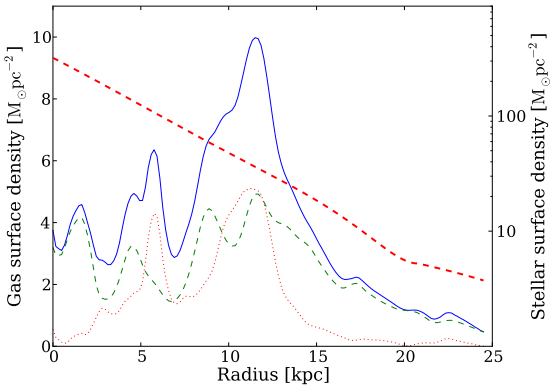

Figure 4.5: Gas surface density (solid line) calculated as a combination of the H I observations from Chemin *et al.* (2009) (green dashed line), and the converted CO intensity profile from Nieten *et al.* (2006) (red dotted line). The stellar surface density is shown by the red dashed line (Marcon-Uchida *et al.*, 2010). The total gas surface density is a smoothed version of the curve in Fig 3.12.

An interesting point arising from the new gas density data within the inner 8 kpc of the galaxy in the presence of multiple peaks. In previous observations (H I observations of (Dame *et al.*, 1993)), there is a strong peak at around 10-12kpc, and in the rest of the disk, the density is much lower. This is not the case in the new data. There are two very clear peaks in gas density only slightly weaker than that of the main ring at 10 kpc, and it is suggested by Chemin *et al.* (2009) that these are consistent with ring-like structures in the inner regions of the disc.

The total gas surface density, $\Sigma_{\rm g} = \Sigma_{\rm HI} + \Sigma_{\rm CO}$ can be used to calculate the equipartition field strength using Eq. (3.14), where $\rho_{\rm g}$ can calculated via

$$\rho_{\rm g} = \frac{\Sigma_{\rm HI}}{2h_{\rm HI}} + \frac{\Sigma_{\rm CO}}{2h_{\rm CO}}, \tag{4.1}$$

and we use $v = 10{\rm kms}^{-1}$ as an estimate for the turbulent velocity (Ferrière, 2001). We define ρ_0 in terms of a single hydrogen atom per unit volume, $\rho_0 = 1.67 \times 10^{-24}{\rm g\,cm}^{-3}$. We obtain a value of B_0=4.61μG at $r = 12\,$kpc, and use this as the reference equipartition field strength.

4.2.3 Rotation curve

The rotation curve derived from observations of M31 has undergone several changes in recent decades as observational methods and instrumentation have advanced. We discuss the most significant of these differences in this section.

In the dynamo model used by Moss *et al.* (1998), discussed in Section 3.3.1, the rotation curve used was taken from observations of H I gas by Braun (1991). This rotation curve, shown in Fig. 4.6 (left panel) has a systematic negative gradient in the slope of $U_\phi(r)$ beyond the inner regions of the disk, out to a galactocentric radius of around 25 kpc.

More recent observations of H I by Sofue *et al.* (1999) and Chemin *et al.* (2009) show a flatter profile in U_ϕ, as shown in Fig. 4.6 (upper right and middle left panels) (The velocity measurements are divided into the two spiral arms of M31; approaching, and receding; as Chemin *et al.* (2009), whereas the study of Sofue *et al.* (1999) did not differentiate between the arms).

The uncertainties in the observations, which are of the order $10\,\mathrm{km\,s^{-1}}$ (Chemin *et al.*, 2009), mean that small scale features in Fig. 4.6 may not be real.

The curve obtained in Chemin *et al.* (2009) is globally in reasonably good agreement with the curve from Sofue *et al.* (1999), as shown in Fig. 4.6. We see that the curve of Sofue *et al.* (1999) is slightly less featured, and does not extend as far out into the disc as in the observations of Chemin *et al.* (2009). Another notable difference is the behaviour of the curve in the inner 3 kpc. As discussed by Chemin *et al.* (2009), the inner disc of M31 may be warped, so obtaining accurate rotation velocities from the observations is extremely difficult. As the observational data on the magnetic field is poor in this region, we have a small amount of flexibility in how we handle the information we have.

The first thing we do with the rotation curve is to reduce the radial range in which we are working. Our main concern with respect to M31 is the region of the disk in the range 6–14 kpc. This is where the surface gas density peaks, and is also the region where we have reliable information about the regular magnetic field. Also, of the observational data we are using, only the rotation curve extends to such large radii, with the other quantities tending to extend to between 20 and 25 kpc: we take $R_0 = 25\,\mathrm{kpc}$ as our maximum radius. Hence we reduce the working range of the rotation curve to 25 kpc, as shown in Fig. 4.6 (middle right panel). Contrary to the radial inflow based model of Moss *et al.* (2000), we no longer use an inner boundary. We allow the disc to extend inwards to $r = 0$, but this must be handled carefully numerically.

We have chosen to use flat boundary conditions at the central point, which renders

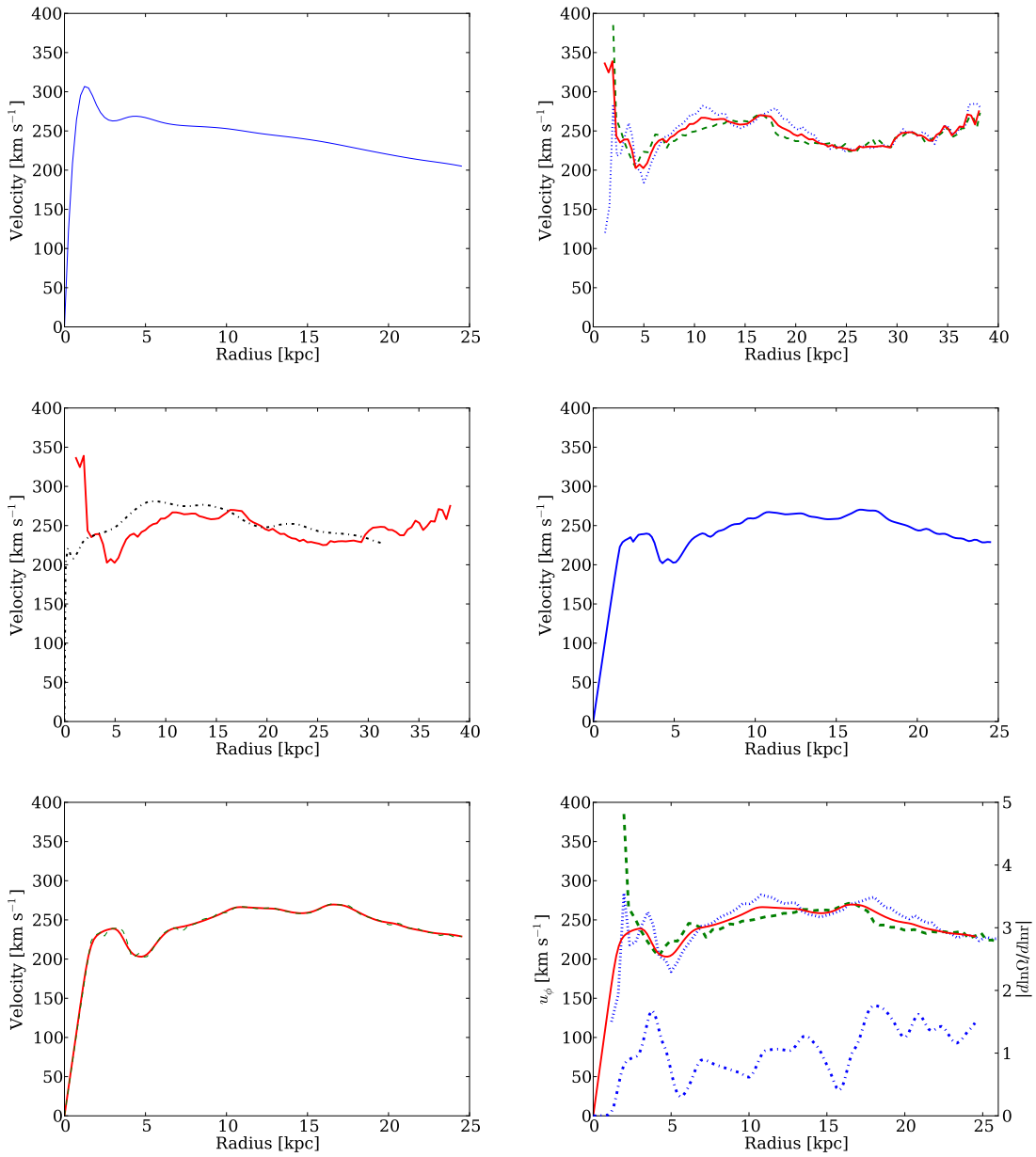

Figure 4.6: *Upper left panel*: The rotation curve of M31 taken from Braun (1991) (see Fig. 3.10). *Upper right panel*: The averaged rotation velocity of M31 as given by Chemin *et al.* (2009). The approaching spiral arm (dotted line) and the receding spiral arm (dashed line) are averaged. Note the differences in radial axes; the data in the upper right and middle left panels extends to 40 kpc. *Middle left panel*: Average rotation velocity of Chemin *et al.* (2009) (solid line), and the rotation curve of Sofue *et al.* (1999) (dashdot line). *Middle right panel*: Rotation curve using solid body rotation within 2 kpc, either rotation curve for 2-3 kpc and that of Chemin *et al.* (2009) outside 3 kpc. *Lower left panel*: Our smoothed rotation curve (solid line) and the rotation curve from the middle right panel (dashed line). *Lower right panel*: Our smoothed rotation curve (solid line) and those of both spiral arms as in the upper right panel. The dashdot line denotes the local shear (right axis).

the gradient equal to zero at $r = 0$. We believe this to be the best way of retaining realism in the results whilst allowing for as natural an evolution of the magnetic field as possible. The flattening of the curve at $r = 0$ discourages the increase towards infinities where r is extremely small.

In the inner regions of the disk ($r < 3\,\mathrm{kpc}$), there is a convenient intersection of the rotation curves of Sofue *et al.* (1999) and Chemin *et al.* (2009) around $r = 3\,\mathrm{kpc}$, so it can be assumed that the observations at that radius are reliable. This is a good point in the curve in which to fix an effective inner boundary, beyond which we will use the rotation curve of Chemin *et al.* (2009).

It would appear that the data of Sofue *et al.* (1999) could be used within 3 kpc, however this causes problems. In the very inner regions, where the curve drops away very steeply, $\partial\Omega/\partial r$ becomes extremely large, and hence also the dynamo number.

Given the discrepancies between the various rotation curves at small radii, and the absence of information about the regular magnetic field in the centre of M31, we shall assume that the rotation of the disc for $r < 2\,\mathrm{kpc}$ is that of a solid body. This simply means taking the velocity from this point and decreasing it linearly to zero with decreasing r, as shown in Fig. 4.6 (middle right panel).

Finally we apply a cubic spline interpolation too make a modest smoothing, and obtain a new curve, which retains the main features of the curve of Chemin *et al.* (2009) whilst removing a lot of the smaller scale variations that we do not consider to be reliable components of the large-scale rotation of the galaxy. The result is shown in Fig. 4.6 (lower panels; red solid line).

We now have a smooth profile describing the rotational velocity of the galaxy, which retains the main features of the observations, and combines observations in the inner regions of the galaxy with those from previous studies. Using the observations of the atomic hydrogen disc scale height, $h(r)$, and rotational velocity $U_\phi = r\Omega(r)$ we are able to derive the local dynamo number from Eq. (2.19), shown by the solid line in Fig. 4.7, as a direct comparison with the method and result found by Moss *et al.* (1998).

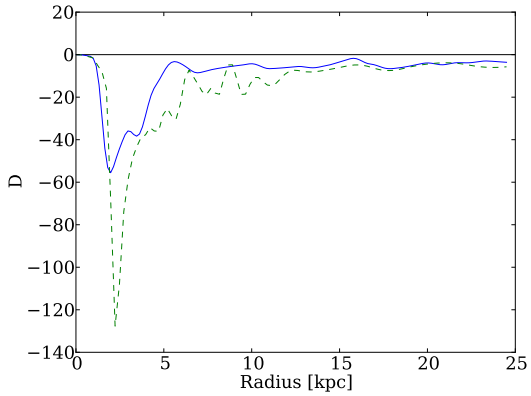

Figure 4.7: The local dynamo number given by Eq. (2.19) (solid line), and the local dynamo number used by Moss *et al.* (1998) (dashed line).

There is a clear difference in the magnitude of the local dynamo number in the inner regions of the disc. The minor peaks, arising from small variations in the rotation curve impact on the evolution of the dynamo considerably. Where there is even a small increase in the magnitude of the dynamo number in relation to the surrounding areas, the magnetic field will be allowed to grow to a greater extent.

4.2.4 Star formation rate

Tabatabaei & Berkhuijsen (2010) infer star formation rates from Hα observations, but note that for $r < 6\,\mathrm{kpc}$, there are few ionising stars, so Hα must be heated by something other than star formation. Hence the star formation rate is not reliable for $r < 6\,\mathrm{kpc}$ if it is derived from observations of Hα. The upper panel of Fig. 17 from Tabatabaei & Berkhuijsen (2010) demonstrates a modest rate of star formation in the region $6 \leq r \leq 17\,\mathrm{kpc}$.

These recent observations of the star formation rate in M31 have demonstrated the lack of connection between the gas density in the disc of M31 and the star formation rate (this is a result not confined solely to M31, and can be shown for a number of other galaxies (Kennicutt, 1989)). It was shown that the star formation does not follow a standard power law relation with the gas density. Another consequence of these findings is that the gas density in the disc falls below estimates of threshold values (Kennicutt, 1989; Marcon-Uchida *et al.*, 2010) considered sufficient to allow star formation. Since the connection between the two quantities is unclear, Tabatabaei *et al.* (2008) noted that the

values for star formation rate cannot be obtained using the standard Kennicutt- Schmidt law. Further investigation beyond the scope of this study is required to discover the mechanism by which the properties of the galaxy contribute to the star formation. It is for these reasons that we developed the outflow model of Section 2.3.1 from the star formation rate rather than the gas density profiles.

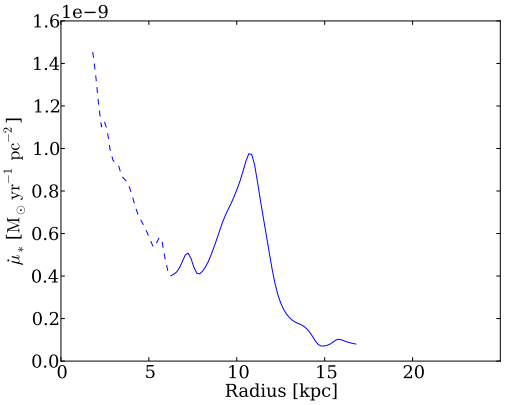

Figure 4.8: Local star formation rate density inferred from H_α observations of Tabatabaei & Berkhuijsen (2010). Note the dashed line within 6 kpc is derived from the H_α emission which is assumed to originate in mechanisms other than star formation.

4.2.5 Outflow model

Following the model for a galactic outflow developed in Section 2.3.1, we can proceed to derive $U_z(r)$ for M31. From the star formation rate surface density, $\dot{\mu}_*(r)$, of Section 4.2.4, and the CO scale height of Section 4.2.1 we can derive the wind velocity given by Eqn. 2.36. This wind velocity (Table 4.1) can be translated into a mass-weighted outflow from the disc of order $0.4\,\mathrm{km\,s^{-1}}$, using Eqn. 2.38; shown in Fig. 4.9 (left panel). The radial velocity profile, U_r is calculated using the model described in Section 2.3.3, and is shown in teh right panel of Fig. 4.9; however we do not use it in the dynamo calculations.

Beyond the region of observed star formation, we cannot simply assume that an outflow does not exist. As seen in Fig. 4.9, there is no rapid truncation in outflow velocity towards the extremities of the observed star forming region $6 < r < 17\,\mathrm{kpc}$. It is very possible that there is some star formation occurring in the other regions of the disc, but this is undetected. As a result we make the choice to mimic the general properties of the molecular gas, from which the stars form. Hence we reduce the outflow value to

Physical Quantity	**Mean Value**
Hot phase temp.	1.1×10^6K
Isothermal sound speed	$121\,\mathrm{km\,s^{-1}}$
Wind velocity	$191\,\mathrm{km\,s^{-1}}$
Mass weighted outflow velocity	$0.38\,\mathrm{km\,s^{-1}}$

Table 4.1: Mean values of the physical quantities described in the development of the wind model, derived from the observations of star formation rate, and gaseous disc scale height, through Eqs. (2.35)- (2.38).

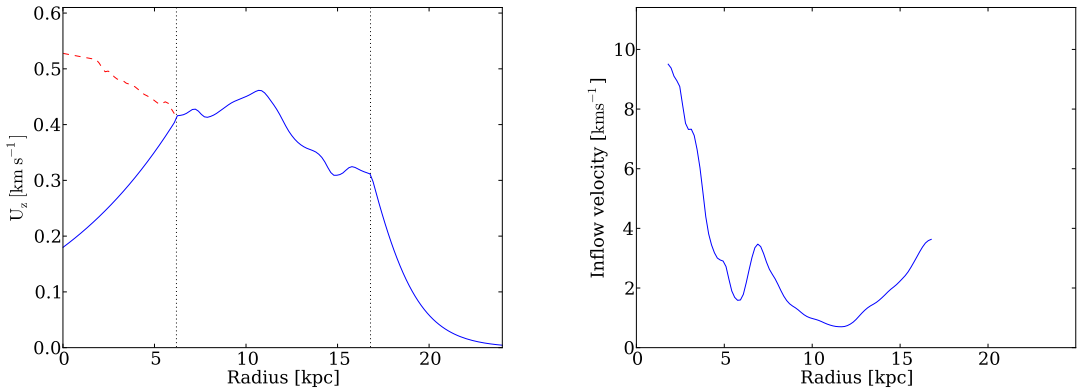

Figure 4.9: *Left panel*: Mass weighted vertical velocity profile as calculated using the wind model described by Eq. (2.38), for the optimum value of $R_{U_z} = 1.5$. The red dashed line within 6 kpc denotes the possible outflow profile if the Hα observations of Tabatabaei & Berkhuijsen (2010) are taken to be representative of star formation. Outside the region of observed star formation ($r > 17\,\mathrm{kpc}$), we reduce the magnitude of the outflow exponentially. *Right panel*: Radial inflow velocity profile as calculated using the wind model described by Eq. (2.47), based on the red dashed line in the left panel and the solid line beyond $r = 6\,\mathrm{kpc}$ to the end of the observed star forming region at $r = 17\,\mathrm{kpc}$. The inflow velocity profile was not used in the dynamo calculations.

a little under half that of the active region in the region $0 < r < 6\,\mathrm{kpc}$, and reduce exponentially in the region $17 < r < 24.5\,\mathrm{kpc}$.

4.3 Results

4.3.1 Galactic parameters

For both the α-quenching and dynamical α models we adopt the following parameters for non-dimensionalisation, characteristic of the observed profiles. We take $h_0 = 0.5\,\mathrm{kpc}$, $\Omega_0 = 25\,\mathrm{km\,s^{-1}\,kpc^{-1}}$, and $\alpha_0 = 0.5\,\mathrm{km\,s^{-1}}$. We take $\eta_\mathrm{t} = 1.0 \times 10^{26}\mathrm{cm^2 s^{-1}}$, $l_0 = 0.1\,\mathrm{kpc}$, and use $R_0 = 24.5\,\mathrm{kpc}$ to be the disc radius in which our observations lie. These parameters are used to derive the dimensionless parameters $R_\omega = 19$, and $R_\alpha = 0.8$. We consider values of R_{U_z} in the range $0 < R_{U_z} < 2.5$ which corresponds to values of $0.0 < U_0 < 1.62\,\mathrm{km\,s^{-1}}$, in order to calibrate the mass weighted outflow velocity.

4.3.2 Comparison with observations

We compare our results with the radial profiles of regular magnetic field strength and pitch angle from Fletcher *et al.* (2004). As well as comparing the dynamo model output with the observations directly, we average the model over 2 kpc rings, similar to the way the observations are treated, and uncertainties can be deduced from the mean and standard deviation. This gives the opportunity to compare the outputs of the model, in particular the magnetic field strength and pitch angles directly with the observational data.

4.3.3 Dynamos with α-quenching

We present the results for the α-quenching model in Fig. 4.10. We find a higher than observed magnitude of the regular magnetic field for low R_{U_z} and for high R_{U_z} a weaker field.

The optimum value is $R_{U_z} = 1.5$, which allows the field profile to rest comfortably within the observational ranges. Fig. 4.10 (panel b) shows the radial and azimuthal magnetic field profiles, as well as averages over 2 kpc sections for both quantities in the region $6 < r < 14\,\mathrm{kpc}$, where the observations of the regular magnetic field of Fletcher *et al.* (2004) lie. There is very good agreement in both the radial and azimuthal components of the magnetic field, with larger values of the magnetic field towards the inner regions of the disc, and lower values beyond $r = 14\,\mathrm{kpc}$. This good fit with the observations is reflected in the r.m.s. magnetic field strength, which has been averaged

in 2 kpc rings throughout the disc. this opens the opportunity for future observations to be tested against the model outputs in the regions not covered in Fletcher *et al.* (2004).

The pitch angle of the magnetic field for the α-quenching model is shown in Fig. 4.11 (panel c) and is in good agreement with the observations for $R_{U_z} = 1.5$. We find that for equal values of R_{U_z}, the outputs for the α- quenching and dynamical α models are in excellent agreement. The pitch angle of the magnetic field for the dynamical α model shown in Fig. 4.11 (panel c) shows a good agreement with the observations. We find that for the optimum value of $R_{U_z} = 1.5$, the pitch angle closely fits the observations of Fletcher *et al.* (2004) (see the lower panel for the averaging over 2 kpc rings throughout the disc), with the exception of the dip in the observed pitch angles in the region $8 < r < 10$ kpc. There is a drop in the model output, but it is not of the magnitude of the observations. It is possible that this may be a result of the smoothing we performed with the observational data used in the simulation. The agreement between the two α nonlinearities is very encouraging; from this we can suggest that both models are suitable representations of each other, whilst taking into account different aspects of the dynamo.

4.3.4 Dynamos with a dynamical α

We again use the parameters and observations outlined above, and allow the simulation to continue until a steady state in the magnetic field strength is achieved. We find that similarly to the dynamical α model of Sur *et al.* (2007), the magnetic field saturates much lower than the equipartition magnetic field strength. As a result we multiply the dimensionless output $B(r)$ by a factor of $5.5B_0$ to normalise to the observations of Fletcher *et al.* (2004). This factor of 5.5 is simply a chosen number, but could be explained in refernce to what was discussed earlier about various simplifications in the dynamo having a detrimental effect on the outcome of a simulation. The inclusion of the Vishniac-Cho flux at this point may allow the magnetic field to grow to a larger magnitude.

Figs. 4.11 (panel a) and 4.10 (panel a) show a strong similarity between the magnetic field profiles of the dynamical α and α- quenching models for the optimum value of $R_{U_z} = 1.5$. For lower values, the magnetic field strength is weaker, and at higher values, the magnetic field is also weaker.

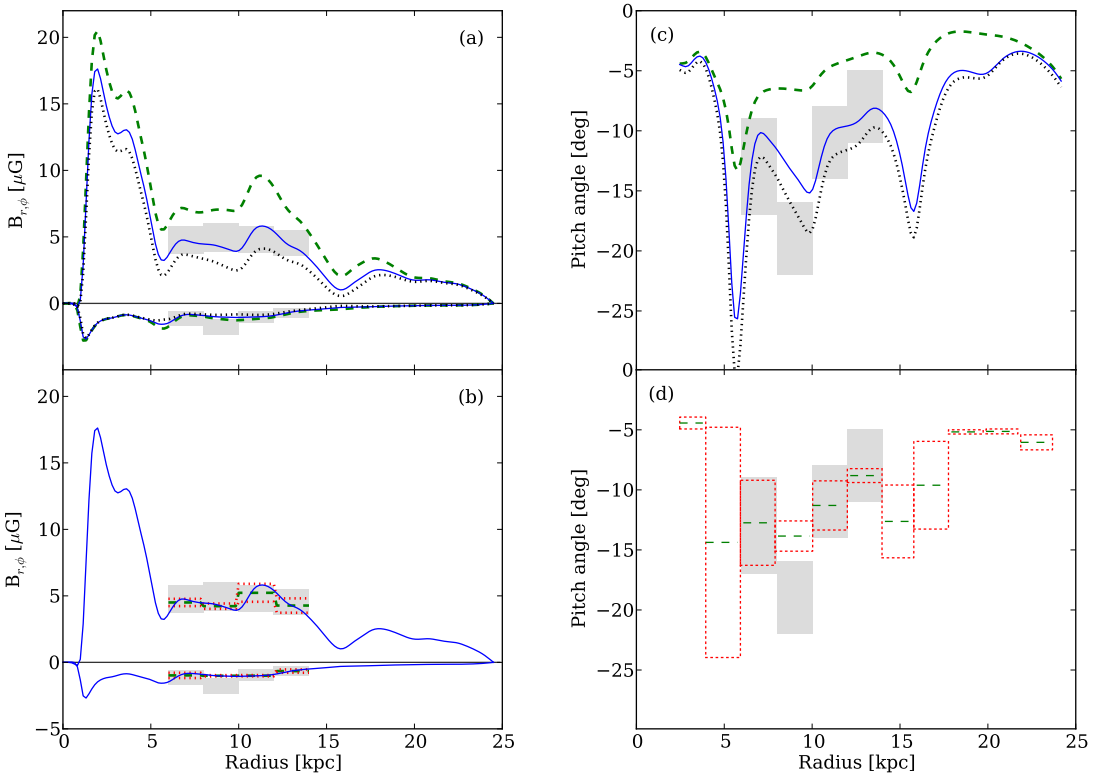

Figure 4.10: (a) Azimuthal (positive lines) and radial (negative lines) magnetic field components, for the α-quenching model, for $R_{U_z} = 0.0$, 1.5 and 2.5 (dashed, solid and dotted lines respectively). (b) Azimuthal and radial magnetic field profiles (positive and negative lines respectively) from the α-quenching model using $R_{U_z} = 1.5$. The dashed line represents averaging over regions of width 2 kpc within the range $6 < r < 14$ kpc, with the dotted line being a single standard deviation from the mean. (c) Pitch angles for the α-quenching model. Solid lines show the optimum value of $R_{U_z} = 1.5$. Dashed and dotted lines denote the results for $R_{U_z} = 0.0$, and 2.5 respectively. (d) Pitch angle obtained using $R_{U_z} = 1.5$, averaged over 2 kpc sections throughout the disc, with the dotted boxes denoting a single standard deviation either side of the mean, to correspond with the observations. The grey boxes in all panels denote observational values from Fletcher *et al.* (2004).

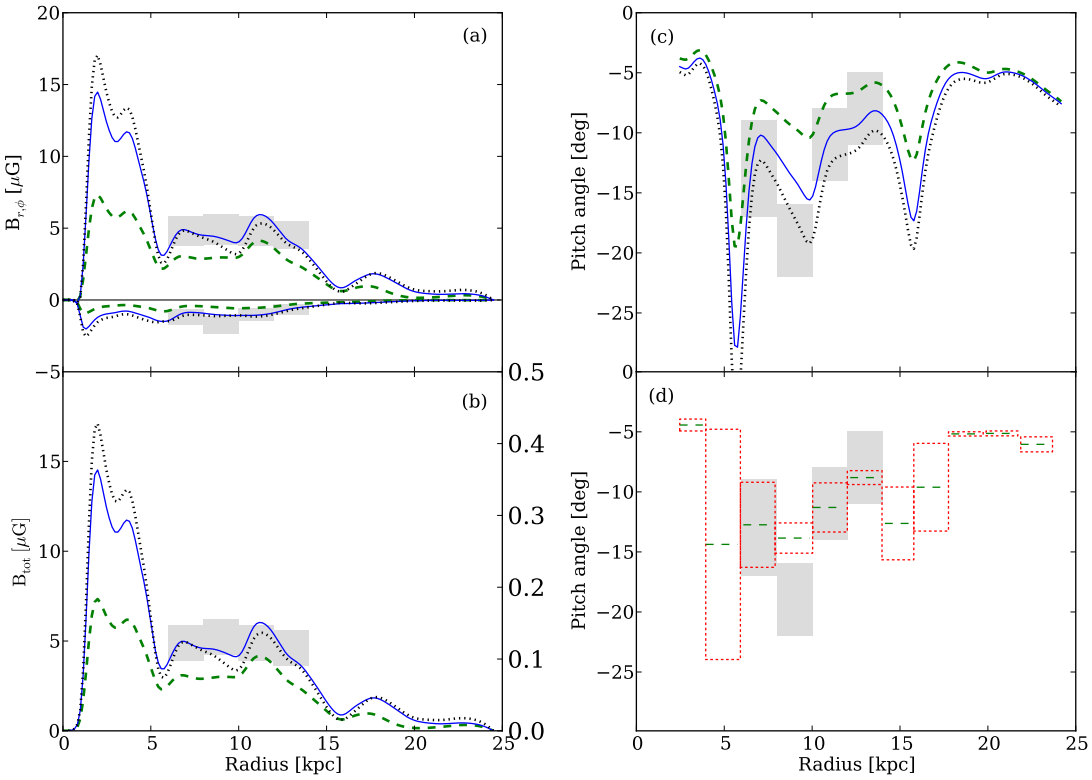

Figure 4.11: (a) Azimuthal (positive lines) and radial (negative lines) normalised magnetic field components for the dynamical α model, for $R_{U_z} = 0.3$, 1.5 and 2.5 (dashed, solid and dotted lines respectively). (b) Total values of the magnetic field strength, for the dynamical α model, for $R_{U_z} = 0.3$, 1.5 and 2.5 (dashed, solid and dotted lines respectively). (c) Pitch angles for the dynamical α model. Solid lines show the optimum value of $R_{U_z} = 1.5$. The dotted line denotes the result for $R_{U_z} = 2.5$. The dashed line shows the pitch angle using $R_{U_z} = 0.3$. (d) Pitch angle obtained from the dynamical α model using $R_{U_z} = 1.5$, averaged over 2 kpc sections throughout the disc, with the dotted boxes denoting a single standard deviation either side of the mean, to correspond with the observations. The grey boxes in all panels denote observational values from Fletcher *et al.* (2004).

4.3.5 Time evolution of the magnetic field

We calculate the linear growth rate of the total magnetic field,

$$\Gamma = \frac{d\ln|\boldsymbol{B}|}{dt}. \tag{4.2}$$

There is a similarity in the evolution of the magnetic field profiles for the α-quenching and dynamical α models as a function of time, demonstrated in Fig. 4.12.

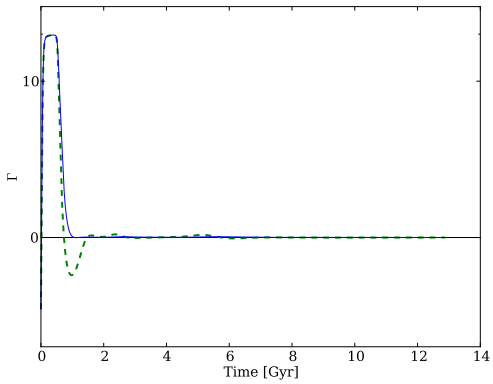

Figure 4.12: Linear growth rates calculated using Eq. (4.2) for the α-quenching and dynamical α models (solid and dashed lines respectively).

In both models, we observe a relatively quick initial growth phase. During this period in both models, the shear dominates the growth, and the magnetic field grows exclusively in the region of the disc where the angular velocity is high, i.e. $0 < r \lesssim 6\,\mathrm{kpc}$. The nonlinearity beings to dominate once the magnetic field grows to magnitudes comparable with that of the equipartition magnetic field strength, and in both models we see a reduction in the growth rate and an eventual slight decay in the field, this magnitude of decay being greater in the dynamical α model. Beyond this, the growth rate of the magnetic field in the α-quenching model remains positive, with some pseudo-oscillatory behaviour until the magnetic field saturates and the growth rate becomes zero at around 12Gyr. In the dynamical model, the same saturation is observed at a comparative point in time, however the growth rate oscillates about the origin until this time. This oscillatory behaviour could be explained in physical terms by how the magnetic field is transforming between azimuthal and radial components. The strength of the magnetic field increases (positive growth rate) as the Ω-effect winds up the field

lines, and then some of the magnetic material is removed from the disc by the outflow, and the field strength decreases slightly (negative growth rate). This process continues until the magnetic field is in a steady state.

Fig. 4.13 demonstrates the evolution of the nonlinearity in the α-quenching model

$$\alpha \propto \left(\frac{1}{1 + B^2/B_{\rm eq}^2} \right).$$

Globally, we see a short linear, kinematic growth phase, of the order of 1 Gyr. The dashed line shows that this short phase predominantly takes place in the inner regions of the disc, Which is also demonstrated by the solid lines in Figs. 4.14 and 4.15, where we see a comparatively high growth rate within 5 kpc.

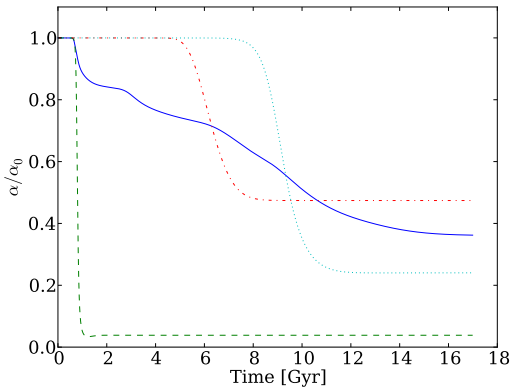

Figure 4.13: Magnitude of the nonlinearity, $(\alpha_{\rm k} + \alpha_{\rm m})/\alpha_0$, in the α-quenching model, globally averaged (solid line), then at 3, 10 and 18 kpc (dashed, dashdot and dotted lines respectively).

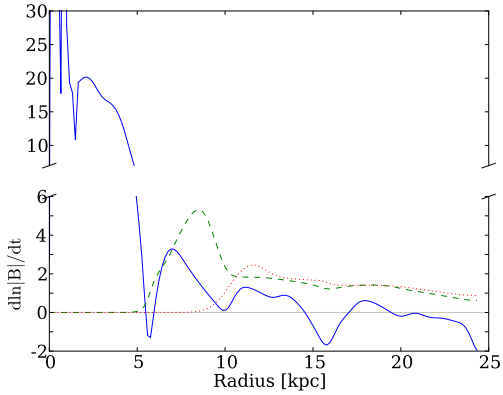

Figure 4.14: Growth rate of the total magnetic field strength for the α-quenching model, at times of 1.5, 5.5 and 9 Gyr (solid, dashed and dotted lines respectively).

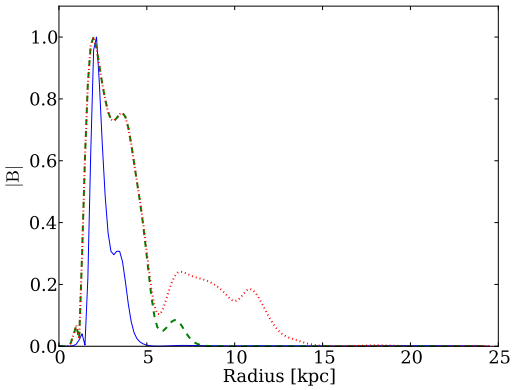

Figure 4.15: Normalised magnitude of the total magnetic field strength for the α-quenching model, at times of 1.5, 5.5 and 9 Gyr (solid, dashed and dotted lines respectively).

As time advances, the growth of the magnetic field propagates through the disc. The kinematic growth as we move out through the disc becomes weaker, but lasts longer. We see this via the saturation of the nonlinearity at a galactocentric radius of 10 kpc prior to the saturation at 18 kpc. Again, this is demonstrated in Figs. 4.14 and 4.15, where the kinematic growth phase at each radius lasts longer as we progress through the disc. This is particularly notable in the dotted line in both Figures. At a time of 7 Gyr, globally, the growth of the magnetic field is almost at the end of its kinematic phase. The magnetic field at this point has ceased growth within $\simeq 10$ kpc, due to the saturation of the dynamo in the region. We observe this propagation throughout the entirety of the disc in M31.

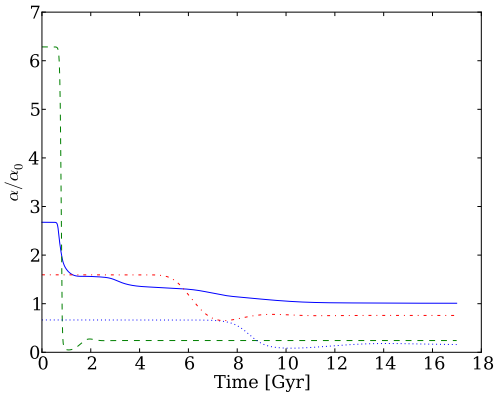

Figure 4.16: Magnitude of the nonlinearity, $(\alpha_k+\alpha_m)/\alpha_0$, in the dynamical α model, globally averaged (solid line), then at 3, 10 and 18 kpc (dashed, dashdot and dotted lines respectively).

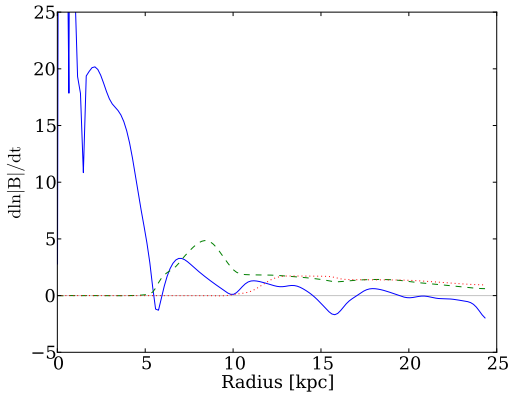

Figure 4.17: Growth rate of the total magnetic field strength for the dynamical α model, at times of 0.3, 3.0 and 7.0 Gyr (solid, dashed and dotted lines respectively).

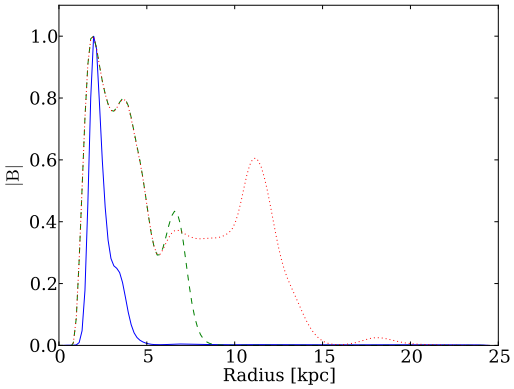

Figure 4.18: Normalised magnitude of the total magnetic field strength for the dynamical α model, at times of 0.3, 3.0 and 7.0 Gyr (solid, dashed and dotted lines respectively).

Figs. 4.16 to 4.18 demonstrate the time dependent growth of the nonlinearity and the magnetic field for the dynamical α model

$$\alpha \propto (\alpha_k + \alpha_m)\,.$$

Fig. 4.16 shows a good general agreement with the evolution of the nonlinearity of the α-quenching model (Fig 4.16). The exception arises in the magnitude of the nonlinearity in the various regions in the disc. In the inner regions of the disc, the nonlinearity grows towards a larger magnitude than in the other regions. Predominantly, the initial growth takes place in the inner 5 kpc (See Fig. 4.17) in the terms including $\alpha_{\rm m}$ in Eqn. (3.11) again, in good general agreement with the α-quenching model.

Both the α-quenching and dynamical α models evolve similarly and result in comparable magnetic field profiles (see Fig. 4.19). The main differences in the overall evolution of the magnetic field are the speed of growth, and the final profile of the magnetic field. The dynamical α dynamo grows quicker than the α- quenching dynamo. The resulting azimuthal magnetic field profile is stronger in the extremities of the disc in the α-quenching. This could be explained by the lower magnitude outflow in those regions removing smaller amounts of helicity in the dynamical α model, and hence the magnetic field is slightly smaller in magnitude in the steady state.

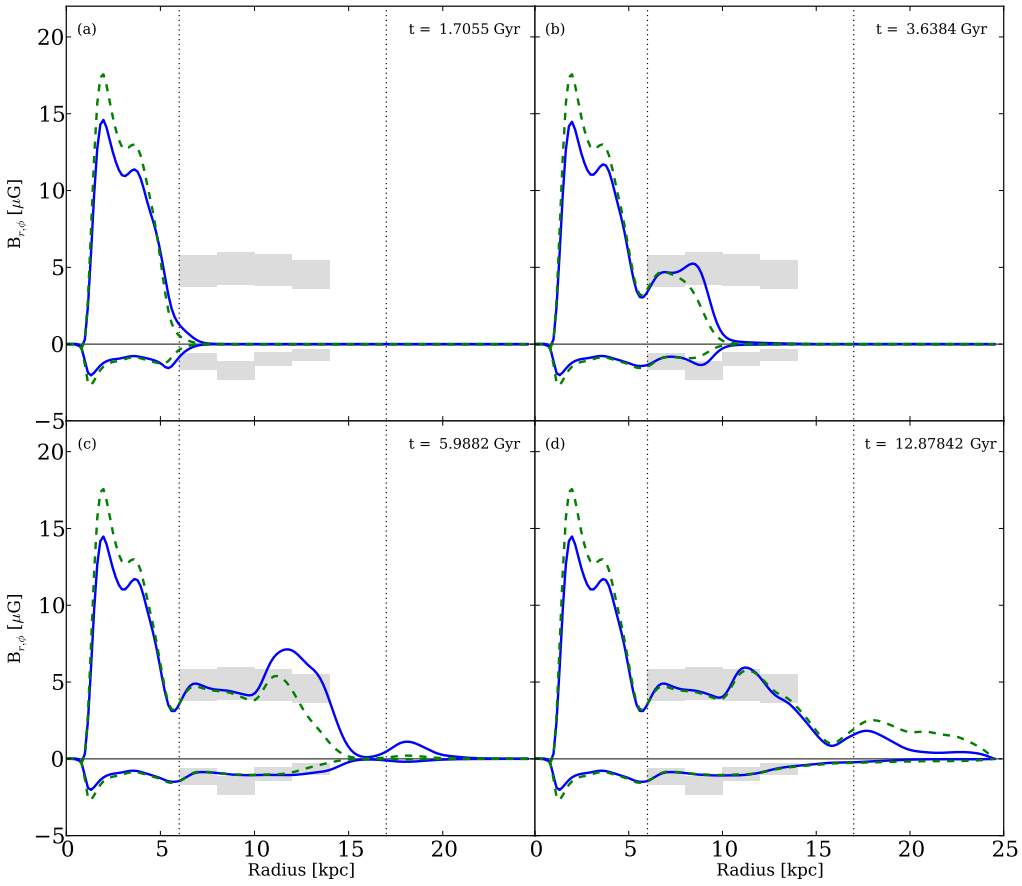

Figure 4.19: Snapshots of the azimuthal and radial magnetic field profile (positive and negative lines respectively), obtained from the dynamical α model (solid lines), and α-quenching models, with the optimum value of $R_{U_z} = 1.5$. Dotted vertical lines define the region $6 < r < 17\,\mathrm{kpc}$, in which the outflow is most prominent, and based solely on the observations of star formation of Tabatabaei & Berkhuijsen (2010). (a) The early, shear dominated strong growth phase. (b)-(d) The weaker, nonlinear growth phase.

4.4 Saturation of the dynamo with constant α_{k}

Given the uncertainty in the exact nature of the α-effect, we now consider a dynamical α model where the kinetic component is $\alpha_{\mathrm{k}} = 1$, instead of $\alpha_{\mathrm{k}} = l_0^2 \Omega\,(r)\,/h\,(r)$, and α_{m} varies with time, as before. We can test the effects of using a constant α_{k} with radius.

We find differences in the way the magnetic field evolves in the dynamical α regime between the use of the constant and non- constant $\alpha_{\rm k}$. We investigate by monitoring how the nonlinearity in each case evolves.

For the nonlinearity in the dynamical model

$$\alpha \propto (\alpha_{\rm k} + \alpha_{\rm m}) \,,$$

where $\alpha_{\rm m} < 0$, we observe similar global evolution to the α-quenching model, where the nonlinearity begins at the same magnitude throughout the disc (see Fig. 4.20), where the growth of the field begins kinematically, then undergoes a nonlinear growth phase, followed by saturation of the dynamo and no growth occurs afterwards.

The use of a constant α with radius prevents the propagational growth from small to large radii found using a non-constant α.

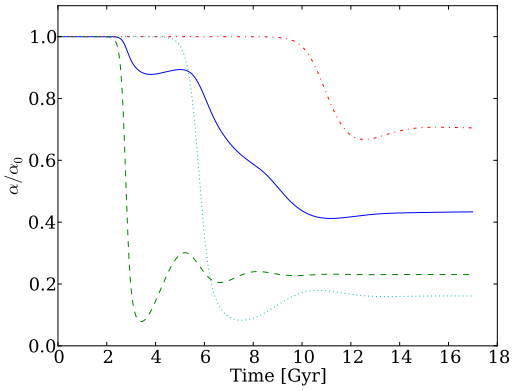

Figure 4.20: Magnitude of the nonlinearity in the dynamical α model, $(\alpha_{\rm k} + \alpha_{\rm m})/\alpha_0$, with $\alpha_{\rm k} = 1$, globally averaged (solid line), then at 3, 10 and 18 kpc (dashed, dashdot and dotted lines respectively).

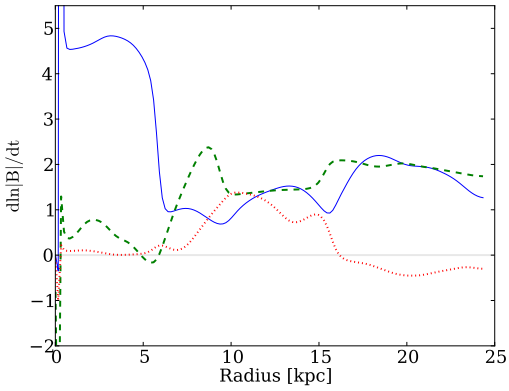

Figure 4.21: Growth rate of the total magnetic field strength for the dynamical α model with $\alpha_{\rm k} = 1$, at times of 0.3, 3.0 and 7.0 Gyr (solid, dashed and dotted lines respectively).

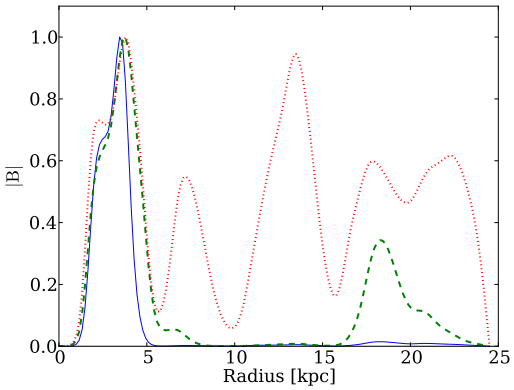

Figure 4.22: Normalised magnitude of the total magnetic field strength for the dynamical α model with $\alpha_{\rm k} = 1$, at times of 0.3, 3.0 and 7.0 Gyr (solid, dashed and dotted lines respectively).

In Figs. 4.22 and 4.23 we see a difference to the growth in Figs. 4.18 and 4.19. We now see a much stronger non-kinematic growth phase whilst using $\alpha_{\rm k} = 1$ in comparison with the non-constant $\alpha_{\rm k}$. We also see a later period of growth in the outer regions of the disc in comparison with the non-constant model.

4.5 Sensitivity to model inputs

Reproducing observations with theoretical models is a difficult task, and the averaging and smoothing implemented with the observational data used in this chapter could arguably be having undesirable effects on the results obtained. In order to investigate this, we further discuss the effect of small variations in two sets of observational inputs; the scale height of the H I disc, and the rotation curve. These quantities are chosen as a result of the observational data being smoothed considerably.

From the disc scale height in Fig. 4.4, we see that the model flaring used is a rather simplistic fit to the data. The first alternative possibility is that the disc could be flared to a lesser extent than estimated, so we adopt the extreme of a flat disc (the dotted line in the left panel of Fig. 4.23). The second possibility is that the disc is flared to a greater extent than we have modelled, hence we look at an exponential disc which begins at the same height as the main model, but then its scale height increases slightly quicker as we move further through the disc until at the outer edge of the disc, the scale height is roughly twice that of the main model. We take both of these examples, and show the

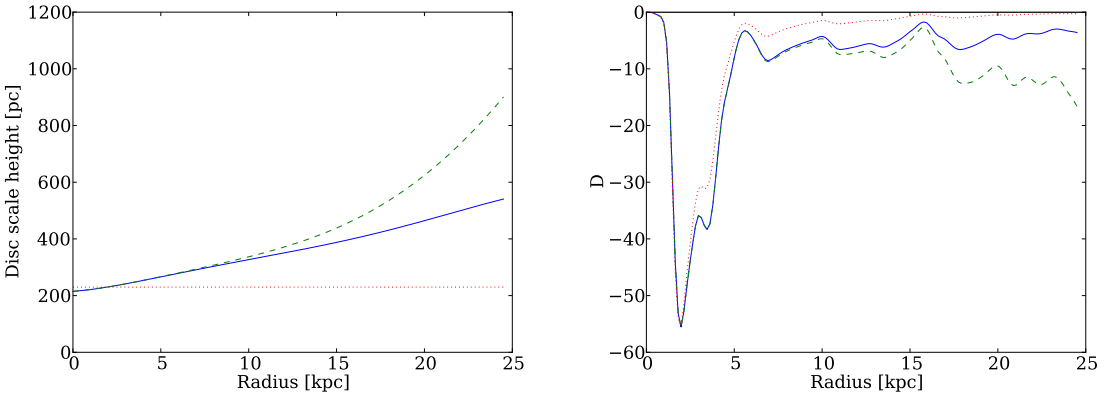

Figure 4.23: *Left panel*: Variations in the degree of disc flaring, used as a test of the sensitivity of the model to certain parameters. The solid line is the original model we used from Fig. 4.4. The dotted line is a flat disc of scale height 230pc (chosen so that the local dynamo number in the inner regions of the disc is comparable to that for the original flared model [right panel]), and the dashed curve demonstrates a more extreme degree of flaring than that of the original model. *Right panel*: Variations in the local dynamo number as a result of varying the disc scale height shown in the left panel. The solid line shows the local dynamo number using the original model from Fig. 4.7. The dotted line shows the result for the flat disc, and the dashed line shows the result obtained from the disc with the highest degree of flaring.

results using the dynamical α model using $\alpha_{\rm k} = 1$, with the optimum value of $R_{U_z} = 1.5$. The results are shown in Fig. 4.24.

The difference in the magnetic field profile when using different scale heights is clear. With the flat disc, a lower magnitude magnetic field is observed, and for the more flared disc, the magnetic field is stronger in the region of stronger flaring. The larger local dynamo number in the outer regions of the disc caused by the more flared disc, shown in Fig. 4.23 leads to a greater amount of growth in this region. The magnetic pitch angle is greatly affected by the alteration of the scale height. For the flat disc, the magnetic field is much less azimuthal, and hence the magnetic pitch angle is greatly increased. Using the more flared disc, the magnetic field becomes slightly more azimuthal and hence the magnetic pitch angle is slightly decreased in magnitude. With a flat disc, the azimuthal component of the magnetic field is removed more from the inner regions of the disc (Eqns. 2.20 and 2.21), resulting in more of the radial component, B_r being added to the inner regions, increasing the pitch angle. In a flared disc, the balance of removal of the azimuthal component shifts towards the outer regions, and hence the radial component does not increase as much, hence reducing the increase in the pitch angle.

In order to investigate the sensitivity of the model to changes in the rotation curve, we adopt each of the spiral arm rotation curves introduced in Section 4.2.3 and shown

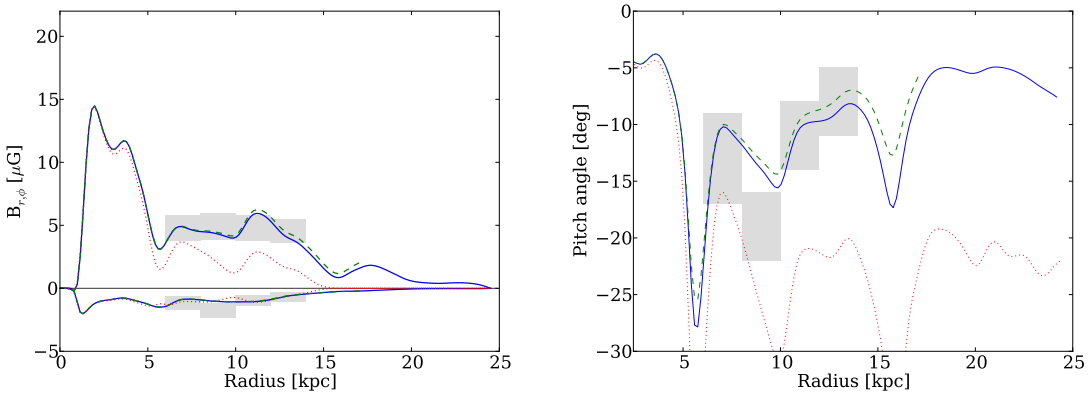

Figure 4.24: *Left panel:* Azimuthal (positive lines) and radial (negative lines) magnetic field components for the dynamical α model, for the different disc models demonstrated in Fig. 4.23 (solid, dashed and dotted lines respectively). The grey boxes denote observational values of the regular magnetic field from Fletcher *et al.* (2004). *Right panel:* Pitch angles the dynamical α model, for the different disc models demonstrated in Fig. 4.23 (solid, dashed and dotted lines respectively). The grey boxes denote observational values of the regular magnetic field as tabulated in Fletcher *et al.* (2004). Note that increasing only the flaring of the disc has very little effect on the magnitude of the pitch angle, and we only see comparable differences in the very outer regions of the disc; the difference between a flat disc and the flared disc is considerable.

here in Fig. 4.25. We also revert to using one disc flaring, the original model from Section 4.2.1. We smooth the rotation curves of the spiral arms, resulting in interesting feature differences in the local dynamo number. The results are shown in the lower panels of Fig. 4.25.

We retain the results for the averaged rotation curve for comparison. There are clear differences between the azimuthal magnetic field profiles between the two models, and very little difference in the radial field component. This is most likely a result of $\partial\Omega/\partial r$ entering the equation for the azimuthal component. It would appear that the magnetic field profile given by the rotation curve for the northern spiral arm (shown by the dashed line) is much closer to the observational data than the rotation curve of the southern spiral arm (shown by the dotted line). However, the pitch angle given by the southern spiral arm appears to be a closer fit to the observational data. The magnetic pitch angle is affected by changes in the rotation curve, but still remains within the uncertainty in the observations.

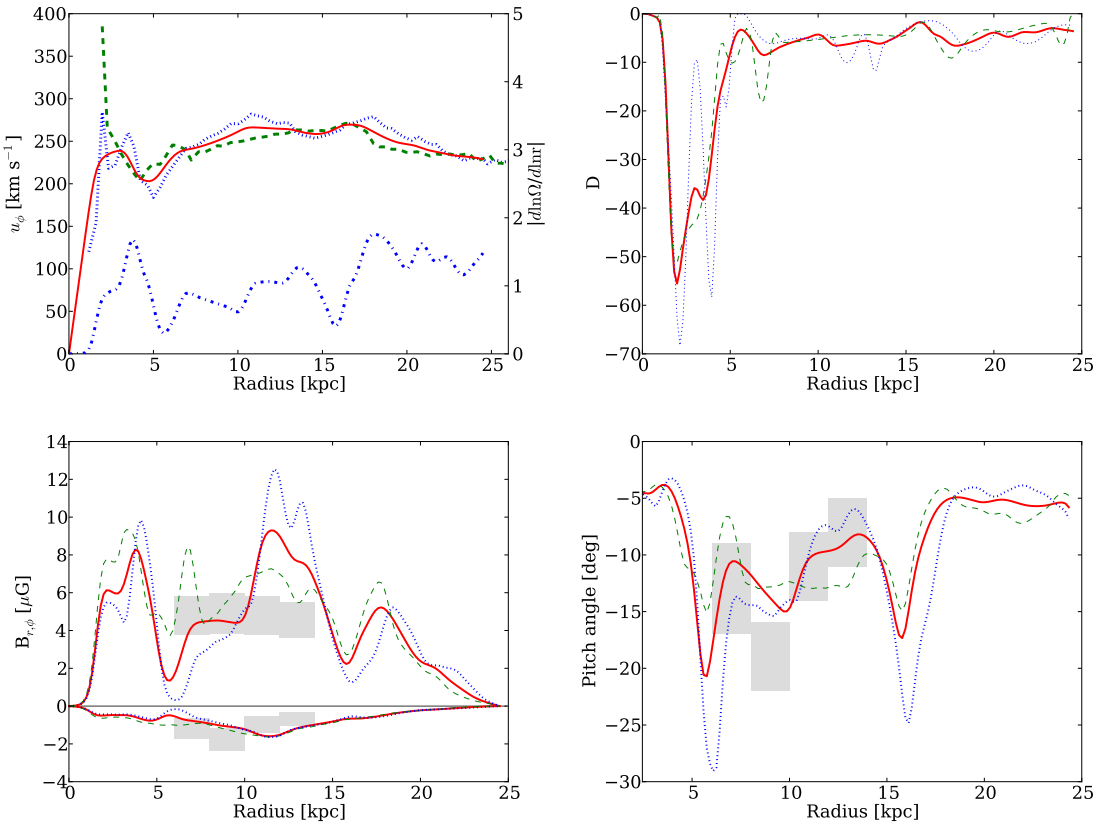

Figure 4.25: *Upper left panel*: Our smoothed rotation curve (solid line) and the rotation curves of both spiral arms as in Fig. 4.6. The dashdot line denotes the local shear. *Upper right panel*: Variations in local dynamo number based on the individual rotation curves of the spiral arms as given in the upper left panel. The solid line shows the result for the averaged rotation velocity, the dashed line gives the result for the receding arm and the dotted line shows the outcome of using the approaching arm. *Lower left panel*: Azimuthal (positive lines) and radial (negative lines) magnetic field components for the dynamical α model, for the different rotation curves demonstrated in the upper left panel (The lines correspond to the arms as described above). *Lower right panel*: Pitch angles for the dynamical α model, for the different rotation curves. The grey boxes denote observational values as tabulated in Fletcher *et al.* (2004).

4.6 Summary

In this chapter, we have investigated both the α-quenching and dynamical α models with the inclusion of a vertical outflow for the galaxy M31.

It has been shown that the observed pitch angles of the magnetic field can be reproduced well, upon application of the galactic outflow derived from observed values of star formation rate.

Observations of the regular magnetic field strength can also be reproduced with the α-quenching model, and the dynamical α dynamo is shown to saturate at 1/5 equipartition. Upon normalisation, the dynamical α results demonstrate very good agreement with the results using α-quenching in terms of magnetic field profile in radius.

The thin disc no-z model has been shown to evolve propagationally from the centre to the outer regions of the galactic disc using both α-quenching and dynamical α models. This result can be sensitive to the treatment of the kinetic component of the α- effect, $\alpha_{\rm k}$. Using $\alpha_{\rm k} = 1$ throughout the galactic disc (instead of using the formula, $\alpha_{\rm k} = l^2\Omega/h$) allows the magnetic field to grow in the outer regions of the disc (after the initial, kinematic growth phase in the inner regions of the disc) prior to the middle region $6 < r < 14\,{\rm kpc}$, contrary to the propagational evolution described for a non-constant $\alpha_{\rm k}$.

The magnetic field strength and pitch angle can also be sensitive to differences in quantities such as the disc scale height, and the rotation curve. Increases in the degree of disc flaring renders the magnetic field more azimuthal, decreasing the magnitude of the pitch angle of the magnetic field. Variations in the rotation curve affect the magnetic field when converted to the angular velocity, $\Omega\,(r)$, and further to $\partial\Omega/\partial r$. Increases in $\partial\Omega/\partial r$ lead to increased azimuthal field strength, hence reducing the magnitude of the pitch angle.

In this study we derive the input parameters, R_ω, R_α and R_{U_i} directly from observations. We only vary however the coefficient for the vertical flow, and leave the other two alone. We have in Chapter 3 that R_α has an effect in that below a certain threshold, dynamo action is not possible, however further study is required to judge how sensitive the model is to both of our untouched input variables.

The method we have used to fit our simulation results to the observations, where useful, is not the most efficient method of fitting; in reality it provides us with the opportunity to make only a visual judgement of the fit. It would be beneficial in future studies to make use of more sophisticated numerical methods of fitting so that more quantitative data on the fit can be ascertained.

———

Chapter 5

The Triangulum Galaxy

M33

NGC598

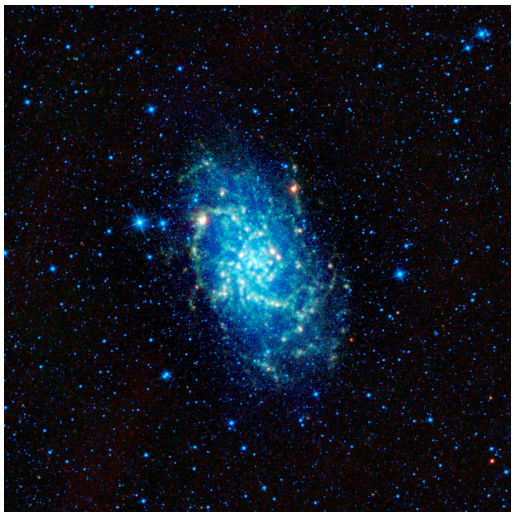

Image credit: NASA/JPL-Caltech/UCLA

5.1 Introduction

The Triangulum galaxy (M33, NGC598) lies at a distance of 840kpc, and at an inclination of $56° \pm 1°$ (Tabatabaei *et al.*, 2008). Its inclination allows for equally good determination of the magnetic field components parallel and perpendicular to the line of sight of the observations. The disc of M33 is warped, making it difficult to judge the accuracy of the observations. The magnetic field of M33 is considered to be comprised of more than

the single, axisymmetric mode magnetic field of M31. It was shown by Tabatabaei *et al.* (2008) that not only axisymmetric $m = 0$, but bisymmetric $m = 1$ and vertical $k = 1$ modes (k is used as a vertical wavenumber which would fit into eigenvalue solutions to the dynamo equations, in the same way they were introduced in Chapter 2) make up the regular magnetic field of M33 (with the warping of the disc being considered as a possible reason for the presence of the vertical component of the magnetic field). The pitch angles of the axisymmetric $m = 1$ mode magnetic field are large ($\simeq 45°$).

M33 is a galaxy with moderate gas density, and abundant in areas of high star formation, making it a good candidate for study using our models, as these properties are different to those of M31, which has low gas density and a low star formation rate. M33 is a spiral galaxy, but unlike M31, has a weaker, discontinuous spiral pattern.

5.2 Observational data

5.2.1 Gaseous disc scale height

We propose a model for the H I disc scale height given by two points of data in Section 6.2 of Tabatabaei *et al.* (2008), taken from (Baldwin, 1981), whereby the scale height of the disc is 250pc at $r = 3\,\mathrm{kpc}$ and rises steadily to 650pc at $r = 5\,\mathrm{kpc}$. We retain the data for the inner point; however with the linear relationship we have chosen to take with this galaxy due to having only two observed data points to deal with, the gradient would be unphysical in the inner regions of the disc. We have therefore chosen to reduce the gradient slightly, so the scale height is still approximately $250\,\mathrm{pc}$ at $r = 3\,\mathrm{kpc}$, does not reach $650\,\mathrm{pc}$ at $r = 5\,\mathrm{kpc}$ but still remains physically acceptable. The gas scale height is shown in Fig. 5.2.

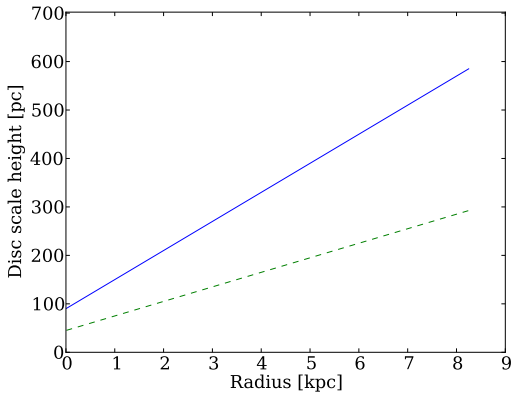

Figure 5.2: Model of the H I disc scale height of M33 (solid line), derived from two points of observational data given in Section 6.2 of Tabatabaei *et al.* (2008). The dashed line shows the model molecular gas scale height.

With the scale height of the H I gas at the inner boundary being of magnitude $\approx$ 200 pc, there is no necessity to truncate and flatten the scale height within the inner regions of the disc. The values of the disc scale height in the inner regions are not identical to the observational data, but follow the same general trend, and non-dimensionalising the disc scale height would not disproportionately reduce the local dynamo number to sub-critical values.

5.2.2 Gas densities

We use the combination of the CO gas surface density and H I surface density, from Gratier *et al.* (2010). This data is in very good agreement with earlier CO and total gas density observations of Heyer *et al.* (2004). We perform an identical smoothing to that which we used for the observational data in Chapter 4. This combination gives the solid line in Fig. 5.3.

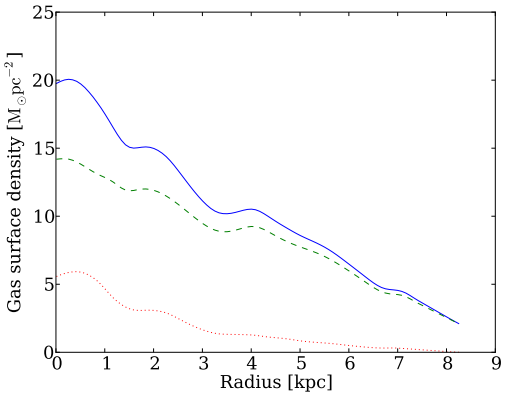

Figure 5.3: Total gas surface density (solid line) calculated as a combination of the H I and CO observations from Gratier *et al.* (2010) (dashed and dotted lines respectively).

There is a definite difference in the gas surface density between M33 and M31 (see Fig. 4.5 for M31): here we observe a steady decrease in density from the inner regions to the outer regions of the disc. As a result of the equipartition field strength being calculated from the gas volume density, we expect that this will result in the strongest magnetic field existing within the inner regions of the disc.

We obtain a value of $B_0 = \sqrt{4\pi\rho_0 v^2} = 8\mu$G taken at the peak density as the reference equipartition field strength.

5.2.3 Rotation curve

We adopt the rotation curve from observations of CO within the inner 1 kpc of the disc, and H I outside this region of Sofue *et al.* (1999) and show in Fig. 5.4 (left panel).

M33 rotates considerably slower (almost a factor of 2 in the maximum velocity) than M31, and with the increase in velocity with radius being slower, $\partial\Omega/\partial r$ is much smaller than that of M31 in the inner regions of the disc. This results in a much smaller local dynamo number for M33 in the inner regions of the disc (Fig. 5.5).

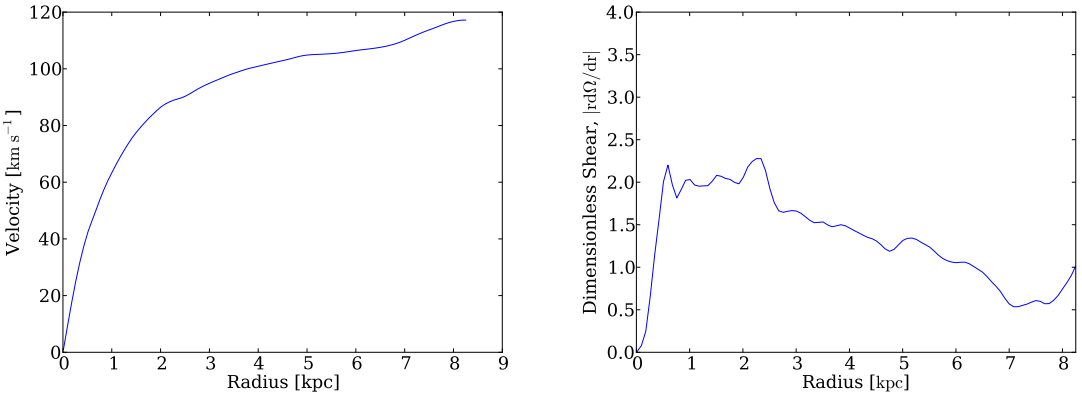

Figure 5.4: *Left panel*: The rotation curve of M33 taken from Sofue *et al.* (1999). *Right panel*: Dimensionless local shear rate, $r|d\Omega/dr|$ calculated using $\Omega(r) = U_\phi/r$.

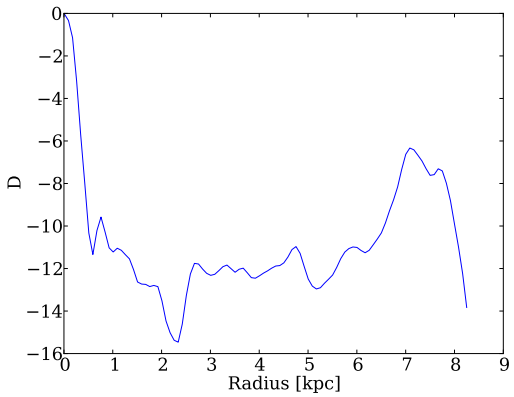

Figure 5.5: The local dynamo number given by Eq. (2.19) using $R_\omega = 11.3$ and $R_\alpha = 0.45$.

With this local dynamo number, with no clearly dominant peaks in comparison with M31, we would expect the resulting magnetic field profiles to be much more evenly distributed throughout the disc. However, given the combination of this with the high gas density, the magnetic field profile should have a small overall negative gradient; however we note the profile is dominated primarily by $B_{\rm eq}$.

5.2.4 Star formation rate

We obtain the values of star formation rate from observations of Heyer *et al.* (2004). M33 has a considerably higher rate of star formation than M31 (some 30 times in the inner

Physical Quantity	Mean Value
Hot phase temp.	2.4×10^6K
Isothermal sound speed	$174.9\,\mathrm{km\,s^{-1}}$
Wind velocity	$276.6\,\mathrm{km\,s^{-1}}$
Mass weighted outflow velocity	$0.55\,\mathrm{km\,s^{-1}}$

Table 5.1: Mean values of the physical quantities described in the development of the outflow, derived from the observations of star formation rate, and gaseous disc scale height, through Eqs. (2.35)-(2.38).

regions).

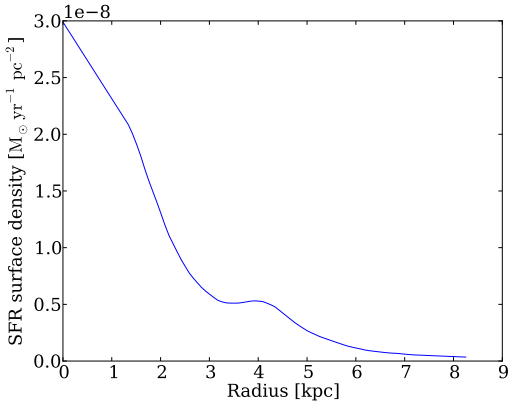

Figure 5.6: The local star formation rate from observations of Heyer *et al.* (2004).

The large values, and peak in star formation rate in the inner regions will give a larger outflow velocity in the inner few kpc, a contrast to the profile of M31, which had a peak in the outflow at around $r = 12\,\mathrm{kpc}$.

5.2.5 Outflow model

With the observed star formation rate density profile of Heyer *et al.* (2004) from Section 5.2.4, along with the gaseous scale heights described in Section 5.2.1 we obtain mean values for the physical quantities described in the development of the outflow model from Section 2.3.1, shown in Table 5.1. We obtain a mass weighted outflow velocity of the order of $0.5\,\mathrm{km\,s^{-1}}$ (Fig. 5.7), which we will calibrate using R_{U_z} in the dynamo equations.

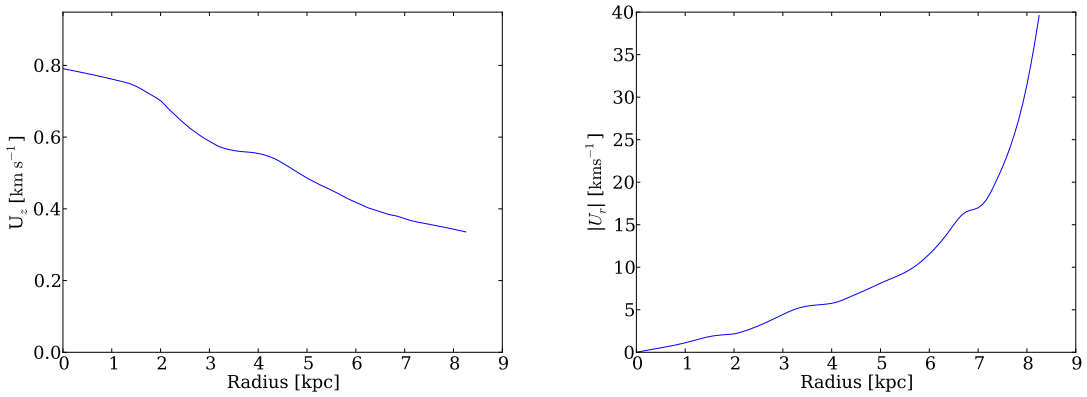

Figure 5.7: *Left panel*: Mass weighted outflow velocity profile as calculated using the outflow model described by Eq. (2.38). *Right panel*: Radial velocity profile as calculated using the model described in Section 2.3.3.

The outflow is as expected, following the general patterns of the gas density, scale heights and star formation rates. We have modelled the radial inflow for this galaxy using the model discussed in Section 2.3.3, but not used it in the dynamo calculations. Where in regions of higher star formation, the vertical outflow is high (driven by a larger supernova explosion rate), the radial inflow is low.

5.3 Results

5.3.1 Galactic parameters

For both the α-quenching and dynamical α models we adopt the following parameters for non-dimensionalisation, characteristic of the observed profiles used in the discussion. We take $h_0 = 0.5\,\mathrm{kpc}$ $\Omega_0 = 14.6\,\mathrm{km\,s^{-1}\,kpc^{-1}}$ and $l_0 = 0.1\,\mathrm{kpc}$, which leads to a value of $\alpha_0 = 0.29\,\mathrm{km\,s^{-1}}$. We take $\eta_\mathrm{t} = 1.0 \times 10^{26}\mathrm{cm^2 s^{-1}}$, and use $R_0 = 8.25\,\mathrm{kpc}$ to be the disc radius in which our observations lie. These parameters are used to derive the dimensionless parameters $R_\omega = 11.3$, and $R_\alpha = 0.45$. We consider values of R_{U_z} in the range $0 < R_{U_z} < 2.0$ in order to calibrate the outflow velocity.

5.3.2 Dynamos with α-quenching

We use the disc scale height, rotation curve and gas densities to calculate the magnetic field strength and pitch angle for the α-quenching model for M33 using the parameters and observations introduced in Sections 5.2.1 to 5.3.1, and compare with observations of

the regular magnetic field of M33 of Tabatabaei *et al.* (2008). For the regular magnetic field profile, shown in Fig. 5.8, we find higher than observed magnitude for low R_{U_z}, and with increasing values, we see a suppression of the magnetic field strength, this being greater in the regions where the vertical outflow is greater. The magnetic field saturates at around the equipartition field strength in the α-quenching model, similarly to the results for M31 in Chapter 4. It is clear from the observations of the regular magnetic field (Tabatabaei *et al.*, 2008), that the regular magnetic field for M33 is of a magnitude much smaller than the equipartition field strength (approximately $1-2\mu G$, in comparison with the peak equipartition field strength of $8\mu G$ calculated above).

We observe an optimum value of $R_{U_z} = 2.0$ (chosen via the dynamical α results, which we will discuss in the next section), which allows the radial magnetic field component to rest within the observational ranges (upon averaging in a similar way to the way we treated the results for M31 in Chapter 4). As predicted, the magnetic field profiles have peaks in the inner regions of the disc, and decrease with a moderate gradient with radius. The outflow for M33 reduces the saturation level of the magnetic field more in the inner regions, as a result of its higher magnitude in this region.

5.3.3 Dynamos with a dynamical α

We again use the parameters and observations outlined above, and use the disc scale height, rotation curve and gas densities to calculate the magnetic field strength and pitch angle for the dynamical α model for M33. We adopt the optimum value of $R_{U_z} = 2.0$, which gives the pitch angles which most closely match the observations, shown in Fig. 5.9. The first notable difference in models (see Fig. 5.8) is the magnitude of the regular magnetic field. In a similar fashion to that of M31, the dynamo in the dynamical α model saturates at a much lower level than in the α-quenching model (1/3 of the equipartition field strength for the optimum value of $R_{U_z} = 2.0$). Fortunately, the results of the dynamical α model are of the magnitude of the observed values of Tabatabaei *et al.* (2008), with no normalisation required. This is because the observations of Tabatabaei *et al.* (2008) show that M33 has a lower than equipartition magnetic field, in close agreement with the dynamical α model saturating at a magnitude lower than equipartition. The profiles of the total magnetic field, and the radial and azimuthal components calculated using the model follow the general trend of the observations, with peak values in the inner regions followed by lower values outside this region.

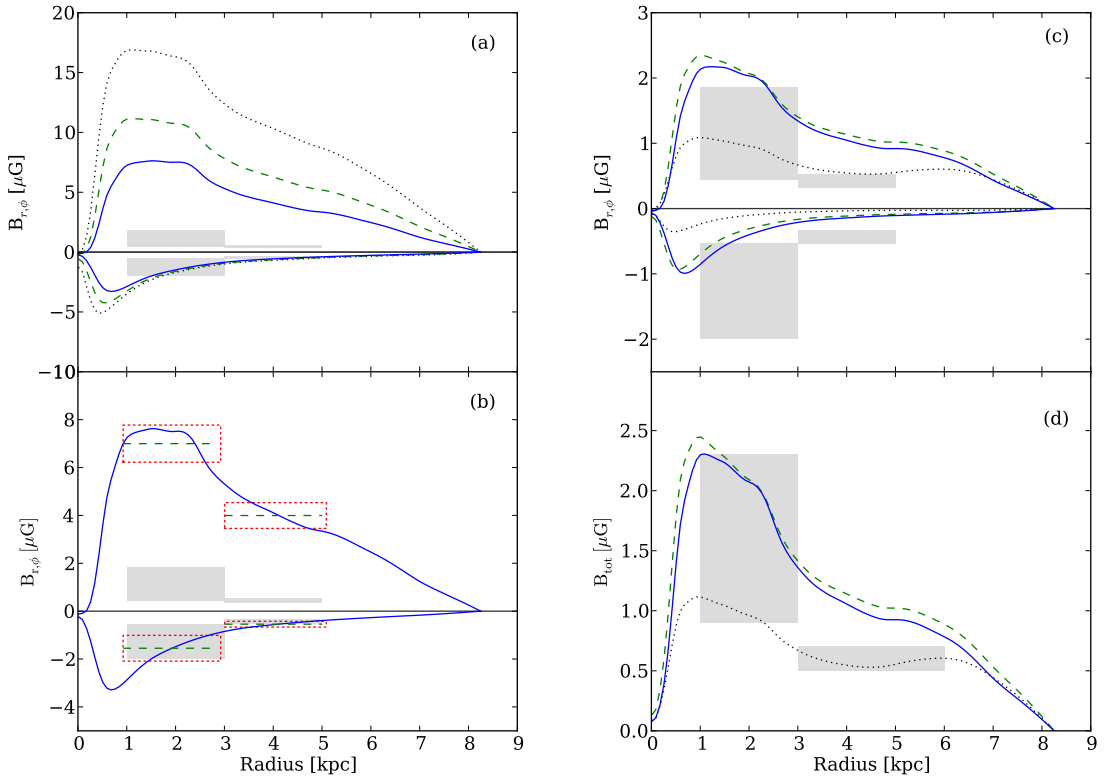

Figure 5.8: (a) Azimuthal (positive lines) and radial (negative lines) magnetic field components for the α-quenching model, for $R_{U_z} = 0.0$, 1.0 and 2.0 (dotted, dashed and solid lines respectively). (b) Azimuthal and radial magnetic field profiles (positive and negative lines respectively) from the α-quenching model using $R_{U_z} = 2.0$. The dashed line represents averaging over regions of width 2 kpc within the range $1 < r < 5$ kpc, with the dotted line being a single standard deviation from the mean. (c) Azimuthal (positive lines) and Radial (negative lines) magnetic field components for the dynamical α model, for $R_{U_z} = 0.0$, 1.0 and 2.0 (dotted, dashed and solid lines respectively). (d) Total magnetic field strength from the dynamical α model using $R_{U_z} = 2.0$. The grey boxes in all panels denote observational values from Tabatabaei *et al.* (2008).

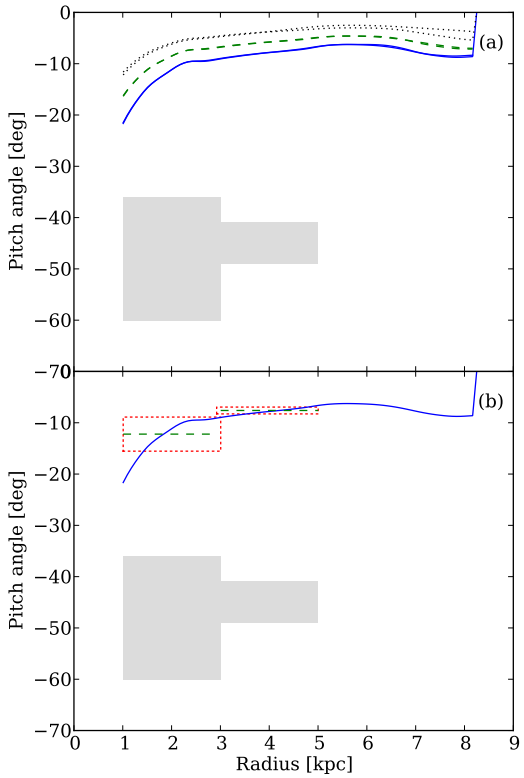

Figure 5.9: Pitch angles for both the α-quenching (a) and dynamical α (b) models. Solid lines show optimum $R_{U_z} = 2.0$. Dashed and dotted lines denote the results for $R_{U_z} = 1.0$, and 0.0 respectively. The grey boxes denote observational values of Tabatabaei *et al.* (2008).

5.3.4 Pitch angle of the magnetic field

The pitch angle of the magnetic field is not well reproduced with either of the α-quenching or dynamical α models (see Fig. 5.9). We find pitch angles of the order 1/5 that of the observed values, however the shape of the pitch angle profile is not too dissimilar from the observations in the regions given. This suggests that it is possible that the dynamo in M33 operates in a different way to that of M31. An analytic calculation of the pitch angle was conducted by Tabatabaei *et al.* (2008), which found the magnitude of the pitch angle to be in the range 15–20°, similar magnitudes to those we have produced. Fig. 5.10 shows that the predicted relationship between R_{U_z} and the pitch angle of the magnetic field, whereby the pitch angle increases with increasing R_{U_z}, is correlates with the simulated results, with both non-linearities operating similarly. The analytical model agrees with the simulations, but both unfortunately differ significantly from the observations.

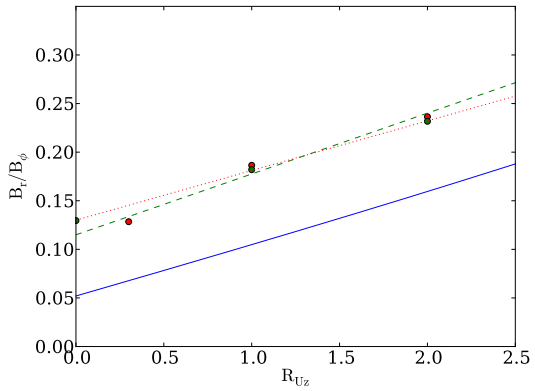

Figure 5.10: An analytical representation of the ratio between radial and azimuthal magnetic field components with varying R_{U_z}, given by Eq 2.44 (solid line). Green circles show the results for the α-quenching model and red circles show the results for the dynamical α model.

5.4 Summary

In this chapter we have presented observational data for M33, and investigated dynamo models for both the α-quenching and dynamical α dynamo non-linearities, with the inclusion of our star formation derived galactic outflow.

The observed profiles and magnitudes of the magnetic field of Tabatabaei *et al.* (2008) are reproduced with reasonable accuracy using the dynamical α model, which saturates

at around $1-2\mu$G. Both α-quenching and dynamical α models agree with the structure of the magnetic field, producing a peak in the inner regions of the disc, followed by a moderate decrease with radius.

The magnitude of the local pitch angle of the magnetic field is not well produced for M33. This could possibly be attributed to the operation of the dynamo of M33 being different to that of M31. The key differences to M31 are that the dynamical α gives the correct saturated magnetic field strength, but does not produce large enough pitch angles. Higher azimuthal modes of the magnetic field are present in M33, but not M31 , and this could contribute to a large observed pitch angle. The presence of higher modes in the observed magnetic field indicates that the dynamo in M33 is different to the M31 dynamo. This could be due to M33's higher gas density, higher star formation rate or its slower rotation. Non-axisymmetric models could prove useful and help to understand the differences.

The inclusion of a radial inflow (5.7, right panel) could increase the magnitude of the pitch angle, having a similar effect to that of including a vertical outflow, as discussed in Section 2.3.2 (including and increasing U_r in the analysis of the steady state equations leads to an increase in the pitch angle). It is possible that further investigations could resolve the issue of the currently too small pitch angles.

With the observations of Tabatabaei *et al.* (2008) demonstrating the presence of a vertical magnetic field component in M33, it may be that the no-z model is inappropriate for use with this galaxy. A 2D model could possibly give results more consistent with the observations.

———

Chapter 6

The Whirlpool Galaxy

M51a

NGC5194

Image Credit: NASA/ESA

6.1 Introduction

The Whirlpool galaxy (M51, NGC5194) lies at a distance of 8.4Mpc (Schuster *et al.*, 2007), seen nearly face on. It is a galaxy high in gas density. Unlike and of the other galaxies in this study, M51 has a companion galaxy, M51b (NGC5195), with which it interacts. This interaction leads to a high rate of star formation. M51 has a strong total magnetic field, however a weaker than equipartition regular magnetic field (Fletcher *et al.*,

2011).

In comparison with M31 and M33, the regular magnetic field is made up of $m = 0$ and $m = 2$ azimuthal modes. Unlike M31 and M33, M51 has a very definite and strong spiral structure, with large interarm regions where magnetic field is known to exist; however in these regions, the magnitude of the magnetic pitch angle changes by about $\pm 15°$, in comparison with the pitch angle in the magnetic arms, which are of the order $20°$ (Fletcher *et al.*, 2011).

6.2 Galactic observations

6.2.1 Gaseous disc scale height

We consider a model for the H I disc scale height, based on the profile derived for the ionised gas (free electrons) of M51 by Berkhuijsen *et al.* (1997). We adapt this to give an estimate of the H I disc scale height. The four data points of Berkhuijsen *et al.* (1997) are fitted with an exponential. We then reduce the magnitude of the scale height, to roughly account for the larger density of H I than the free electrons. Issues which may arise from such a reduction may include the results being difficult to verify. Also, reducing the scale height to such an extent in the inner regions of the disc could allow the dynamo to dominate in these areas, possibly masking what could be happening in the outer regions of the disc. We adopt the flaring and scale height as shown in Fig. 6.2. The molecular gas scale height is taken to be half that of the H I scale height, to hold consistency with the previous chapters.

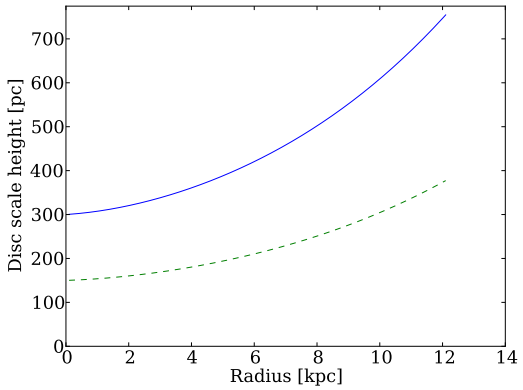

Figure 6.2: Model of the H I disc scale height of M51 (solid line), derived from the free electron-derived disc scale height of Berkhuijsen *et al.* (1997). The dashed line shows the model molecular gas scale height.

The disc of M51 is shown to flare quite quickly within a radius half that of M31, more than doubling it's height by the time it reaches $r = 12\,\mathrm{kpc}$.

6.2.2 Gas densities

We use the combination of the CO gas surface density and H I surface density, from Schuster *et al.* (2007). We perform a similar smoothing to that which we used for all of the data in Chapter 4. This combination gives the solid line in Fig. 6.3.

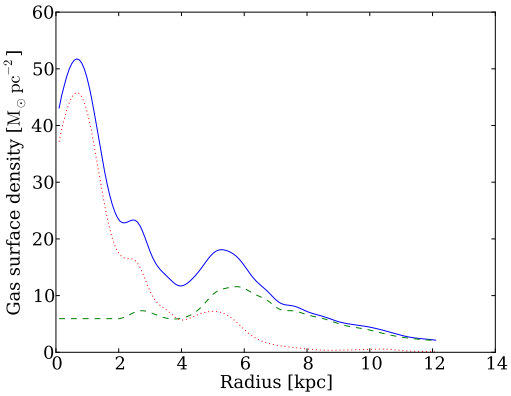

Figure 6.3: Total gas surface density (solid line) calculated as a combination of the H I and CO observations from Schuster *et al.* (2007) (dashed and dotted lines respectively).

Fig. 6.3 shows again quite a distinctive radial density distribution, with a large peak in the density in the inner regions of the disc(at least 5 times larger than the peak of density for M31), and we observe a relatively quick decrease in density from the inner regions of the disc to around $r = 4\,\mathrm{kpc}$. beyond this there is a slower decrease in density towards the outer regions of the disc. As a result of the equipartition field strength being calculated from the volume gas density, we would expect that this will result in the majority of the output magnetic field to exist within the very inner regions of the disc.

We obtain a value of $B_0 = \sqrt{4\pi\rho_0 v^2} = 12\mu\mathrm{G}$ taken at the peak density as the reference equipartition field strength.

6.2.3 Rotation curve

We adopt the rotation curve from observations of Garcia-Burillo *et al.* (1993) shown in Fig. 6.4.

M51 rotates faster than M33, and marginally slower than M31 (the peak velocity of M31 being of the order $250\,\mathrm{km\,s^{-1}}$). This results in a local dynamo number for M51 comparable to that of M31 in magnitude (Fig. 6.5 for M51; Fig. 4.7 for M31).

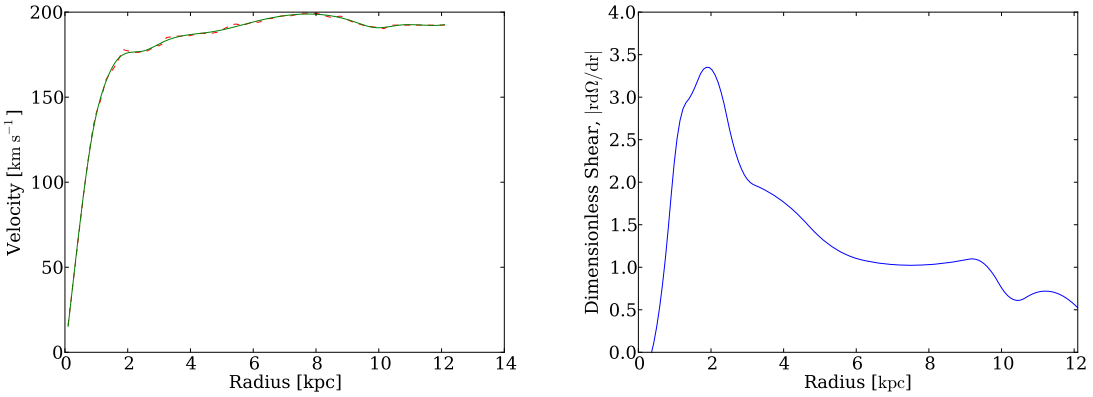

Figure 6.4: *Left panel*: The unsmoothed (dashed line) and smoothed (solid line) rotation curves of M51 taken from Sofue *et al.* (1999). *Right panel*: Dimensionless local shear rate, $r|d\Omega/dr|$ calculated using $\Omega\,(r) = U_\phi/r$.

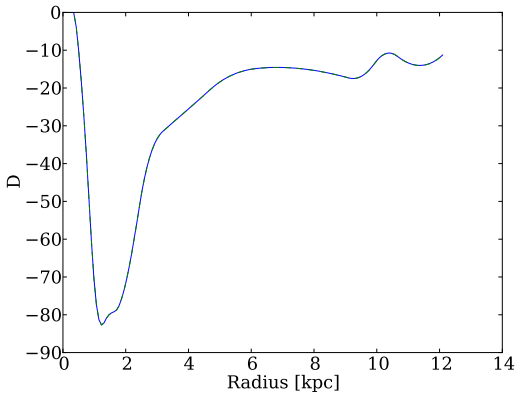

Figure 6.5: The local dynamo number given by Eq. (2.19).

Using this alongside the gas density profile, we would expect that the magnetic field will be dominant within the inner regions of the disc, a direct contrast to M31, where the peak gas density in the 10 kpc ring allowed the magnetic field to be more evenly distributed throughout the disc.

6.2.4 Star formation rate

We obtain the values of star formation rate from Schuster *et al.* (2007) shown in Fig. 6.6. M51 has a considerably higher rate of star formation than M33 (some 10 times in the inner regions, so even 300 times that of M31 in the inner regions, a massive difference).

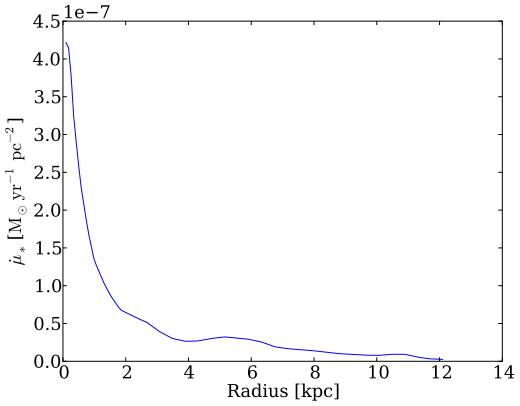

Figure 6.6: The local star formation rate from observations of Heyer *et al.* (2004).

The peak in star formation rate towards the centre of the disc will give a larger outflow velocity in the inner regions.

6.2.5 Outflow and inflow models

With the observed star formation rate density profile from Section 6.2.4, along with the gaseous scale heights described in Section 6.2.1 we obtain mean values for the physical quantities described in the development of the outflow model from Section 2.3.1, shown in Table 6.1. We obtain a mass weighted outflow velocity of the order of $0.7\,\mathrm{km\,s^{-1}}$ (Fig. 5.7), which we will calibrate using R_{U_z} in the dynamo equations. We have modelled the radial inflow for this galaxy in this instance (see Fig. 6.7, right panel); however we have again not used it in the dynamo calculations, showing a very large radial inflow in the outer regions of the disc. In comparison with observations of Shetty *et al.* (2007), we see a slightly higher peak in the outer regions than expected, but in the rest of the disc a comparable magnitude of the radial velocity is achieved.

6.3 Results

6.3.1 Galactic parameters

For both the α-quenching and dynamical α models we adopt the following parameters for non-dimensionalisation, characteristic of the observed profiles used in the discussion. We take $h_0 = 0.5\,\mathrm{kpc}$, $\Omega_0 = 25\,\mathrm{km\,s^{-1}\,kpc^{-1}}$ and $l_0 = 0.1\,\mathrm{kpc}$, which leads to a value of $\alpha_0 = 0.5\,\mathrm{km\,s^{-1}}$. We take $\eta_\mathrm{t} = 1.0 \times 10^{26}\mathrm{cm^2 s^{-1}}$, and use $R_0 = 12.1\,\mathrm{kpc}$ to be

Physical Quantity	Mean Value
Hot phase temp.	3.9×10^6K
Isothermal sound speed	$226.9\,\mathrm{km\,s^{-1}}$
Wind velocity	$358.7\,\mathrm{km\,s^{-1}}$
Outflow velocity	$0.72\,\mathrm{km\,s^{-1}}$

Table 6.1: Mean values of the physical quantities described in the development of the outflow, derived from the observations of star formation rate, and gaseous disc scale height, through Eqs. (2.35)-(2.38).

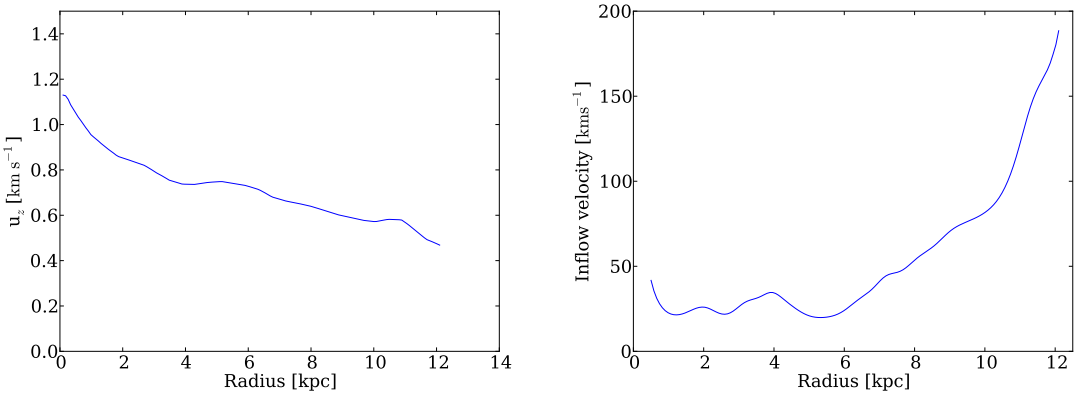

Figure 6.7: *Left panel*: Mass weighted vertical velocity profile as calculated using the wind model described by Eq. (2.38). *Right panel*: Radial inflow velocity profile as calculated using the wind model described by Eq. (2.47). Again, the inflow velocity profile was not used in the dynamo calculations.

the disc radius in which our observations lie. These parameters are used to derive the dimensionless parameters $R_\omega = 19.28$, and $R_\alpha = 0.77$. We consider values of R_{U_z} in the range $0 < R_{U_z} < 3.5$ in order to calibrate the outflow velocity.

6.3.2 Dynamos with α-quenching

We use the disc scale height, rotation curve and gas densities to calculate the magnetic field strength and pitch angle for the α-quenching model for M51 using the parameters and observations introduced in Sections 6.2.1 to 6.3.1, and compare with observations of the magnetic field of M51 of Fletcher *et al.* (2011). For the regular magnetic field profile, shown in Fig. 6.8, we find a higher than observed magnitude for low R_{U_z}, and with increasing values, we see a suppression of the growth. The magnetic field saturates at around the equipartition field strength in the α-quenching model, similar to simulation results for M31 and M33. The regular magnetic field for M51 is of a magnitude much smaller than the equipartition field strength (approximately $2-4\mu G$, in comparison with the peak equipartition field strength of $12\mu G$ calculated above) (Fletcher, 2011).

We find an optimum value of $R_{U_z} = 3.5$, which allows the radial magnetic field profile to lie within the observational ranges (upon averaging in a similar way to the way we treated the results for M31). The magnetic field profiles have peaks in the inner regions of the disc, and decrease with a moderate gradient with radius. The outflow for M51 reduces the saturation level of the magnetic field more in the inner regions.

6.3.3 Dynamos with a dynamical α

We again use the parameters and observations outlined above, and use the disc scale height, rotation curve and gas densities to calculate the magnetic field strength and pitch angle for the dynamical α model for M51. We adopt the optimum value of $R_{U_z} = 3.5$, which gives the pitch angles that are the best match to the observations of Fletcher *et al.* (2011) shown in Fig. 6.9. The first notable difference in models (see Fig. 6.8) is the magnitude of the regular magnetic field. In a similar fashion to that of M31 and M33, the dynamo in the dynamical α model saturates at a much lower level than in the α-quenching model (1/3 of the equipartition field strength for the optimum value of $R_{U_z} = 3.5$). Also, in a similar fashion to M33, the results of the dynamical α model are of the same magnitude of the observed field strengths obtained by Fletcher *et al.* (2011), with no normalisation required. The profiles of the total magnetic field, and the radial and azimuthal components calculated using the model are of the same order of magnitude as the observations, however the positive gradient in the observations is not

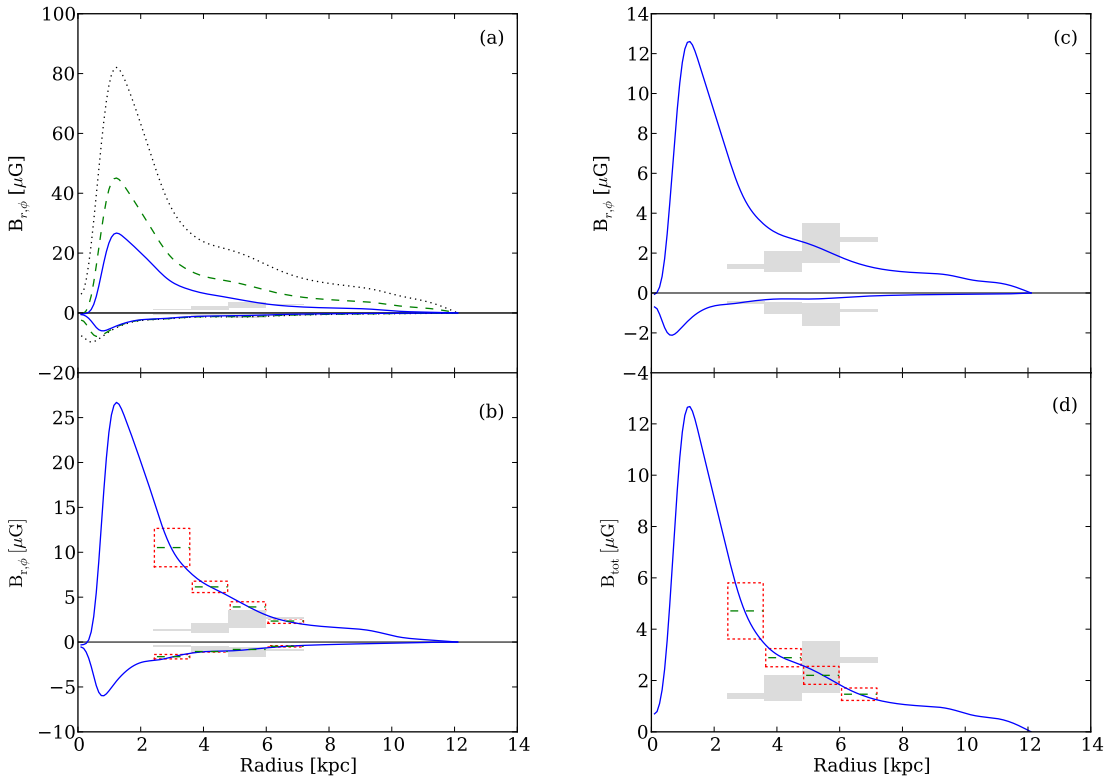

Figure 6.8: (a) Azimuthal and radial magnetic field components for the α-quenching model, for $R_{U_z} = 0.0$, 1.5 and 3.5 (dotted, dashed and solid lines respectively). (b) Azimuthal and radial magnetic field profiles from the α-quenching model using $R_{U_z} = 3.5$. The dashed line represents averaging over regions of width 2 kpc within the range $1 < r < 5$ kpc, with the dotted line being a single standard deviation from the mean. (c) Azimuthal and Radial magnetic field components, for the dynamical α model, for $R_{U_z} = 0.0, 1.5$ and 3.5 (dotted, dashed and solid lines respectively). (d) Total magnetic field strength from the dynamical α model using $R_{U_z} = 3.5$. The grey boxes in all panels denote observational values from Fletcher *et al.* (2011).

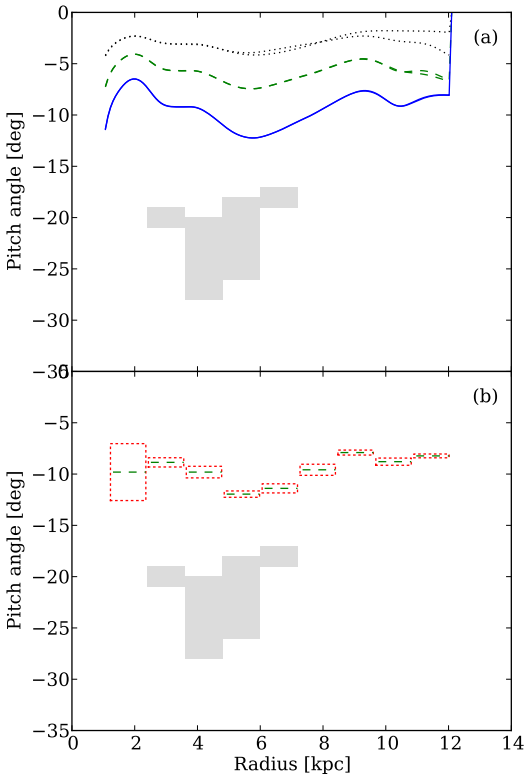

Figure 6.9: Pitch angles for both the α-quenching (a), and dynamical α (b) models. Solid lines show optimum $R_{U_z} = 3.5$. Dashed and dotted lines denote the results for $R_{U_z} = 1.5$, and 0.0 respectively. The grey boxes denote observational values of Tabatabaei *et al.* (2008).

reproduced, as a result of the peaks in gas density and star formation rate in the inner regions of the disc.

6.3.4 Pitch angle of the magnetic field

The pitch angle of the magnetic field is not well reproduced with either of the α-quenching or dynamical α models (see Fig. 6.9). We find pitch angles of the order 1/2 that of the observed values, and the shape of the profile is not convincingly reproduced. This suggests that it is possible that the dynamo in M51 operates in a different way to that of M31, and in a similar way to M33. Fig. 6.10 shows that the predicted relationship between R_{U_z} and the pitch angle of the magnetic field, whereby the pitch angle increases with increasing R_{U_z}, again, holds, with a near perfect fit to the analytic result, showing how a simple analytic test can be used to explain the results of a much more complicated simulation, even when the observations are not agreed with by either the analytical or simulated models.

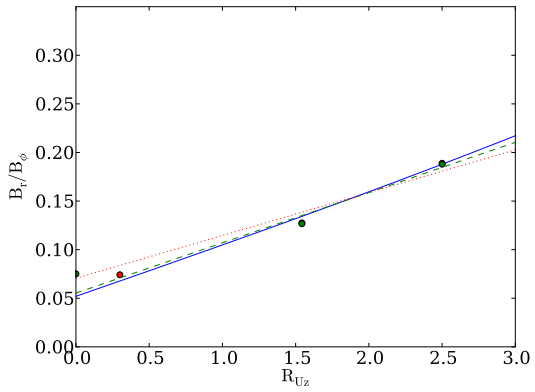

Figure 6.10: An analytical representation of the ratio between radial and azimuthal magnetic field components with varying R_{U_z}, given by Eq 2.44 (solid line). Green circles show the results for the α-quenching model and red circles show the results for the dynamical α model.

6.4 Summary

In this chapter we have presented observational data for M51, and investigated the evolution of the dynamo for both the α- quenching and dynamical α dynamo models, with the inclusion of our star formation derived galactic outflow.

It has been shown that, as for M33, we have a galaxy with a weak regular magnetic field, for which the dynamical α model can produce the correct field strength, but in this case not the correct profile. The model also produces pitch angles which are of a shape and magnitude inconsistent with the observations. The regular magnetic field observations of Fletcher *et al.* (2011) can be reproduced in magnitude using the dynamical α model. Both α-quenching and dynamical α models agree with the structure of the magnetic field, producing a peak in the inner regions of the disc, followed by a fast decreasing gradient within the inner 4 kpc, followed by a gradual decrease out to $r = 12$ kpc, however both fail to reproduce the observed increase in field strength with radius.

The magnitude of the local pitch angle of the magnetic field is not well produced for M51, in a similar way to that of the results for M33. This could possibly be attributed to the operation of the dynamo of M51, again being different to that of M31. Again, higher mode magnetic fields are present in the observations of M51 (an m=2 mode is present at all radii), and this would contribute to a larger observed pitch angle at some azimuths than the results of the axisymmetric models suggest.

———

Chapter 7

The Fireworks Galaxy
NGC6946

Image Credit: Public domain.

7.1 Introduction

The Fireworks galaxy (NGC6946) lies at a distance of 5.5Mpc (Tully, 1988), and is inclined at $38° \pm 2°$ (Boomsma *et al.*, 2008). It is a galaxy high in gas density, and abundant in areas of high star formation, similar to M51. In contrast to M51 however, NGC6946 has a less pronounced spiral structure. This galaxy is known to host "magnetic arms" that sit between the gaseous spiral arms (Ehle & Beck, 1993) and these magnetic

arms contain strong ($\simeq 10\mu$G) and well ordered regular magnetic fields, with a similar relationship between the observed regular magnetic field and the equipartition magnetic field to that observed for M31, where the regular magnetic field strength is comparable with the equipartition field strength, in contrast to M33 and M51. NGC6946 has a strong total magnetic field ($\simeq 25\mu$G in the inner regions of the disc) (Beck, 2007).

7.2 Galactic observations

7.2.1 Gaseous disc scale height

Observations of the H I disc scale height of NGC6946 are limited and somewhat uncertain due to the probable warping of the disc in the inner regions. Beck (2007) suggested for simplicity using a flat disc of $h(r) = 100\,\mathrm{pc}$. Where this could be argued to be a suitable approximation for simple dynamo models, it limits what can be ascertained in terms of scientific understanding from results. A flat disc model would not necessarily reflect the physical structure of the gaseous disc, and lack of consistency between our studied galaxies may somewhat dilute the validity of our results. We adopt a disc flaring comparable in nature to that for M51, as M51 has a similarly shaped gas density profile to that of NGC6946, and hence we can infer a similar degree of flaring to this disc model

$$h = \frac{1}{3} h_0 e^{r/L_h}, \tag{7.1}$$

where L_h is the approximate line of sight length through the disc, which for NGC6946 we take as $\simeq 9\,\mathrm{kpc}$.

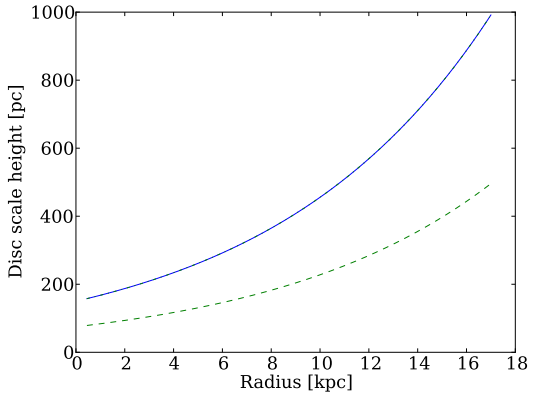

Figure 7.2: Model of the H I disc scale height of NGC6946 (solid line) given by Eq. (7.1). The dashed line shows the model molecular gas scale height.

7.2.2 Gas densities

We use the combination of the CO gas surface density and H I surface density, from Crosthwaite & Turner (2007). This data shows a very high density of molecular hydrogen, however further discussion (R. Beck, private communication) suggests that this may not be accurate (it was discussed that possible warping of the disc of NGC 6946 may be contributing to the somewhat questionable observational values, and that any data considered would have to be treated as having a relatively large uncertainty, giving a greater freedom in the ranges of values that could be chosen), and it was decided that we should flatten the density in the inner regions of the disc to a more acceptable value of $12 M_{\odot} pc^{-2}$. We perform a similar smoothing to that which we used for all of the data in Chapter 4. This combination gives the solid line in Fig. 7.3.

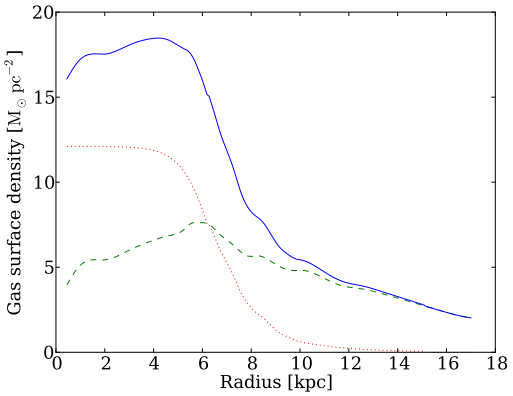

Figure 7.3: Total gas surface density (solid line) calculated as a combination of the H I and CO observations from Crosthwaite & Turner (2007) for corrected CO profile (dashed and dotted lines respectively).

The peak in surface density is wider in this galaxy in comparison with the others we have studied, and the overall profile remains quite high throughout the disc.

We obtain a value of $B_0 = \sqrt{4\pi\rho_0 v^2} = 5.5\mu$G as the reference equipartition field strength.

7.2.3 Rotation curve

We adopt the rotation curve from observations of Sofue *et al.* (1999), and impose solid body rotation in the inner regions of the disc, in a similar fashion to that of M31, and show in Fig. 5.4.

NGC6946 has quite a similar rotation curve to that of M31, with a peak in the mid-section of the disc, and a large maximum velocity. As a result, we see a similar local dynamo number for NGC6946 in the inner regions of the disc to that of M31 (Fig 7.5).

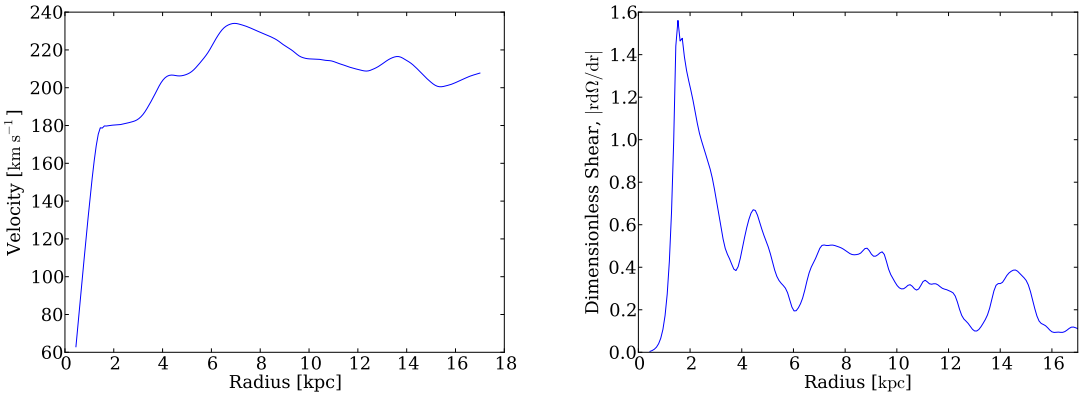

Figure 7.4: *Left panel*: The rotation curve of NGC6946 taken from Sofue *et al.* (1999). *Right panel*: Dimensionless local shear rate, $r|d\Omega/dr|$ calculated using $\Omega(r) = U_\phi/r$.

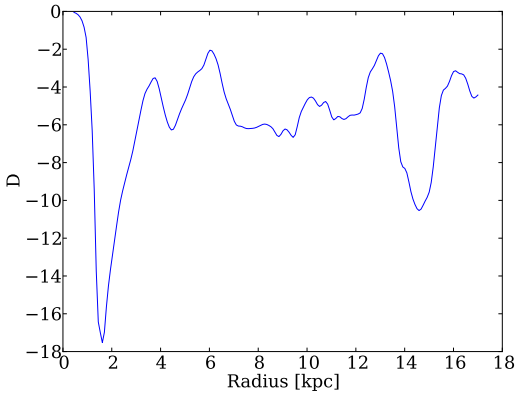

Figure 7.5: The local dynamo number given by Eq. (2.19).

With this local dynamo number taken into account with the wide distribution of gas density, we may expect an output magnetic field profile similar in shape to that of M31, with the exception that the peak in the magnetic field will reside in the inner regions of the disc rather than the mid-section.

7.2.4 Star formation rate

We obtain the values of star formation rate from Crosthwaite & Turner (2007). NGC6946 has a considerably higher rate of star formation then M31 (some 70 times in the inner regions), but observations only extend to $r = 8\,\mathrm{kpc}$. Studying the profile in Fig. 7.6, we should be able to follow the rate of star formation in a pseudo- exponential fashion

Physical Quantity	Mean Value
Hot phase temp.	1.4×10^6K
Isothermal sound speed	$122.5\,\mathrm{km\,s^{-1}}$
Wind velocity	$193.6\,\mathrm{km\,s^{-1}}$
Outflow velocity	$0.49\,\mathrm{km\,s^{-1}}$

Table 7.1: Mean values of the physical quantities described in the development of the outflow, derived from the observations of star formation rate, and gaseous disc scale height, through Eqs. (2.35)-(2.38).

towards the outer boundary we adopt of $r = 17\,\mathrm{kpc}$.

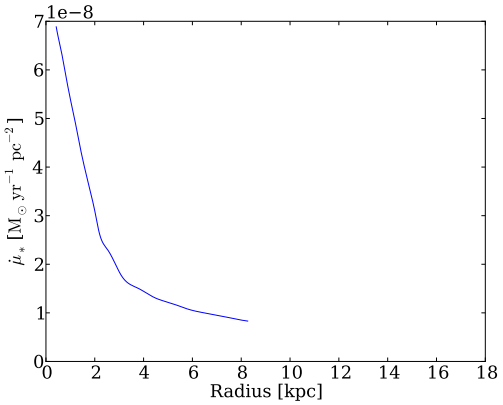

Figure 7.6: The local star formation rate from observations of Crosthwaite & Turner (2007).

We expect that the large peak in star formation rate will give a larger outflow velocity in the inner regions.

7.2.5 Outflow model

With the observed star formation rate density profile from Section 7.2.4, along with the gaseous scale heights described in Section 7.2.1 we obtain mean values for the physical quantities described in the development of the outflow model from Section 2.3.1, shown in Table 7.1. We obtain a mass weighted outflow velocity of the order of $0.5\,\mathrm{km\,s^{-1}}$ (Fig. 7.7), which we will calibrate using R_{U_z} in the dynamo equations.

We have modelled the radial inflow for this galaxy (see Fig. 7.7, right panel), showing a very large radial inflow in the outer regions of the disc, similar to that of M51 (Fig.

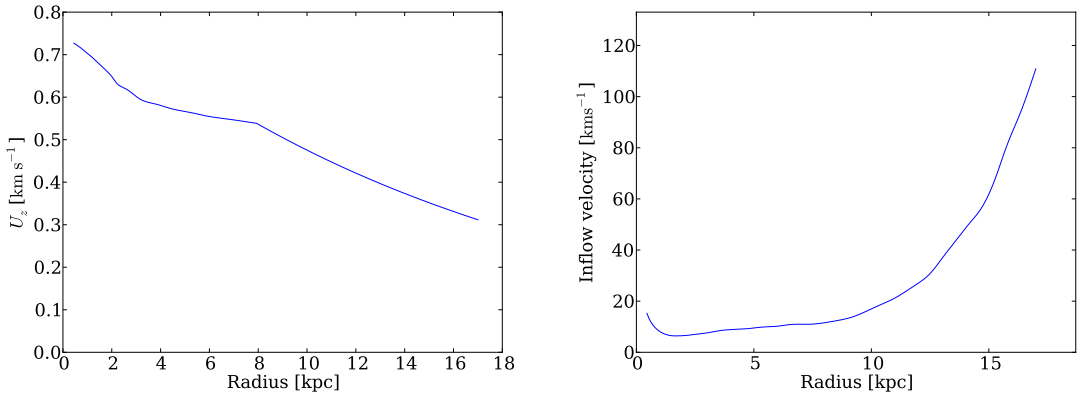

Figure 7.7: *Left panel*: Mass weighted vertical velocity profile as calculated using the wind model described by Eq. (2.37). *Right panel*: Radial inflow velocity profile as calculated using the wind model described by Eq. (2.47)

6.7), however with a magnitude approximately 1/10 that of the M51 inflow in the regions of high star formation. We do not use this inflow in the model, as the vertical outflow is our main motivation.

7.3 Results

7.3.1 Galactic parameters

For both the α-quenching and dynamical α models we adopt the following parameters for non-dimensionalisation, characteristic of the observed profiles used in the discussion. We take $h_0 = 0.5\,\mathrm{kpc}$ and $\Omega_0 = 35\,\mathrm{km\,s^{-1}\,kpc^{-1}}$, which leads to a value of $\alpha_0 = 0.7\,\mathrm{km\,s^{-1}}$. We take $\eta_\mathrm{t} = 1.0 \times 10^{26}\mathrm{cm^2 s^{-1}}$, $l_0 = 0.1\,\mathrm{kpc}$, and use $R_0 = 17\,\mathrm{kpc}$ to be the disc radius in which our observations lie. These parameters are used to derive the dimensionless parameters $R_\omega = 27$, and $R_\alpha = 1$. We consider values of R_{U_z} in the range $0 < R_{U_z} < 2.0$ in order to calibrate the outflow velocity.

Note on the observational data

We adopt the observational data of Beck (2007) for NGC6946. The regular magnetic field strengths are derived from the energy density of the magnetic field $E_B = B^2/8\pi$. Beck (2007) calculated the field strengths assuming that the disc scale height was constant.

7.3.2 Dynamos with α-quenching

We use the disc scale height, rotation curve and gas densities to calculate the magnetic field strength and pitch angle for the α-quenching model for NGC6946 using the parameters and observations introduced in Sections 7.2.1 to 7.3.1, and compare with observations of the magnetic field of NGC6946 of Beck (2007) (with a modest margin of error of $\pm 1\mu$G). For the regular magnetic field profiles, shown in Fig 7.8 (left panel), we find a marginally higher than observed magnitude for low R_{U_z}, and with increasing values, we see a suppression of the growth. The magnetic field saturates at around the equipartition field strength in the α-quenching model for $R_{U_z} = 2.0$. We observe an optimum value of $R_{U_z} = 2.0$ which allows the magnetic field profile to rest comfortably within the observational ranges.

For the optimum value of R_{U_z}, the profile we find does not fit the observations quite as well as for the dynamical non-linearity. At $r = 2\,\mathrm{kpc}$, the model regular magnetic field strength is approximately twice that observed, and at 5 kpc, the model output is 0μG, contrary to the 5μG observed at that radius. In contrast to the method we used to average the results for M31, the observations for NGC6946 are less discrete (the data points are 0.5 kpc apart), hence we do not apply an averaging to the model outputs.

There are large fluctuations in the profiles for the magnetic field components, resulting from the large variations in the local shear (Fig. 7.4 (right panel)), in comparison with the other galaxies where the local variations in the shear were not quite as dramatic as with NGC 6946.

7.3.3 Dynamos with a dynamical α

We again use the parameters and observations outlined above, and use the disc scale height, rotation curve and gas densities to calculate the magnetic field strength and pitch angle for the dynamical α model for NGC6946. We adopt the optimum value of $R_{U_z} = 2.0$, which gives the largest pitch angles shown in Fig. 7.9. Again, as in the other galaxies, the dynamo in the dynamical α model saturates at a much lower level than in the α-quenching model (1/5 of the equipartition field strength for the optimum value of $R_{U_z} = 2.0$). As a result, we have to normalise our results to compare with the observations of Beck (2007), by multiplying the profiles by a factor of 5.5. The normalised profiles of the total magnetic field, and the radial and azimuthal components calculated using the model are of the correct order of magnitude as the observations, and we find moderate agreement in the averaging of the structure of the magnetic field, showing (beyond the inner regions of the disc) a general decrease in the magnetic field

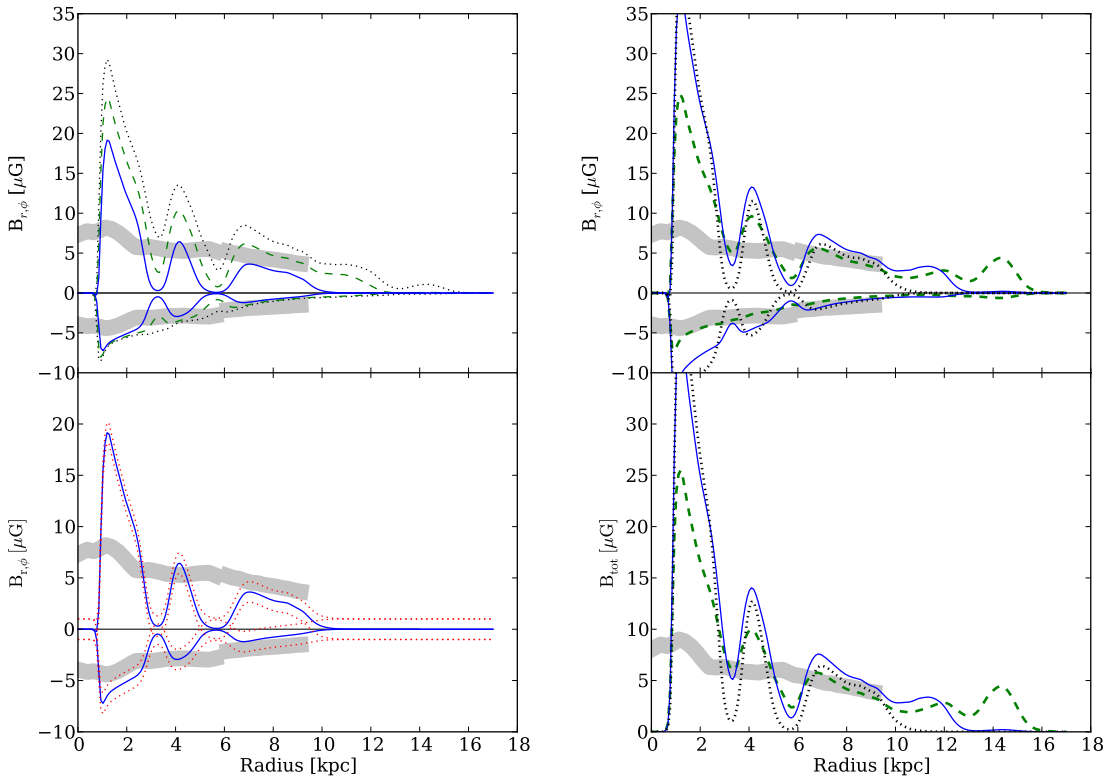

Figure 7.8: (*Upper left panel*): Azimuthal (positive lines) and Radial (negative lines) magnetic field components for the α- quenching model, for $R_{U_z} = 0.0$, 1.0 and 2.0 (dotted, dashed and solid lines respectively). (*Lower left panel*): Azimuthal and radial magnetic field profiles (positive and negative lines respectively) from the α-quenching model using $R_{U_z} = 2.0$. (*Upper right panel*): Azimuthal (positive lines) and Radial (negative lines) magnetic field components for the dynamical α model, for $R_{U_z} = 0.0$, 1.0 and 2.0 (dotted, dashed and solid lines respectively). (*Lower right panel*): Total magnetic field strength from the dynamical α model using $R_{U_z} = 2.0$. The grey boxes in all panels denote observational values from Beck (2007).

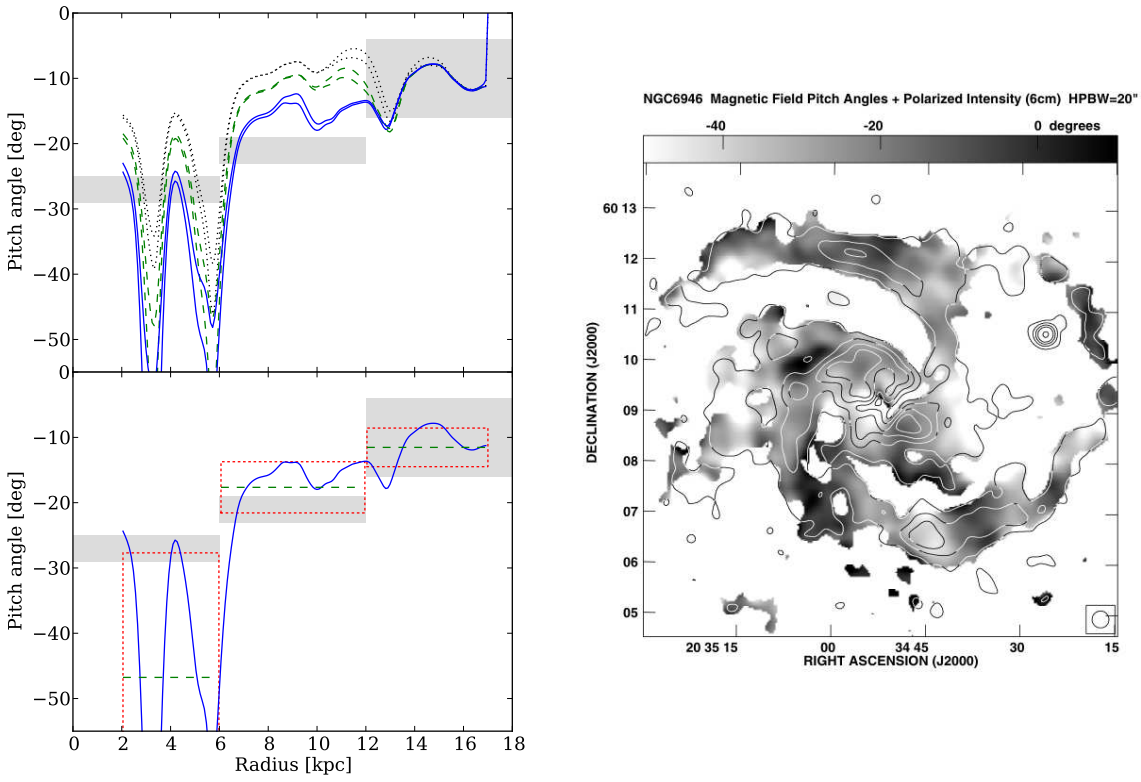

Figure 7.9: (*Left panel*): Pitch angles for both the α- quenching, and dynamical α models. Solid lines show optimum $R_{U_z} = 2.0$. Dashed and dotted lines denote the results for $R_u = 1.0$, and 0.0 respectively. The grey boxes denote observational values of Beck (2007). (*Right panel*): Fig. 16 from Beck (2007): Pitch angles of the magnetic field vectors at 20"resolution and contours of polarized intensity at $\lambda 6.2$ cm.

strength with increasing radius.

7.3.4 Pitch angle of the magnetic field

In Fig. 7.9 there are very big fluctuations in the magnetic pitch angle, in particular in the inner 6 kpc. As the observations of the pitch angle were averaged over three regions by Beck (2007), we can in this instance apply the method used for the averaging of the model outputs used for M31 to average over the three regions. There is a danger here of relying too much on the averaged results, which in this case are only divided into three sections for the entire disc, especially when considering results which fluctuate to the extent they do here. It could be the case that we lose a lot of clarity in the results and miss what could be quite useful information which could otherwise benefit future investigations. We find that the general trend of the pitch angle to decrease with radius is well reproduced, in a very similar fashion to that of M31. The averaging and standard deviation estimates sit within the observational values in all three regions, giving the best results. Fig. 6.10 shows that the predicted relationship between R_{U_z} and the pitch angle of the magnetic field, whereby the pitch angle increases with increasing R_{U_z}, again, holds, with very good agreement between both nonlinearities. The right panel of Fig. 7.9 shows the observational map from which the grey boxes in the left panel are based (the values in the grey boxes are taken directly from the text of Beck (2007), based themselves on the map) and how varied they are in the disc of NGC6946.

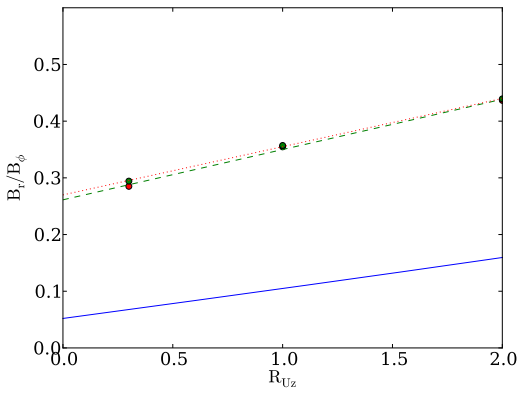

Figure 7.10: An analytical representation of the ratio between radial and azimuthal magnetic field components with varying R_{U_z}, given by Eq 2.44 (solid line). Green circles show the results for the α-quenching model and red circles show the results for the dynamical α model.

7.4 Summary

In this chapter we have presented the observational data for NGC6946 of Beck (2007), and investigated the evolution of the dynamo for both the α-quenching and dynamical α dynamo models, with the inclusion of our star formation derived galactic outflow.

The observed profiles and magnitudes of the magnetic field of Beck (2007) can be reproduced in structure using the α- quenching model. The dynamical α results require upscaling by a multiple of 5.5 to sit on the observations, in a similar fashion to the upscaling used for M31. Both α-quenching and dynamical α models agree with the structure of the magnetic field, producing a peak in the inner regions of the disc, followed by a slowly decreasing gradient beyond the inner 4 kpc, followed by a gradual decrease out to $r = 17\,\mathrm{kpc}$ (where it must be noted that the magnetic field profiles produced in the α-quenching model reduce to negligible values beyond $r = 10\,\mathrm{kpc}$ for the optimum value of R_{U_z}).

The magnitude of the local pitch angle of the magnetic field is relatively well produced for NGC6946, in a similar way to that of the results for M31. This could possibly be attributed to the evolution of the dynamo of NGC6946, being similar to that of M31.

Here we have a galaxy with a strong observed regular magnetic field; like M31. The dynamical α model cannot obtain the correct magnitude of magnetic field strength, but can reproduce the pitch angles, just like in the case of M31.

———

Chapter 8

Conclusions

We have developed a new physically rich model for a flared, thin-disc galactic dynamo, incorporating the effects of observationally derived vertical outflows from the disc, and a dynamical evolution of the α-effect, based on magnetic helicity conservation laws.

We have adapted and combined previous models of supernova evolution and galactic winds in the presence of magnetic fields to derive a mass weighted vertical outflow from a galactic disc, which can be derived directly from observations of star formation.

We have demonstrated that these outflows have a definite and measurable effect on the strength of the magnetic field. It has become clear that the outflows affect the magnetic field in terms of its components in different ways. This varied effect on the components directly affects the pitch angle of the magnetic field; an observable quantity not previously widely studied. An increase in the strength of an outflow from a disc is seen to increase the size of the magnetic pitch angle, hence making the magnetic field more radial in its nature.

There are various sensitivities to the model we have used, and we have explored them, investigating their effects. We in particular chose to investigate the sensitivity to the flaring of the disc, an observable quantity which, as can be seen in most of the galaxies we have studied, has some uncertainty in its nature. Evolution of the model using a flat disc in comparison to a flared disc shows the magnetic pitch angle to increase to values beyond those observed, and also reduces the magnitude of the azimuthal magnetic field below what is observed. The degree of flaring does not have a large effect on the results, so the main difference surfaces when using a flat instead of a flared disc. This justifies the use of a flared disc in such studies.

The strength of the magnetic field and the profile of the magnetic pitch angle can be slightly sensitive to the rotation curve used in these studies. Small changes in the

differential rotation of the disc dictate changes in the local shear rate, which directly affects the Ω-effect. A larger shear will result in an amplification in the azimuthal field. These effect however are quite small, and hence the resulting effects on the magnetic pitch angle are similarly small.

In future studies, where the possiblity of studying these galaxies in more detail arises, it will be interesting to explore these sensitivites more.

We have applied this model to four nearby galaxies; M31, M33, M51 and NGC6946. We have organised them differently in this chapter as a result of the outcome of the study. The galaxies fall into two categories; one where the dynamical α model produces magnetic field strengths considerably smaller than the observed values, and the other where the observed field strengths are reproduced by the model.

The two galaxies where the dynamical α model produces weaker than observed magnetic fields are M31 and NGC6946 and are discussed here:

M31

We obtain a good match to the observed pitch angles and magnetic field profiles described in Fletcher *et al.* (2004), however the more physically derived dynamical α model saturates at 1/5 of the equipartition magnetic field strength, and the magnitude of the observed regular magnetic field in M31 is approximately that of the equipartition strength. The simpler α-quenching model will always saturate at the equipartition, $B_{\rm eq}$ by construction, so the magnetic field strength given by the α-quenching model is of the correct magnitude.

Without an outflow, the pitch angle of the magnetic field in M31 is smaller than observed. With the inclusion of a physically acceptable mass weighted outflow of only approximately 0.4 $\rm kms^{-1}$, the magnetic pitch angle is increased to within the observations with an acceptable margin of error.

Both models predict a substantial magnetic field in the inner galaxy that is not seen in synchrotron emission observations. It is suggested that magnetic fields in this region could be searched for using Faraday rotation measures.

NGC6946

We obtain a good match to the observed pitch angles from both dynamo models. Similarly to M31 the magnetic field in the dynamical α model saturates at approximately

1/5 the equipartition magnetic field strength, much lower than the observed values, so an arbitrary scaling is required to match the model results with the observations.

We observe a reasonable reproduction of the radial profile of the magnetic field strengths for the region $r > 4\,\mathrm{kpc}$ described in Beck (2007), from the α-quenching model.

M31 and NGC6946 Summary

Both M31 and NGC6946 have strong regular magnetic fields, that from observations (Fletcher *et al.*, 2004; Beck, 2007) are known to be roughly of the magnitude of the equipartition magnetic field strength. In both galaxies the dynamical α model can reproduce the observed magnetic pitch angles well, but not the field strength, which is better reproduced (for $r > 4\,\mathrm{kpc}$ in NGC6946) by the simple α- quenching model.

The other group contains our other two galaxies; M33 and M51, and is where the dynamical α model does reasonably well in reproducing magnetic fields of the order of magnitude of the observations.

M33

In contrast to both M31 and NGC6946, for M33, the dynamical α model gives reasonable magnetic field profiles, saturating at around $B \approx 2\mu\mathrm{G}$ in good agreement with the observations of Tabatabaei *et al.* (2008), however the magnitudes of the pitch angles of the magnetic field are not well produced. It is possible that higher, bisymmetric dynamo modes discussed in Tabatabaei *et al.* (2008) are present, which would account for the larger values of observed pitch angles, and cannot be obtained in our axisymmetric model.

M51

In very similar fashion to M33, for M51, the dynamical α model gives reasonable magnetic field profiles, with good agreement in terms of magnitude ($\boldsymbol{B}$ saturates at around $1.4\mu\mathrm{G}$), however the magnitudes of the pitch angles of the magnetic field are not well produced.

M33 and M51 Summary

Both M33 and M51 have weak regular magnetic fields, with magnitudes only a fraction of the equipartition field strength ($B_0 = 8\mu\mathrm{G}$ for M33, and $B_0 = 12\mu\mathrm{G}$ for M51). Both M33 and M51 are very rich in gas and both have very high star formation rates in comparison

with the likes of M31. Perhaps this is a sign that the galactic dynamo operates and saturates differently in different types of galaxies.

Extending beyond this thesis

Beyond this work, it would be interesting to follow up the models by investigating the effects of radial inflows on the galactic dynamo. It was shown that both M33 and M51 may have comparatively high radial inflows in the outer regions of the disc. It is possible that this could be a contributory factor in increasing the pitch angle of the magnetic field in these galaxies.

Also, it would be interesting to see whether additional fluxes, such as the Vishniac-Cho flux could help the magnitude of the magnetic field strength calculated using the dynamical α-model.

Time dependent outflows and azimuthal velocities would be an ideal way to further this investigation. It would be good to see how an outflow magnitude decreasing with time would affect the magnitudes of the magnetic field strengths and pitch angles of the galaxies we have studied.

Bibliography

Baldwin, J. E. 1981 H I spiral structure in M31 and M33 .

Baryshnikova, I., Shukurov, A., Ruzmaikin, A. & Sokoloff, D. D. 1987 Generation of large-scale magnetic fields in spiral galaxies. *Astron. Astrophys.* **177**, 27–41.

Beck, R. 1982 The magnetic field in M31. *Astron. Astrophys.* **106**, 121–132.

Beck, R. 2007 Magnetism in the spiral galaxy NGC 6946, magnetic arms, depolarization rings, dynamo modes, and helical fields. *AA* **470**, 539–556.

Beck, R., Berkhuijsen, E. M. & Hoernes, P. 1998 A deep lambda 20 CM radio continuum survey of M31. *Astron. Astrophys. Supp.* **129**, 329–336.

Beck, R., Berkhuijsen, E. M. & Wielebinski, R. 1978 Detection of polarised radio emission of M31. *Astron. Astrophys.* **68**, L27–L29.

Beck, R., Berkhuijsen, E. M. & Wielebinski, R. 1980 Distribution of polarised radio emission in M31. *Nat.* **283**, 272–275.

Beck, R., Brandenburg, A., Moss, D., Shukurov, A. & Sokoloff, D. 1996 Galactic magnetism: Recent developments and perspectives. *Ann. Rev. Astron. Astrophys.* **34**, 155–206.

Beck, R. & Graeve, R. 1982 The distribution of thermal and nonthermal radio continuum emission of M31. *Astron. Astrophys.* **105**, 192–199.

Beck, R., Loiseau, N., Hummel, E., Berkhuijsen, E. M., Graeve, R. & Wielebinski, R. 1989 High-resolution polarization observations of M31. I - Structure of the magnetic field in the southwestern arm. *Astron. Astrophys.* **222**, 58–68.

Berkhuijsen, E. M. 1977 A radio continuum survey of M31 at 2695 MHz. II - Comparison of radio and optical data. *Astron. Astrophys.* **57**, 9–31.

Berkhuijsen, E. M., Beck, R. & Hoernes, P. 2003 The polarized disk in M 31 at lambda 6 cm. *Astron. Astrophys.* **398**, 937–948.

Berkhuijsen, E. M., Horellou, C., Krause, M., Neininger, N., Shukurov, A. D. P. A. & Sokoloff, D. D. 1997 Magnetic fields in the disk and halo of M51. *Astron. Astrophys.* **318**, 700–720.

Berkhuijsen, E. M. & Wielebinski, R. 1974 A radio continuum survey of M31 at 2695 MHz. I. Observations; comparison of radio continuum data. *Astron. Astrophys.* **34**, 173–179.

Berkhuijsen, E. M., Wielebinski, R. & Beck, R. 1983 A radio continuum survey of M31 at 4850 MHz. I - Observations - List of sources. *Astron. Astrophys.* **117**, 141–144.

Bissantz, N., Englmaier, P. & Gerhard, O. 2003 Gas dynamics in the Milky Way: second pattern speed and large-scale morphology. *Mon. Not. R. Astron. Soc.* **340**, 949–968.

Blackman, E. G. & Field, G. B. 2000 Constraints on the Magnitude of α in Dynamo Theory. *Astrophys. J.* **534**, 984–988.

Boomsma, R., Oosterloo, T. A., Fraternali, F., van der Hulst, J. M. & Sancisi, R. 2008 H I holes and high-velocity clouds in the spiral galaxy NGC 6946. *AA* **490**, 555–570.

Brandenburg, A. & Subramanian, K. 2005 Astrophysical magnetic fields and nonlinear dynamo theory. *Phys. Rep.* **417**, 1–209.

Braun, R. 1991 The distribution and kinematics of neutral gas in M31. *Astrophys. J.* **372**, 54–66.

Braun, R., Thilker, D. A., Walterbos, R. A. M. & Corbelli, E. 2009 A wide-field righ-resolution H I mosaic of Messier 31. I. opaque atomic gas and star formation rate density. *Astrophys. J.* **695**, 937–953.

Cattaneo, F. & Hughes, D. W. 1996 Nonlinear saturation of the turbulent α effect. *Phys. Rev. E* **54**, 4532–+.

Cattaneo, F. & Hughes, D. W. 2009 Problems with kinematic mean field electrodynamics at high magnetic Reynolds numbers. *Mon. Not. R. Astron. Soc.* **395**, L48–L51.

Chemin, L., Carignan, C. & Foster, T. 2009 H I kinematics and dynamics of Messier 31. *Astrophys. J.* **705**, 1395–1415.

Chiba, M. & Lesch, H. 1994 Galactic dynamics and magnetic fields: II. Magnetic fields in barred galaxies. *Astron. Astrophys.* **284**, 731.

Corbelli, E., Lorenzoni, S., Walterbos, R., Braun, R. & Thilker, D. 2010 A wide-field H I mossaic of M31: II. the disk warp, rotation and the dark matter halo. *Astron. Astrophys.* **511**, A89.

Cram, T. R., Roberts, M. S. & Whitehurst, R. N. 1980 A complete, high-sensitivity 21-cm hydrogen line survey of M31. *Astron. Astrophys.* **40**, 215–248.

Crosthwaite, L. P. & Turner, J. L. 2007 C0(1-0), CO(2-1), and neutral gas in NGC 6946: molecular gas in a late-type, gas-rich, spiral galaxy. *AJ* **134**, 1827–1842.

Dame, T. M., Koper, E., Israel, F. P. & Thaddeus, P. 1993 A complete CO survey of M31. I. distribution and kinematics. *Astrophys. J.* **418**, 730–742.

Efstathiou, G. 2000 A model of supernova feedback in galaxy formation. *Mon. Not. R. Astron. Soc.* **317**, 697–719.

Ehle, M. & Beck, R. 1993 Ionized gas and intrinsic magnetic fields in the spiral galaxy NGC 6946. *AA* **273**, 45–64.

Ferrière, K. 1993 The full alpha-tensor due to supernova explosions and superbubbles in the Galactic disk. *Astrophys. J.* **404**, 162–184.

Ferrière, K. M. 2001 The interstellar environment of our galaxy. *Rev. Mod. Phys.* **73**, 1031–1066.

Fletcher, A. 2011 Magnetic fields in nearby galaxies. *ASP. Conf. Series* **438**, 197–210.

Fletcher, A., Beck, R., Shukurov, A., Berkhuijsen, E. M. & Horellou, C. 2010 Magnetic fields and spiral arms in the galaxy M51. *Mon. Not. R. Astron. Soc.* **412**, 2396–2416.

Fletcher, A., Beck, R., Shukurov, A., Berkhuijsen, E. M. & Horellou, C. 2011 Magnetic fields and spiral arms in the galaxy M51. *Mon. Not. R. Astron. Soc.* **412**, 2396–2416.

Fletcher, A., Berkhuijsen, E. M., Beck, R. & Shukurov, A. 2004 The magnetic field of M31 from multi-wavelength radio polarization observations. *Astron. Astrophys.* **414**, 53–67.

Garcia-Burillo, S., Combes, F. & Gerin, M. 1993 CO in Messier 51 II. Molecular cloud dynamics. *Astron. Astrophys.* **274**, 148–164.

Gratier, P., Braine, J., Rodriguez-Fernandez, N. J., Schuster, K. F., Kramer, C., Xilouris, E. M., Tabatabaei, F. S., Henkel, C., Corbelli, E., Israel, F., van der Werf, P. P., Calzetti, D., Garcia-Burillo, S., Sievers, A., Combes, F., Wiklind, T., Brouillet, N., Herpin, F., Bontemps, S., Aalto, S., Koribalski, B., van der Tak, F., Wiedner, M. C., Röllig, M. & Mookerjea, B. 2010 Molecular and atomic gas in the local group galaxy M33. *Astron. Astrophys.* **522**.

Han, J. L., Beck, R. & Berkhuijsen, E. M. 1998 New clues to the magnetic field structure of M 31. *Astron. Astrophys.* **335**, 1117–1123.

Heiles, C., Goodman, A. A., McKee, C. F. & Zweibel, E. G. 1993 Magnetic fields in star-forming regions - observations. In: Protostars and planets III (A93-42937 17-90), p. 279-326.

Heyer, M. H., Corbelli, E., Schneider, S. E. & Young, J. S. 2004 The molecular gas distribution and Schmidt Law in M33. *Astrophys. J.* **602**, 723–729.

Hitschfeld, M., Kramer, C., Schuster, K. F., Garcia-Burillo, S. & Stutzki, J. 2009 A complete ^{12}CO 2-1 map of M51 with HERA. II. Total gas surface densities and gravitational stability. *Astron. Astrophys.* **495**, 795–806.

Houck, J. C. & Bregman, J. N. 1990 Low-temperature galactic fountains. *Astrophys. J.* **352**, 506–521.

Hughes, D. W., Proctor, M. R. E. & Cattaneo, F. 2011 The α-effect in rotating convection: a comparison of numerical simulations. *Mon. Not. R. Astron. Soc.* **414**, L45–L49.

Käpylä, P. J., Korpi, M. J. & Brandenburg, A. 2010 The α effect in rotating convection with sinusoidal shear. *Mon. Not. R. Astron. Soc.* **402**, 1458–1466.

Kennicutt, R. C. 1989 The star formation law in galactic disks. *Astrophys. J.* **344**, 685–703.

Korpi, M. J., Brandenburg, A., Shukurov, A., Tuominen, I. & Nordlund, A. 1999 A supernova-regulated interstellar medium: Simulations of the turbulent multiphase medium. *Astrophys. J.* **514**.

Krasheninnikova, I., Shukurov, A., Ruzmaikin, A. & Sokolov, D. 1989 Configuration of large-scale magnetic fields in spiral galaxies. *Astron. Astrophys.* **213**, 19–28.

Krause, F. & Rädler, K.-H. 1980 *Mean-Field Magnetohydrodynamics and Dynamo Theory*. Pergamon Press.

Kulsrud, R. M. & Zweibel, E. G. 2008 On the origin of cosmic magnetic fields. *Rep. Prog. Phys.* **71**.

Larmor, J. 1919 How could a rotating body such as the sun become a magnet? *Rep. Brit. Ass.* **87**, 159–160.

Marcon-Uchida, M. M., Matteucci, F. & Costa, R. D. D. 2010 Chemical evolution models for spiral disks: the Milky Way, M31 and M33. *Astron. Astrophys.* **520**.

McKee, C. F. & Ostriker, J. P. 1977 A theory of the interstellar medium - Three components regulated by supernova explosions in an inhomogeneous substrate. *Astrophys. J.* **218**, 148–169.

Moss, D. 1995 On the generation of bisymmetric magnetic field structures in spiral galaxies by tidal interactions. *Mon. Not. R. Astron. Soc.* **275**, 191–194.

Moss, D., Shukurov, A. & Sokoloff, D. 2000 Accretion and galactic dynamos. *Astron. Astrophys.* **358**, 1142–1150.

Moss, D., Shukurov, A., Sokoloff, D. D., Berkhuijsen, E. M. & Beck, R. 1998 The nature of the magnetic belt in M31. *Astron. Astrophys.* **335**, 500–509.

Muller, U. & Stieglitz, R. 2002 The Karlsruhe Dynamo Experiment. *Nonlin. Process. in Geophys.* **9**, 165–170.

Nieten, C., Neininger, N., Guelin, M., Ungerechts, H., Lucas, R., Berkhuijsen, E. M., Beck, R. & Wielebinski, R. 2006 Molecular gas in the Andromeda galaxy. *Astron. Astrophys.* **453**, 459–475.

Norman, C. A. & Ikeuchi, S. 1989 The disk-halo interaction: Superbubbles and the structure of the interstellar medium. *Astrophys. J.* **345**, 372–383.

Panesar, J. S. & Nelson, A. H. 1992 Numerical models of 3-D galactic dynamos. *Astron. Astrophys.* **264**, 77–85.

Parker, E. N. 1955 Hydromagnetic dynamo models. *Astrophys. J.* **122**, 293.

Phillips, A. 2001 A comparison of the asymptotic and no-z approximation for galactic dynamos. *Geophys. Astrophys. Fluid Dyn.* **94**, 135–150.

Pooley, G. G. 1969 5C 3: a radio continuum survey of M31 and its neighbourhood. *Mon. Not. R. Astron. Soc.* **144**, 101.

Rohde, R., Beck, R. & Elstner, D. 1999 Magnetic arms in NGC 6946 generated by a turbulent dynamo. *Astron. Astrophys.* **350**, 423–433.

Ruzmaikin, A. A. & Shukurov, A. M. 1981 Magnetic Field Generation in the Galactic Disk. *Sov. Ast.* **25**, 553–+.

Ruzmaikin, A. A., Shukurov, A. M. & Sokoloff, D. D. 1988 Magnetic fields of galaxies. *Kluwer, Dordrecht* .

Ruzmaikin, A. A., Sokolov, D. D. & Shukurov, A. M. 1985 Magnetic field distribution in spiral galaxies. *Astron. Astrophys.* **148**, 335–343.

Schuster, K. F., Kramer, C., Hitschfeld, M., Garcia-Burillo, S. & Mookerjea, B. 2007 A complete ^{12}CO 2-1 map of M51 with HERA I. Radial averages of CO, H I, and radio continuum. *Astron. Astrophys.* **461**, 143–151.

Shetty, R., Vogel, S. N., Ostriker, E. C. & Teuben, P. J. 2007 Kinematics of spiral-arm streaming in M51. *AJ* **665**, 1138–1158.

Shu, C.-G., Mo, H.-J. & Mao, S.-D. 2005 An analytic model of galactic winds and mass outflows. *Chinese J. Astron. Astrophys.* **5** (4), 327–346.

Shukurov, A. 2007 Introduction to galactic dynamos. In *Mathematical Aspects of Natural Dynamos*. Eds. E. Dormy and A.M. Soward, CRC Press.

Shukurov, A., Sokoloff, D., Subramanian, K. & Brandenburg, A. 2006 Galactic dynamo and helicity losses through fountain flow. *Astron. Astrophys.* **448**, L33–L36.

Sofue, Y., Fujimoto, M. & Weilebinski, R. 1986 Global structure of magnetic fields in spiral galaxies. *Ann. Rev. Astron. Astrophys.* **24**, 459–497.

Sofue, Y., Tutui, Y., Honma, M., Tomita, A., Takamiya, T., Koda, J. & Takeda, Y. 1999 Central rotation curves of spiral galaxies. *Astrophys. J.* **523**, 136–146.

Stanek, K. Z. & Garnavich, P. M. 1998 Distance to M31 with the Hubble Space Telescope and HIPPARCO red clump stars. *Astrophys. J. Lett.* **503**, L131.

Stil, J. M., Krause, M., Beck, R. & Taylor, A. R. 2009 The integrated polarization of spiral galaxy disks. *Astrophys. J.* **693**, 1392–1403.

Subramanian, K. & Brandenburg, A. 2006 Magnetic helicity density and its flux in weakly inhomogeneous turbulence. *Astrophys. J.* **648**, L71–L74.

Subramanian, K. & Mestel, L. 1993 Galactic dynamos and density wave theory - II. An alternative treatment for strong non-axisymmetry. *MNRAS* **265**, 649–654.

Sur, S., Shukurov, A. & Subramanian, K. 2007 Galactic dynamos supported by magnetic helicity fluxes. *Mon. Not. R. Astron. Soc.* **377**, 874–882.

Tabatabaei, F. S. & Berkhuijsen, E. M. 2010 Relating dust, gas and the rate of star formation in M31. *Astron. Astrophys.* **517**.

Tabatabaei, F. S., Krause, M., Fletcher, A. & Beck, R. 2008 High-resolution radio continuum survey of M33. III. Magnetic fields. *Astron. Astrophys.* **490**, 1005–1017.

Tully, R. B. 1988 *Nearby Galaxies Catalog*. Cambridge: Cambridge University Press.

Vainshtein, S. I. & Cattaneo, F. 1992 Nonlinear restrictions on dynamo action. *Astrophys. J.* **393**, 165–171.

Vishniac, E. T. & Cho, J. 2001 Magnetic helicity conservation and astrophysical dynamos. *Astrophys. J.* **550**, 752–760.

Walter, F., Brinks, E., de Blok, W. J. G., Bigiel, F., Kennicutt, R. C., Thornley, M. D. & Leroy, A. 2008 THINGS: The Hi nearby galaxy survey. *Astron. J.* **136**, 2563–2647.

Weilebinski, R. 1990 Magnetic fields in galaxies. The interstellar medium in galaxies; Proceedings of the 2nd Teton Conference, Grand Teton National Park, WY, July 3-7, 1989 (A91-55926 24-90). Dordrecht, Netherlands, Kluwer Academic Publishers, 1990, p. 349-369.

Widrow, L. M. 2002 Origin of galactic and extragalactic magnetic fields. *Rev. Mod. Phys.* **74**, 775–823.

Yin, J., Hou, J. L., Prantzos, N., Boissier, S., Chang, R. X., Shen, S. Y. & Zhang, B. 2009 Milky Way versus Andromeda: a tale of two disks. *Astron. Astrophys.* **505**, 497–508.